

Diploma Thesis

3D Printing of Hardmetal Bodies
by FFF (Fused-Filament Fabrication)

carried out at the
Institute of Chemical Technologies and Analytics
Faculty of Technical Chemistry
TU Wien

under the supervision of
Ao. Univ.Prof. Dipl.-Ing. Dr. techn. Walter Lengauer

by
Markus Fürst, BSc

Vienna, August 2020

Acknowledgments

First and foremost, I want to thank Walter Lengauer for the supervision of my thesis and the opportunity to be part of his research group even before this project. Without his assistance, expertise and patience during the past months, the completion of my studies would have been impossible.

Special thanks to HILTI AG represented by Patricia Alveen and Steven Moseley who initiated the project and gave me the opportunity to be part of it. Our discussions were fruitful in the past meetings and seeing that the cooperation went well, I'm looking forward to starting my PhD program in bilateral cooperation.

Further thanks go to Ivica Duretek, Christian Kukla and their co-workers for providing the material, the majority of the samples and most importantly a lot of know-how and expertise in the field of polymer chemistry and FFF, without which the project would certainly have been impossible.

I want to thank my research group fellow Christian Waldner and all other colleagues from our institute and beyond for making the time during my thesis at TU Wien a pleasant and interesting journey regarding work-related and leisure experiences.

I am grateful towards my family who have always supported me in every imaginable way to reach my personal goals without experiencing shortcomings and always being there for me.

Last but not least I owe a lot of gratitude to my partner Tanja Szikora, who not only had to cope with me when I brought work home during the past months but encouraged me the most to keep going, when the results and thus my mood seemed hopeless.

Abstract

Additive manufacturing (AM) of structural parts has gained an unprecedented boost through the demand of complex or individually shaped parts in aeronautics, the automotive industry, the health sector, or the luxury/sports sector, to name a selected few. AM is intriguing for hardmetals as well, as it allows to produce parts almost without geometrical limitations (inner cooling channels for machining tools, which are impossible to press) and without significant material waste, which is especially important for expensive metal powders such as W. Based on previous research [1], hardmetal (WC-10Co) parts were produced in a multi-step AM process based on fused filament fabrication (FFF). Commercially available ready-to-press (RTP) hardmetal powder containing paraffin-based pressing aid, was mixed with an organic binder consisting of a thermoplastic elastomer and a functionalized polypropylene to produce a flexible filament. The route from the filament to the structural part is a shaping-debinding-sintering (SDS) process, in which the filament was extruded on a commercially available low-cost 3D-printer (Wanhao Duplicator i3 Plus). The printer created the desired object layer by layer based on the CAD file which was supplied beforehand. After the green body was built, the object underwent a two-step debinding procedure. First, the wax and the elastomer were removed in a solvent debinding step in cyclohexane for 48 h at approximately 65°C. Afterwards the residual organic components were removed during a thermal debinding step in a tube furnace. Different atmospheres and temperature profiles were investigated, as the goal was not only to produce fully dense parts, but to reach the C window of hardmetals and thus a two-phased specimen. A printed green body naturally has a higher C content than a conventionally pressed sample, as a lot of organic material is added to the hardmetal powder through the binder. In addition to removing all organic components, the correct C level must be reached through the thermal debinding step, which was aspired by temperature and atmosphere variation. After thermal debinding the sample was vacuum sintered in an induction oven. The sintered sample's magnetic saturation, coercive force as well as the density were measured. After metallographic preparation, the sample's porosity was investigated using a digital microscope. During this thesis no dense specimen was achieved. The experiments showed that the cavities resulting from the printing step can not be removed by post-densification experiments such as cold or hot isostatic pressing. The post-densification experiments revealed that the cavities are connected meaning the samples show open porosity which voids the results of the density measurement by the Archimedes method. The printing parameters were varied in order to minimise or eliminate the cavities without success. The same set of parameters could not be applied to objects of different geometries. Regardless of the cavities, satisfactory results regarding the surface quality were achieved. Two filaments containing different RTP powder, but the same organic binder showed different surface quality as one filament yielded high-quality surfaces while the other filament led to the formation of blobs due to filament curling and over-extrusion at the surface. It was concluded that a thermal debinding program can not be developed without dense bodies, as the same set of debinding conditions (e.g. H₂, 600°C) removes a different amount of C depending on a sample's level of cavitation as the inner surface and the reactivity rises for porous samples. Further experiments should be conducted using a printer of higher quality as the limiting step during this thesis was certainly the shaping step. As the wax impacts the printing quality the idea of implementing any commercially available RTP powder into a printable filament is hardly realisable.

Table of Contents

Acknowledgments	I
Abstract	II
Table of Contents	III
1 Introduction and Motivation	1
2 Literature review	3
2.1 AM in general	3
2.1 AM of ceramic and metal materials	6
2.1.1 AM of ceramics	6
2.1.2 AM of metals	7
2.1.3 AM of hardmetals	8
2.2 Hardmetals	9
3 Experimental Part	12
3.1 Powder characteristics	12
3.2 Organic components	12
3.3 Investigated geometries	13
3.4 Production of the feedstock	13
3.5 Production of the filament	14
3.6 Shaping process	15
3.7 Solvent Debinding	15
3.8 Thermal debinding	16
3.9 Sintering	16
3.10 Analysis	17
3.10.1 Magnetic Measurements	17
3.10.2 Density	18
3.10.3 Metallography	18
3.10.3 Light-Optical-Microscopy (LOM)	19
	III

3.11 Other experimental procedures	19
3.11.1 Pressed samples	20
3.11.2 Cold isostatic pressing	20
3.11.3 Hot isostatic pressing	21
4 Results and Discussion	22
4.1 Overview and numbering of produced samples	22
4.2 Pressed samples	24
4.2.1 Mass loss and shrinkage of the pressed samples	24
4.2.2 Magnetic properties of the pressed samples	25
4.2.3 LOM results of the pressed samples	26
4.2.4 Summary of the pressed samples	28
4.3 1 st series	29
4.3.1 Printing parameters of the 1 st series	29
4.3.2 Mass loss and shrinkage of the 1 st series	29
4.3.3 Magnetic properties of the 1 st series	30
4.3.4 LOM results of the 1 st series	32
4.3.5 Surface quality of the 1 st series	36
4.3.6 Summary of the 1 st series	37
4.4 2 nd series	38
4.4.1 Printing parameters of the 2 nd series	38
4.4.2 Mass loss of the 2 nd series	38
4.4.3 Magnetic properties of the 2 nd series	39
4.4.4 LOM results of the 2 nd series	40
4.4.5 Summary of the 2 nd series	42
4.5 3 rd series	43
4.5.1 Printing parameters	43
4.5.2 Mass loss and shrinkage of the 3 rd series	43

4.5.3 Magnetic properties of the 3 rd series	44
4.5.4 LOM results of the 3 rd series	45
4.5.5 Summary of the 3 rd series	47
4.6 4 th series	48
4.6.1 Printing parameters of the 4 th series	48
4.6.2 Mass loss and shrinkage of the 4 th series	48
4.6.3 Magnetic properties of the 4 th series	49
4.6.4 LOM results of the 4 th series	50
4.6.5 Summary of the 4 th series	53
4.7 5 th series	54
4.7.1 Printing parameters of the 5 th series	54
4.7.2 Mass loss and shrinkage of the 5 th series	54
4.7.3 Magnetic properties of the 5 th series	56
4.7.4 LOM results of the 5 th series	57
4.7.5 Summary of the 5 th series	74
4.8 Self-printed series	75
4.8.1 Printing parameters of the self-printed series	75
4.8.2 Mass loss of the self-printed series	75
4.8.3 Magnetic properties of the self-printed series	76
4.8.4 LOM results of the self-printed series	77
4.8.5 Surface quality of the self-printed series	80
4.8.6 Summary of the self-printed series	81
4.9 Isostatically pressed samples	82
4.9.1 Printing parameters of the isostatically pressed samples	82
4.9.2 Mass loss and shrinkage of the isostatically pressed samples	82
4.6.3 Magnetic properties of the isostatically pressed samples	82
4.9.4 LOM results the isostatically pressed samples	84

5 Conclusion and Outlook	87
A list of the most promising candidates and their printing parameters is presented in Tab. 12.	90
Tab. 12 Most promising candidates regarding the cavity situation	90
Bibliography	XCI

1 Introduction and Motivation

Since S. Scott Crump's patent for the first extrusion-based 3D-printer and the underlying fused deposition modelling process (FDM[®]) also called fused filament fabrication (FFF) in 1992 [2] additive manufacturing (AM) has become an established part of our society. Even though powder bed fusion (PBF) and stereolithography (SLA) technologies were developed even earlier in the 1980s, Crump's invention was the deciding factor at promoting AM in general public. When Crump's patent expired in 2009, AM and especially FFF processes gained unprecedented popularity through the sudden availability to everyone. This led to new developments in the field of conventional plastic printing as well as the application of material extrusion-based (MEX) processes to other materials than polymers. The idea of designing and consecutively fabricating one's own models, sculptures and parts without need for sophisticated machinery and post-processing has captured many since and thus led to the development of various AM systems and their implementation in all kinds of fields from household tinkering to industrial prototyping.

Spanning from Crump's invention three decades ago until today the dominating materials in AM are all sorts of plastics. As of today, AM of metals and ceramics is a well-established segment of the AM market sector with astonishing growth rates due to the increasing demand of complex shaped, well-performing structural parts in many different sectors. The metal AM market achieved nearly \$3.3 B revenue in 2018 which is expected to grow to \$11 B by 2024 [3]. The ceramic AM market expected to grow from \$20 M revenue in 2020 to \$450 M in 2029 [4]. The share of MEX processes using metal and ceramic materials in these numbers is still small. However, MEX processes were already applied to metals and ceramics by using powder-filled polymer filaments in the 1990s and early 2000s [5-7] and have developed as well over the last three decades. Especially the access to complex geometries without the need of expensive dies, moulds, shaping steps after sintering and the absence of scrap and waste material are beneficial factors for AM of metals and ceramics and led to the paradigm shift of from rapid prototyping to manufacturing fully functional parts in AM in general.

A material that yet plays a minor role in AM are hardmetals. Hardmetals belong to both categories of hard materials and composites and were until recently only produced via the traditional powder metallurgical route of pressing and sintering. Due to their unique combination of hardness and toughness they are often used in machining applications like cutting and drilling in form of drill bits or indexable inserts. Even though the geometries of the latter examples usually are easily achievable by conventional pressing, some special applications could require tools with internal cooling channels, which cannot be pressed, making AM a welcome alternative. The advantages such as material waste reduction, accessing geometries unavailable by pressing and especially cost reduction in post-processing, which are of substantial amount in the sector of hard materials, are an obvious driving force of applying AM processes on hardmetals. The production of a part involves a shaping – debinding – sintering (SDS) process and thus a multi-step process as opposed to powder-bed fusion (PBF) techniques such as selective laser sintering/melting or electron beam melting (SLS/SLM, EBM) where the desired part is obtained in a single-step process. Compared to the latter, MEX processes involve lesser investment and equipment costs and the possibility of a homogenous temperature treatment during sintering. MEX processes applied on hardmetals and cermets were extensively studied by Lengauer et al. in 2018 [1, 8, 9], although WC-Co used in FFF was already reported in 1997 [10], but without much detail as it was only included in a list along various investigated ceramic components.

As a part of a follow-up project on the above-mentioned studies of Lengauer et al., the aim of this thesis is to further optimise printing and post-processing parameters. The focus of the work presented, lied on the manufacturing of fully dense, sintered bodies originally printed by FFF. The ultimate aim is to match the mechanical and microstructural properties of traditionally pressed-and-sintered hardmetals using commercially available hardmetal powder containing pressing wax and to develop a process chain from the RTP powder to the sintered structural part, including manufacturing of the filament, printing the green body, debinding and sintering and testing the final product.

2 Literature review

This chapter will give a short overview over the definitions and history of AM with a special focus on ceramic and metal (and later hardmetal) materials.

2.1 AM in general

In this subchapter the most common techniques will be presented and a summary on their history will be given. According to the ISO/ASTM 52900 standard [11] additive manufacturing is defined in the following way:

“Additive manufacturing is the general term for those technologies that, based on a geometrical representation, create physical objects by successive addition of material.”

and furthermore, it is a

“process of joining materials to make parts from 3D model data, usually layer upon layer as opposed to subtractive manufacturing and formative manufacturing methodologies.”

All AM processes are based on a computer aided design (CAD) file which provides the geometrical information. The CAD file is processed by a slicer software to slice the digital 3D-model into multiple layers. The sliced file is processed by different machines, whose underlying techniques are presented below. The abovementioned standard defines seven different process categories of additive manufacturing. The standard's definitions and further information are listed below:

- Binder jetting (BJT)

BJT is a “process in which a liquid bonding agent is selectively deposited to join powder materials”.

It was developed by Sachs et al. in 1990 [12] and patented in 1993 [13]. BJT or inkjet printing was developed based on the traditional 2D inkjet printer. It was the first technique to be called “three-dimensional printing” a term later used to describe all AM variants. Like a 2D-printer, a printing head moves over a powder bed (e.g. gypsum, sand, metal, etc.) and deposits a liquid, organic binder to join the powder particles at the spots set by the CAD file. After the completion of one layer a movable platform lowers the powder bed and new powder is coated on top of the previous layer with a doctor blade. Then the printing head starts depositing the organic binder again and so forth until a three-dimensional object is embedded in the unbound powder.

- Directed energy deposition (DED)

DED is a “process in which focused thermal energy is used to fuse materials by melting as they are being deposited”.

In DED processes a usually metallic powder or wire is deposited through a nozzle and at the same time melted layer-by-layer by a high energy laser or electron beam at the nozzle's tip. The printing head containing the energy source as well as the material feedstock is often mounted on a movable robotic arm which enables higher geometric

independency. The process was developed in 1996 by a research group at Sandia National Labs [14]. The patented technology was called laser engineered net shaping (LENS) and was the first DED process. Advantages are the absent necessity of an actual powder bed as the material is deposited directly, thus reducing the amount of powder needed and accessing much larger geometries compared to other AM techniques. DED processes are often applied when metallic components need repair, or additional material must be added.

- Material extrusion (MEX)

MEX is a “process in which material is selectively dispensed through a nozzle or orifice”.

MEX processes using filaments are the commonly 3D-printing techniques known by the general public, however the extruded material can also be in form of a slurry, a suspension or granules. In 1988 S.S. Crump wanted to create a toy frog for his daughter by using a glue gun [15]. After several refinements he called his technology fused deposition modelling, filed a patent [2] and together with his wife co-founded Stratasys Inc., which is one of the largest AM companies to this day. In MEX processes typically a thermoplastic material, most commonly a filament, is extruded through a heated nozzle, which is mounted on a movable printing head and deposited on a building platform. The printing head follows a path given by the CAD file and deposits the material as so called “roads”, which are basically adjacent rows of extruded material. The final part is obtained by building the object bottom to top layer by layer. Like most other AM techniques FDM in its early years was aimed at an industrial business sector which was reflected in the acquisition costs of such machines, however two major turning points secured FDM’s spot on top of the most applied AM processes. One was the expiration of Stratasys Inc.’s patent in 2009, which led to the rise of several business competitors and thus an explicit price drop. The second event was the start of a project called RepRap (replicating rapid prototyper) by A. Bowyer et al. in 2005 [16]. The idea of the project was to create a machine which can reproduce as many of its parts as possible. The RepRap project was open source from the start and caught the interest of many hobbyists and enthusiasts bringing AM from industrial and academic facilities to the households of everyone. The RepRap project also coined the term fused filament fabrication to avoid legal conflict with Stratasys Inc.’s trademarked term fused deposition modelling (FDM®). FFF will be used in this thesis from here onwards to describe the filament extrusion-based process in AM.

- Material jetting (MJT)

MJT is a “process in which droplets of feedstock material are selectively deposited”.

MJT processes work like BJT processes with the difference that not a binding agent is deposited into a powder bed but the material itself (e.g. wax-metal-slurry) is deposited through a printing head. The first MJT technology was introduced by R.C.Sanders in 1995 [17]. The 3-D model maker, as Sanders named his invention, was used to print wax moulds for investment casting of jewellery. In 1996 3D Systems released a MJT-based technology depositing photocurable polymers [18]. Objet Geometries Ltd. (now merged with Stratasys Inc.) filed their patent in 2001 for their PolyJet process, a simultaneous jetting of different materials to obtain a 3D model [19].

- Powder bed fusion (PBF)

PBF is a “process in which thermal energy selectively fuses regions of a powder bed”.

In PBF processes a layer of powdered material (most commonly metals but also nylon) is thermally treated by a laser (selective laser melting/sintering – SLM/SLS) or an electron beam (electron beam melting – EBM) at selected spots, based on the CAD model. After the thermal treatment is completed, fresh powder is coated on to the building area from the powder reservoir with a doctor blade and the next layer is thermally treated. After the completion of every layer, the part is embedded in a bed of unbound powder. Making further heat treatment steps unnecessary PBF processes are single-step processes. The first PBF method patent was released in 1989 by C. Deckard, who developed the process few years prior still being an undergraduate student [20].

- Sheet lamination (SHL)

SHL is a “process in which sheets of material are bonded to form a part”.

The first SHL process was laminated object manufacturing (LOM) which was invented by Michael Feygin in 1988 [21] a founder of Helisys Inc. who distributed LOM machines until 2000. In SHL techniques layers of laminates of paper, ceramics or metals which are coated in an adhesive are bonded together successively. After each layer, a knife or laser cutter cuts the laminate according to the CAD file. In 2013 Mcor Technologies Ltd. released a technology based on SHL, which makes use of regular office printing paper to create coloured 3D-objects [22].

- Vat photopolymerization (VPP)

VPP is a “process in which liquid photopolymer in a vat is selectively cured by light-activated polymerization”.

VPP technologies derived from stereolithography, the firstborn of all additive manufacturing processes. The first published paper of H. Kodama in 1981 explained the principle of layer-by-layer construction of a solid part out of UV-cured resin [23]. In 1984 three French engineers filed a patent for a stereolithographic method [24] however the patent was abandoned by their employing company for lacking business perspective. Two months later C.Hull, nowadays considered among the founding fathers of additive manufacturing, introduced the term “stereolithography” when he filed his patent [25]. UV light curable photopolymer is placed in a vat. A light source cures the polymer in selected spots at the surface, based on the CAD model and the liquid resin solidifies due to photochemical reaction. After solidification, the building platform moves, fresh resin is reapplied on the surface and the next layer is built by exposure to the UV light. After numerous building steps the final part is cleaned from residual resin. Detailed surfaces can be achieved due to size limitations not being of mechanical nature like nozzle orifices but being set by the precision of the light source.

2.1 AM of ceramic and metal materials

In this subchapter the history and the applicability of AM with ceramics, metals as well as hardmetals will be discussed, with a special focus on MEX processes. Although AM processes were initially designed and developed with polymers as the building material, ceramic and metal materials quickly joined the ranks of processable AM materials.

2.1.1 AM of ceramics

Over the last three decades up until now AM of ceramics was and is not as common as AM of metals. However, the general benefits of AM such as accessing complex geometries, minimizing the waste material, and having a net-shape technology which eliminates post-processing steps also affect ceramics. Especially the post-processing procedures can become quite expensive for hard and brittle ceramics just as for hardmetals. The recent demand for complex shaped ceramic components in the aerospace, automotive and health sector led to a significant growth of AM of ceramics. The most common AM techniques for ceramic processing involves MEX, SHL, BJT and VPP processes such as SLA [26] and most processes are multi-step processes (indirect processes) which require a subsequent debinding step to get rid of organic binder material [27], although PBF processes are also applied to ceramics [28].

- MEX processes were successfully applied to alumina, zirconium oxides, zirconium diborides, boron carbides, silicon nitrides and bioglass parts [26]. Ceramic precursors consisting of the powder, water, organic binders, and further additives are extruded in form of a slurry, paste or filament and applied layer by layer to build a green body. Filament extrusion of ceramics was already reported in 1995 by Agarwala et al. [5] which was called Fused Deposition of Ceramics (FDC) following Stratasys' FDM[®], when the non-commercial term FFF was not yet introduced. One of the earliest materials they experimented with was Si_3N_4 . Bioglass, alumina and zirconia slurries were extruded using a custom-built printer by Owen et al. [29].
- Another multi-step technique to produce ceramic objects is SLA. A liquid slurry is cured by a light source in selected spots. The slurry consists of a photocurable polymer, the ceramic powder, and further organic additives such as dispersing agents. The object is built following the VPP principle. A commercially successful SLA technique to produce fully dense ceramic parts was developed by Homa and Benedikt which led to the Lithoz GmbH, an Austrian AM company focusing on SLA of ceramic components [30]. The available products are alumina, zirconia, and Si_3N_4 for structural purposes but also Ca_3PO_4 and $\text{Ca}_5(\text{PO}_4)_3(\text{OH})$ for medical applications. Several review articles on VPP were published already in 1996 by Griffith et al. [31] or in 2014 by Chartier et al. [32]. No AM technique has a superior resolution compared to VPP processes as no nozzle diameter can be as small as the nowadays reachable pixel densities.
- BJT of ceramics is also a multi-step process in which the organic binder is debinded after the green part is built, and the binder material is cured, to stabilize the green body. Numerous bio-compatible materials (phosphates, apatites), structural ceramics

(alumina, TiC, SiC) as well as electric functional ceramics (BaTiO_3) which were produced by BJT processes have been reported in a review article by Du et al. in 2017 [33].

Although AM of ceramics is still a minor sector compared to AM of metals the production of dense structural parts is certainly possible and commercially available. Especially the biocompatibility and the individual needs of every patient, make AM of ceramics a powerful asset in the health sector.

2.1.2 AM of metals

Compared to AM of ceramics, AM of metals is more widespread and industrially established which is visible in the growth rates [3, 4]. Especially the automotive industry was a promoter of AM of metals over the last years. A wide variety of techniques is available for AM of metals including MJT, BJT, DED, MEX and PBF processes, out of which the latter has the largest share on the metal AM market.

- DED and PBF processes are the most prominent procedures in the metal AM field. Several articles have been published discussing PBF and DED processes in detail [34-36]. PBF A high energy laser or electron beam fuses particles in a powder bed together by melting or only pre-sintering. A good flowability of the powder is required, making the use of gas atomized spherical powders necessary which are generally more expensive than regular powders. DED processes deposit the powder directly which at the same time is heated by a laser. Several industrial competitors offer services in this field e.g. the German EOS GmbH. Processable materials include almost every metal or alloy including steels, aluminium alloys, titanium alloys, copper, gold etc.
- There is currently a commercially available MJT process available offered by Israeli company XJet [37] where droplets of organic binder and nanoscale metal powder are deposited and cured by UV light. A detailed review of BJT techniques used on metals is given by Zhang et al. in [38] where they report the difficulties in post-processing. Furthermore, they report the successful production of TiAl, bronze, Inconel 625, and Fe-Mn alloys by BJT techniques.
- MEX processes are much less prominent than PBF techniques in the metal AM sector, but are rapidly growing. A comprehensive review of MEX processes of metal components was done in 2019 by Rane et al. [39]. The most intuitive way would be to treat metals like the polymer counterparts and extrude the viscous material through a nozzle, but the limiting factor is obviously the high melting point compared to polymers. There is the possibility of direct extrusion for low-melting Sn-Pb alloys [40] but this method is impossible for steels or other materials melting at high temperatures. Alternatives have been developed using water-based slurries in e.g. robocasting which is mostly used for biocompatible materials based on titanium [41]. Another possibility of extrusion is based on pastes and suspensions with organic binders, which was mostly applied to aluminium alloys. The most common way is to apply the principle of filaments or rods on metal MEX processes, where powders are combined

with large volume fractions of organic binder material to form extrudable feedstock. The first experiments were conducted at Rutgers University and the process was called FDMet in relation to FDM[®] as the experiments were carried out on a Stratasys printer [42-44]. Nowadays commercial solutions are offered by companies like American Desktop Metal Inc., which is a subsidiary of Stratasys, or Markforged. Producing metal parts by extruding granules originally used in metal injection moulding (MIM), is also possible as shown by a Chinese research group at Shenzhen University [45]. The list of materials suitable for metal MEX processes is long including copper, silver, titanium alloys, steels several composites with ceramic components etc.

2.1.3 AM of hardmetals

Amongst all materials processed by AM hardmetals or cemented carbides in general are one of the least investigated until now. Their standard manufacturing revolves around conventional powder-metallurgical methods, namely pressing, sintering (vacuum, hot isostatic pressing etc.) and post-processing e.g. coating. These procedures are well established but include many expensive investment and process steps such as die casting for pressing and time and money consuming post-processing because of the material's hardness. AM on the other hand would provide an interesting alternative for smaller quantities, which would make expensive dies obsolete, make new geometries accessible and eliminate costs and waste material in post-processing. Hardmetals or cermets consist of many different metal and ceramic powders and the finished product should have a homogenous microstructure regarding distribution and grain size. The materials must meet high expectations regarding their mechanical properties and small deviations in their compositions often lead to deterioration in their quality. All these arguments pose an interesting challenge for the AM of hardmetals and cermets. Until now a few studies on AM of hardmetals and cermets have been conducted mostly discussing the production by SLM, SLS and LENS. A significantly smaller number discusses the production by MEX, BJT, and 3D gel printing processes all of which will be briefly discussed below. Until now, the author knows of only two review articles being published on AM of hardmetals and cermets [46, 47] all of which were released in 2020 underlining the novelty of AM for hardmetals and cermets.

- SLM/SLS techniques were most often applied to manufacture hardmetals via AM. Like with other metal or ceramic powders a high energy laser beam is moved over a powder bed based on a CAD model, to fuse the powder particles into a three dimensional object layer by layer. A phenomenon which is known from PBF manufacturing of steels was also reported on hardmetals by Chen et al. [48], who came to the conclusion that spheroidal powders lead to specimen of higher density than non-spheroidal powders. While SLM directly melts the mixed powders to form the desired object, SLS is often followed by an infiltration step [49, 50], as reported by Kumar. Although different hardmetals and cermets were produced by SLM, SLS or LENS in several studies, no industrial applicable specimen was achieved, as a significant temperature gradient leads to an inhomogeneous microstructure (formation of ternary phases [46]) and the formation of cracks due to denser areas and more porous areas [9, 47].

- BJT and 3D gel casting were applied on hardmetals [51-54] and parts of high density were produced. The drawbacks are the complicated removal of organic binder afterwards, which often leads to residual pores.
- MEX processes are the most recent of all AM techniques applied on hardmetals and cermets, although first FFF experiments on WC-Co were already conducted in 1997 [10]. Lengauer et al. experimented on parts printed via FFF [1, 9] which satisfactory surface quality but residual cavities due to improper printing parameters. Furthermore, they listed a detailed description of FFF production of hardmetals compared to other AM techniques, which included the lack of unbound powders, which is essential in hardmetals and cermets consisting of many different powders which are potentially affected by separation, the uniform microstructure resulting from a homogenous temperature treatment, the absence of free powders, which can be a health hazard, and the possibility of nearly unlimited storage time under ambient conditions, as no unstable suspension or gels are used and the powder is protected from oxidation. Lieberwirth et al. [55, 56] successfully produced hardmetal parts out of MIM granules, which is a commercially available product without need of further preparation. The main issue of FFF printed hardmetal parts are the cavities resulting from the lack of filament bonding during printing, which requires a lot of optimisation.

2.2 Hardmetals

In this subchapter a summary on hardmetals regarding their history, chemistry and application will be given.

Hardmetals or cemented carbides are metal matrix composites (MMC) consisting of a brittle hard-phase and a ductile binder phase. The patent for the traditional hardmetal WC-Co was issued in 1923 by Karl Schröter [57], an employee under the supervision of Franz Skaupy at the “Osram Studiengesellschaft”, a German company, originally focusing on electric illumination. WC-Co combines superior hardness due to the brittle hard-phase with relatively high toughness due to the ductile binder phase. Up to this day the traditional hardmetal has been improved and modified, regarding the binder content and composition, grain size, and additives such as grain-growth-inhibitors (GGI) or corrosion inhibitors. There are many ways to optimise the material for the respective application reaching from mining of bedrock to precision drilling of PCB circuit boards. The unique combination of mechanical properties is the reason for hardmetals mainly being used in cutting, drilling, or milling applications (Fig. 1).

As mentioned before hardmetals mainly consist of WC (usually 0.2 to 10 μm) and Co (usually 4 to 25wt.%). The hexagonal (hcp) hard-phase grains are embedded in the face-centred-cubic (fcc) metal binder matrix (Fig. 1). Among the materials for machining purposes, hardmetals together with cermets, which are also MMCs, cover a wide range between hardness and toughness acting as a link between high-speed steels and the brittle ceramics (and ultimately diamond).

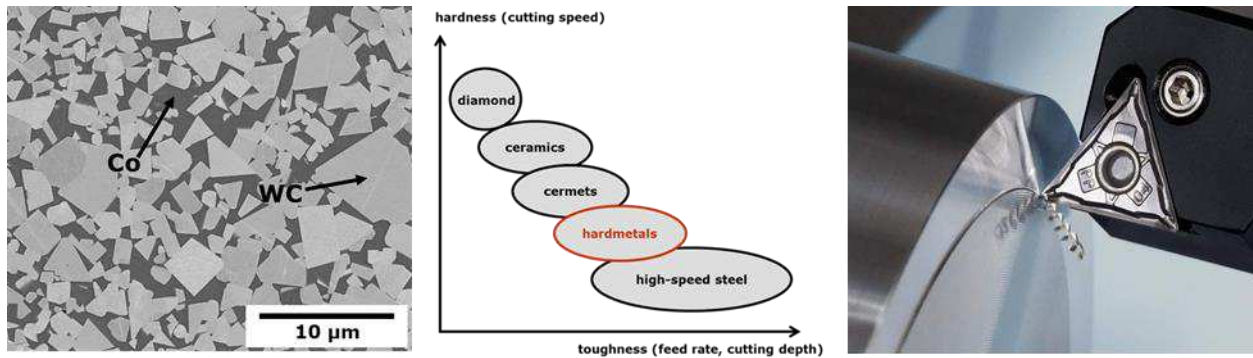


Fig. 1 From left to right: typical WC-Co microstructure (scanning electron microscopy image), positioning of hardmetals in the field of cutting materials, indexable insert during machining [58]

Hardmetals are usually produced via a powder-metallurgical route, where they are pressed and then sintered. The sintering process involves a liquification of the binder phase and a consecutive wetting of the hard-phase grains, which enables fast diffusion and solution/reprecipitation processes due to the mobile liquid phase. This liquid phase forms at a characteristic eutectic temperature depending on the composition. After sintering, the hardmetal is usually coated with property enhancing surfaces (e.g TiN for higher hardness) by chemical or physical vapor deposition (CVD, PVD) processes.

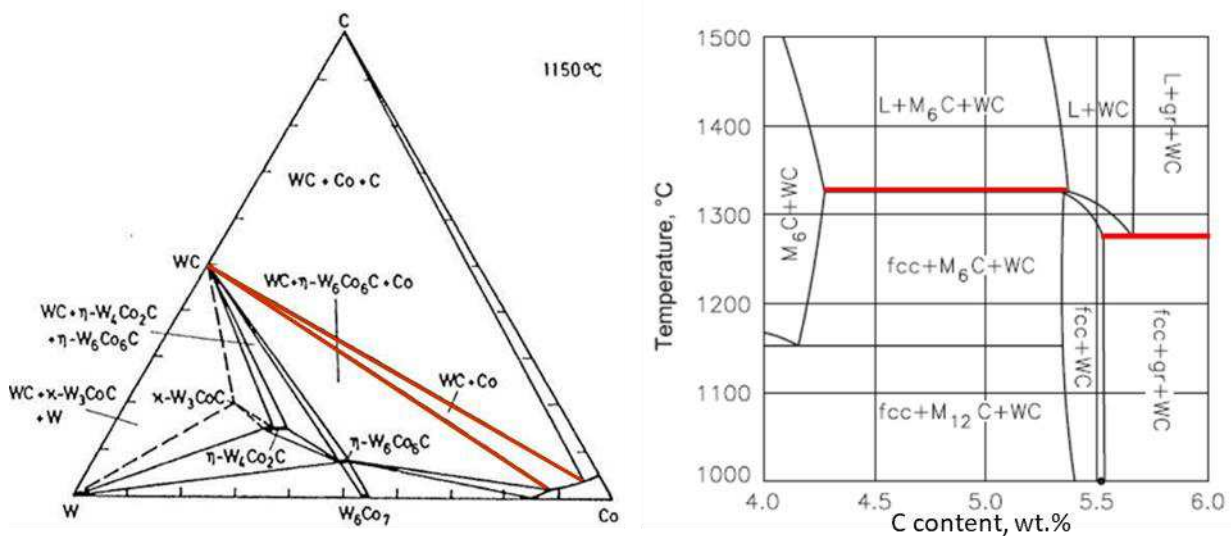


Fig. 2 Left: horizontal cross section through the ternary phase diagram of W-C-Co at 1150°C [59], right: vertical cross section through the ternary phase diagram of W-C-Co (10wt.% Co) [60]

The left image shows a horizontal cross section at 1150°C of the ternary W-C-Co phase diagram. At this temperature no liquid phase is formed yet. The highlighted zone in the left image represents the two-phase region consisting of WC and Co. This region is desired by hardmetal manufacturers, as additional phases lead to a deterioration of the mechanical properties. At low C contents η phase is formed. In the left image the η phase is described as W_6Co_6C . This is the case for 1150°C but at higher temperatures the phase consists of W_3Co_3C or W_4Co_2C as the equilibria shift with different temperatures. η phase is formed during the liquid sintering at higher temperatures and cannot convert to the M_6C

phase at lower temperatures due to too low diffusion rates. Even though being metastable, if η phase is present in a fully sintered sample, it is W_3Co_3C or W_4Co_2C with a high probability [59]. At high C contents free C precipitates as an additional phase.

The right image displays a vertical cross section for 10wt.% Co and a distinguished C range (note that the vertical cross section is presented in wt.%, whereas the horizontal cross section is presented in at.%). The highlighted temperatures indicate the eutectic temperature. It is lower in the region with C excess and higher for lower C contents. As seen above the eutectic temperature changes depending on the composition. Hardmetals are usually sintered at temperatures around 1400°C, where the liquid phase consists mainly of Co. It is the main driving force behind chemical and physical phenomena. The range of the two-phase region shifts after solidification of the liquid phase and diminishes towards an even thinner range. Between approximately 5.4 to 5.5wt.% C lies the two-phase region, which is also called the “C window”. The desired region only leaves a margin of 0.1wt.% C before the precipitation of unwanted additional phases. The impact of other additives (binder elements, GGI, corrosion inhibitors etc.) or composition on the hardmetals’ thermodynamics and kinetics influences the C window and the eutectic temperature greatly. This makes the production of hardmetal a delicate process, which must be optimised for each desired product.

3 Experimental Part

In this chapter the experimental procedures will be presented, including the materials used, the parameters and machines. The chapter is organised as the workflow from the raw powder to the analysed sample, with a few miscellaneous processes being introduced at the end of this chapter.

3.1 Powder characteristics

During this project, two different hardmetal powders were investigated. The first powder (CTS20L) was produced by Ceratizit S.A (from now on referred to as “Ceratizit”) and the second powder (812DWS) was produced by Hyperion Materials & Technologies Deutschland GmbH (from now on referred to as “Hyperion”). Both powders were ready-to-press (RTP) powders containing wax as a pressing aid. The powder specifications are displayed in Tab. 1. During the thesis, the focus lied mainly on the powder 812DWS, which from now on will be referred to as “Hyperion powder” or “Hyperion filament”. The CTS20L, from now on referred to as “Ceratizit powder” or “Ceratizit filament”, was only investigated during the 1st series and during the self-printed series for comparison reasons (4.1 Overview and numbering of produced samples).

Tab. 1 Powder specifications

812DWS					
Chem. Composition (w _i)		Powder properties		Phys. Properties	
WC	0.9125	Hall flow (s/25cm ³)	37	Specific weight (g/cm ³)	14.54
Co	0.0850	Apparent density (g/cm ³)	3.15	Mag. Saturation (4πσ)	162
Cr ₃ C ₂ (GGI)	0.0025	Pressure (MPa)	110	Hc (kA/m)	12
		Shrinkage (%)	18	Porosity	A00B00C00
				HV30	1440
CTS20L					
Chem. Composition (w _i)		Powder properties		Phys. Properties	
WC	0.8930	Hall flow (s/25cm ³)	-	Specific weight (g/cm ³)	14.45
Co	0.1000	Apparent density (g/cm ³)	-	Mag. Saturation (4πσ)	-
Other (GGI)	0.0070	Pressure (MPa)	-	Hc (kA/m)	-
		Shrinkage (%)	-	Porosity	-
				HV30	1660

3.2 Organic components

The organic components present in the final filament were the pressing-aid wax originally added by the powder manufacturers and a ready-to-use binder system provided by MU

Leoben. The exact nature of the wax is unknown as no information was provided by the powder manufacturers, although it is safe to assume that it is paraffin-based. The ready-to-use binder is based on the system from previous publications [9]. One component is a thermoplastic elastomer providing the filament's flexibility and the other component is a polypropylene functionalized with maleic anhydride serving as a backbone and providing green and brown body stability.

3.3 Investigated geometries

Three geometries were selected for different purposes. The shapes are shown in Fig. 3.

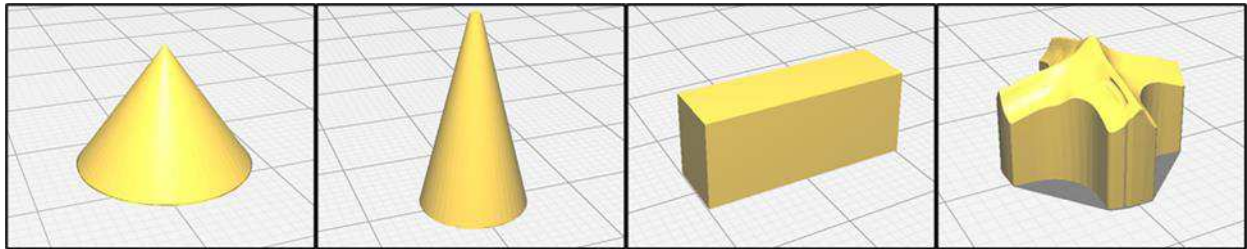


Fig. 3 3D-models of the selected geometries. From left to right: cone flat, cone pointy (only used in the 1st series and the self-printed series) while printing with Ceratizit filament), block, drill bit

The CAD files with the respective geometries were provided by HILTI AG.

The cone shaped geometries were selected to investigate the print quality in areas of different width. The impact of the gas atmosphere during thermal debinding and the resulting potential occurrence of third phased like η phase ($\text{Co}_3\text{W}_3\text{C}$) or free C can also be observed in cross sections of different width. The dimensions were set to $12 \times 12 \times 9 \text{ mm}^3$.

The drill bit shaped geometry was selected as an example of a tool and thus a likely application of AM hardmetal parts. Furthermore, it had the most complex structure to assess the geometrical capabilities of the printing process. The dimensions were $14 \times 15 \times 10 \text{ mm}^3$

The block shaped geometry was selected to have a potential body for mechanical testing of the tensile rupture strength (TRS). The mechanical testing was ultimately not performed due to large residual porosity. The dimensions were $27 \times 7 \times 10 \text{ mm}^3$

3.4 Production of the feedstock

The production of a flexible filament was done by a team at the Chair of Polymer Processing at MU Leoben. For preliminary testing and the first series a smaller amount of feedstock was prepared on a kneader (Plasti-Corder PL2000 Brabender GmbH & Co. KG) using the W 50 EHT chamber with roller blades (Fig. 4) The preliminary tests were performed to produce suitable filaments to have a base for the main production.



Fig. 4 From left to right: Kneader for preliminary tests, pelletizer, twin screw extruder with conveyor belt – pictures provided by Mr. Duretek (MU Leoben)

Two different powder loadings were produced (according to MU Leoben at 60 vol.% and 63 vol.%). Mixing was performed at 200°C at a rotational speed of 60 rpm and a duration of 30 min. The main amount of feedstock with a powder loading of 63 vol.% was produced using a co-rotating twin screw extruder (Leistritz ZSE 18 HP-48D, Fig. 4). The mass flow rate was 20 kg/h and the rotational speed of the screws was set to 700 rpm. The temperature of the cylinder zones ranged from 180 to 200°C. The extruded strands were transported over a metallic conveyor belt (Fig. 5) (SSC-04-12 Reduction Engineering GmbH) to a pelletizer (Reduction Engineering GmbH, Fig. 4) where the material was pelletized.

3.5 Production of the filament

The extrusion of the filament with a diameter of 1.75 mm for the preliminary tests was performed on a high-pressure capillary rheometer (Rheograph 2002 Göttfert Werkstoff-Prüfmaschinen GmbH, Fig. 5) after which the strands were deposited on a Teflon conveyor belt and cooled in ambient air. The extrusion of the main feedstock was performed on the extrusion line, starting with a single screw filter-test-extruder (FT-E20T-MP-IS Dr. Collin GmbH) and afterwards a haul off and winding unit (Fig. 5). The temperature range in the filter test extruder was set between 180 and 200°C and a 1.75 mm die was used. The rotational screw speed was set to 50 rpm. The haul off and winding unit for spooling (Fig. 5) was equipped with a laser measurement device (Laser 2010 T, Sikora) for diameter and ovality measurements.



Fig. 5 From left to right: metallic conveyor belt from 3.4 Production of the feedstock, capillary rheometer with Teflon conveyor belt, filter-test-extruder with haul off and winding unit – pictures provided by Mr. Duretek (MU Leoben)

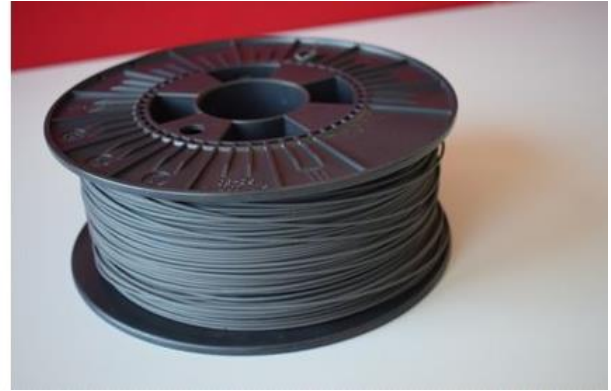


Fig. 6 Spools with wound-up, flexible filament

3.6 Shaping process

The CAD files of the geometries were provided by Hilti AG. MU Leoben used the slicing software Simplify3D to slice the CAD objects and convert it into a “gcode” file which afterwards was processed by the printer. MU Leoben used the Wanhao Duplicator i3v2 printer with nozzle diameters of 0.4 and 0.2 mm.

TU Wien used two different slicing softwares, one being Cura by Ultimaker B.V and PrusaSlicer by Prusa Research a.s. and the printing was performed on a Wanhao Duplicator i3 Plus (Fig. 7). The detailed printing parameters are included in *4 Results and Discussion* in the respective sample chapters.



Fig. 7 From left to right: Wanhao Duplicator i3 Plus [61], printed green part with brim to support adhesion, sintered part

3.7 Solvent Debinding

The printed parts were debinded in Cyclohexane for 48 h. The solvent debinding was performed to remove the wax and the elastomer. The procedure was performed in a beaker on a heating plate with magnetic stirring (Fig. 8). The temperature was set to approximately 65°C. The mass loss during solvent debinding was measured by weighing the sample before and afterwards.



Fig. 8 From left to right: Beaker with samples in Cyclohexane, tube furnace for thermal debinding, graphite crucible with arranged samples

3.8 Thermal debinding

After solvent debinding and thorough drying of the samples, they were thermally debinded to remove the organic backbone consisting polypropylene. Due to the samples being sensitive to mechanical impact and even slight shocks leading to breaking of the samples, they were put on small Al_2O_3 or C support plates to ensure a safe handling after thermal debinding. Different plate materials were chosen to observe if a different support plate material has an influence on the fully sintered sample's C balance. The thermal debinding was performed in a tube furnace (Fig. 8). N_2 and H_2 were applied as debinding atmospheres. The samples were heated up at a rate of $5^\circ\text{C}/\text{min}$ up to a maximum temperature of 600°C or 800°C . The maximum temperature was held for only one minute and the cooling followed Newton's law of cooling. After the thermal debinding the sample's mass was measured once again to calculate the mass loss.

3.9 Sintering

Sintering was performed in a mid-frequency induction furnace with a vacuum chamber (Fig. 9). The temperature was measured with an infrared-pyrometer (range $400\text{-}2200^\circ\text{C}$, Ircon SA, Ircon Inc., Fig. 10). The signal was sent to a control unit which in turn adjusted the generator's output to maintain the previously set sintering profile. Two different sintering profiles are shown in Fig. 9 and Fig. 10. On the left side a profile which was developed by the research group based on previous hardmetal research is shown. On the right side the recommended sintering profile from Hyperion is shown. The samples were arranged in a graphite crucible as shown in Fig. 8. After sintering the mass was measured once again. The Hyperion sintering profile was used from the 5th series onwards.

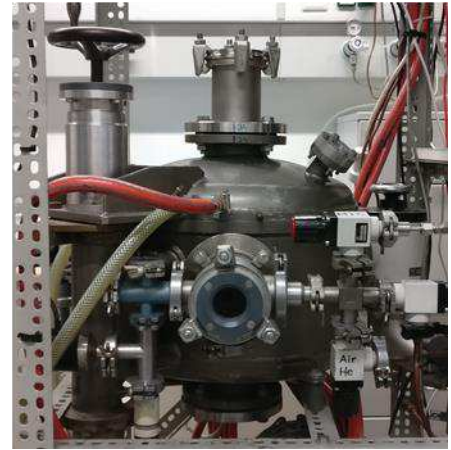
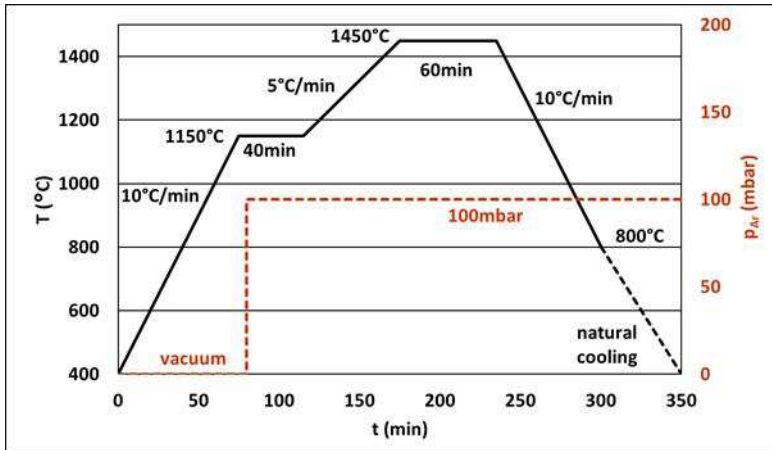


Fig. 9 Left: sintering profile developed in research group, right: mid-frequency induction furnace

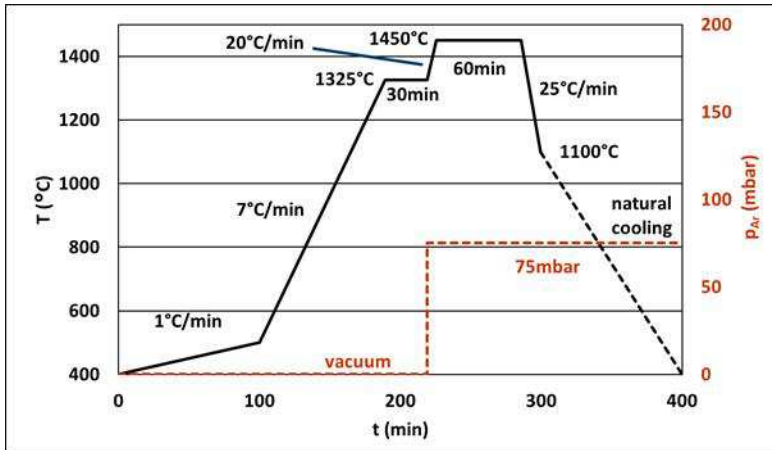


Fig. 10 Left: sintering profile recommended by Hyperion, right: infrared pyrometer on top of the furnace

3.10 Analysis

After weighing and imaging the samples before and after sintering the samples were analysed using the following methods.

3.10.1 Magnetic Measurements

The coercive force (kA/m) and the relative magnetic saturation, also referred to as $4\pi\sigma$ (%), in relation to pure Co were measured using a Koerzimat CS 1.096 (Foerster). The coercive force is dependent on the thickness of the binder phase between the hard-phase grains and thus a grain size can be calculated based on the coercive force value according to a formula (1)) related to the one published in [62].

$$L_{WC} = 76000 * (H_C * 1000)^{-1,23} \quad (1)$$

L_{WC} ... linear intercept length of the WC grains (μm)

H_C ... coercive force ($\text{kA}\cdot\text{m}^{-1}$)

The magnetic saturation is dependent on the state of solution of other elements in the binder phase. During this research the only possible elements dissolved in the binder phase were W, C and traces of Cr and other grain-growth inhibitors, declared by Ceratizit as “other” in *3.1 Powder characteristics*. From the solution level of W in the binder, the C level in the hardmetal can be deduced, as a higher C level in the hardmetal, leads to lower levels of dissolved W in the binder phase, given the C affinity of W. The measurement of the magnetic saturation a fast and non-destructive experimental method to discern if a hardmetal is two-phased or has an unwanted third phase like η phase or free C. (2) was used to calculate the relative magnetic saturation.

$$4\pi\sigma = \sigma_s * \frac{10000}{(202 * w(Co) * 100 - 0,876 * w(Cr) * 100)} \quad (2)$$

σ_s ... specific magnetic moment ($\mu T * kg^3 * m^{-1}$)

3.10.2 Density

The sample’s density was measured using the Archimedes principle. The equation (3) was used to calculate the density. The density value’s correctness cannot be assumed, as the samples showed open porosity the obtained results are questionable.

$$\rho_s = \frac{m_a * \rho_w}{m_a - m_w} \quad (3)$$

ρ_s ... sample density ($g * cm^{-3}$)

m_w ... sample mass in water ($g * cm^{-3}$)

m_a ... sample mass in air ($g * cm^{-3}$)

ρ_w ... water density ($g * cm^{-3}$)

3.10.3 Metallography

The samples were cut with a diamond blade in a high precision cut-off machine (Accutom 10, Struers) and consecutively embedded in bakelite (MultiFast, Struers) at 180°C and 15 kN for 6 min, using an embedding press (LaboPress-3, Struers). The grinding and polishing was performed on a RotoPol-31 (Struers) and the parameters are listed in Tab. 2. In a final step, the samples were etched using Murakami’s reagent for approximately 10 s.

Tab. 2 Grinding and polishing parameters

	Step 1: grinding	Step 2: polishing	Step 3: polishing	Step 4: polishing
Disc type (Struers)	MD-Piano	MD-Allegro	MD-Largo	MD-Dac
Grinding agent (Struers)	Diamond	Diamond (suspension)	Diamond (suspension)	Diamond (suspension)
Graining (μm)	220	9	3	1
Rpm	300	150	150	150
Cooling agent	Water	None	None	Lubricant Blue (Ethanol-based)
Force (N)	20	15	15	10
Time (min)	5	8	10	8

3.10.3 Light-Optical-Microscopy (LOM)

Imaging of the relatively large surface areas of the samples was performed with a digital microscope using an automatically movable sample table (VHX-5000, Keyence, Fig. 11).



Fig. 11 From left to right: uniaxial press, digital microscope, pressed samples on Al_2O_3 support plate ready for thermal debinding

3.11 Other experimental procedures

Other experiments included pressing the RTP powder with an uniaxial press to investigate the powder's thermal debinding and sintering properties without the addition of the ready-to-use binder and post-densification experiments by cold and hot isostatic pressing to try to eliminate cavities in the printed green body.

3.11.1 Pressed samples

The experiments during the thesis were conducted on pressed samples made from the pure “Hyperion powder” to investigate the behaviour during thermal debinding and sintering. For this purpose, the powder was pressed using a uniaxial press (Fig. 11) and a hardmetal die. 20 kN, which at the given diameter corresponds to a pressure of approximately 1550 bar, were applied as the pressing force for approximately 10 s. The samples were shaped cylindrical and had a diameter of 12.8 mm and a height of 1 and 6 mm respectively to investigate the impact of thermal debinding and sintering on areas of different thickness.

3.11.2 Cold isostatic pressing

To investigate if a post-densification process can be applied on the green bodies after printing two samples were cold isostatically pressed (CIP). The samples were put in a chamber of 32 mm in diameter and pressed using the parameters in Tab. 3. The sample names are explained in *4.1 Overview and numbering of produced samples*. The CIP experiments were done by MU Leoben.

Tab. 3 Cold isostatic pressing parameters

Sample	Time (min)	Pressing force (kN)	Chamber pressure (kbar)
CIP1	40	160	1.99
CIP2	40	60	0.75

Both green samples were produced using the two different sets of printing parameters from *4.4.1 Printing parameters* for one sample each. Fig. 12 shows several parts of the CIP process.



Fig. 12 From left to right: Sample packed in a latex bag ready for CIP, uniaxial press, compression mould (Paul-Otto Weber GmbH)

3.11.3 Hot isostatic pressing

A sample was hot isostatically pressed (HIP) at 200°C and 10 bar in its green state, to see if a post-printing densification by hot isostatic pressing is possible. For this purpose, an industrial gas pressure sintering furnace (FP W 1, FCT Systeme GmbH) was used and the temperature and pressure were upheld for 10 min. The drill bit sample was printed using the parameter set which was applied to the “5b” samples in *4.7.1 Printing parameters*.

4 Results and Discussion

In this section the results of the thesis' research will be presented and discussed. The section's structure is based on the chronology in which the series were produced and investigated. The first chapter will discuss the sample name labelling system and the following chapters will discuss the respective series starting with *4.2 Pressed samples* and ending with *4.9 Isostatically pressed samples*.

4.1 Overview and numbering of produced samples

This chapter will give a brief overview which samples were produced in which series and the sample name labelling system.

All samples were named according to this system:

Series no. / Powder / Therm. deb. parameters / Support plate material / Geometry

- **Series no.** is the number of the sample series (including "P" for pressed, the 5th series' subseries labelled "a" to "l", "sp" for self-printed, "CIP" and "HIP" for cold and hot isostatically pressed)
- **Powder** is either Hyperion powder (A) or CERATIZIT powder (B) (only relevant for the 1st series and the 1st self-printed series at TU Wien)
- **Therm. deb. parameters** is the combination of atmosphere and maximum temperature
- **Support plate material** is either Al₂O₃ or C
- **Geometry** is either the sample thickness (1 or 6 mm - only relevant for the pressed samples) or the geometry of the printed samples (Cone, Block, Drill Bit).

A few examples of sample names would therefore be:

PAN₂800AI6

In the first example the sample was pressed from Hyperion powder, thermally debinded under N₂ up to a maximum temperature of 800°C, the support plate material was Al₂O₃ and the sample's thickness was 6 mm. Another example is:

2spBH₂600CDB

In the third example the sample belongs to the 2nd self-printed series, is made from Ceratizit filament, was thermally debinded under H₂ up to a temperature of 600°C, the support plate material was C and the sample had a drill bit geometry.

5eAH₂200to300AIDB (5eDB)

In the second example the sample belongs to the 5th series, is made from Hyperion filament and was thermally debinded under N₂, except for a range between 200 and

300°C where H₂ was applied. The support plate material was Al₂O₃ and the sample had a drill bit geometry,

All samples are listed in Tab. 4.

Tab. 4 Overview over all samples

Pressed samples	1AN ₂ 600AIC	4AH ₂ 600CB	5jAN ₂ 800AIC (5jC)
PAH ₂ 800AI1	1AN ₂ 600AIB	4AH ₂ 600CDB	5jAN ₂ 800AIB (5jB)
PAH ₂ 800AI6	1AN ₂ 600AIDB	5th series	5jAN ₂ 800AIDB (5jDB)
PAH ₂ 800C1	1BN ₂ 600AIC	5aAH ₂ 200to300AIC (5aC)	5kAN ₂ 800AIC (5kC)
PAH ₂ 800C6	1BN ₂ 600AIDB	5aAH ₂ 200to300AIDB (5aDB)	5kAN ₂ 800AIB (5kB)
PAN ₂ 800AI1	2nd series	5bAH ₂ 200to300AIC (5bC)	5kAN ₂ 800AIDB (5kDB)
PAN ₂ 800AI6	2AH ₂ 800CB	5bAH ₂ 200to300AIDB (5bDB)	5IAN ₂ 800AIC (5iC)
PAN ₂ 800C1	2AH ₂ 800CDB	5cAH ₂ 200to300AIC (5cC)	5IAN ₂ 800AIB (5iB)
PAN ₂ 800C6	2AN ₂ 800CC	5cAH ₂ 200to300AIB (5cB)	5IAN ₂ 800AIDB 5iDB)
PAH ₂ 600AI1	2AN ₂ 800CB	5cAH ₂ 200to300AIDB (5cDB)	Self-printed samples
PAH ₂ 600AI6	2AH ₂ 600CC	5dAH ₂ 200to300AIC (5dC)	1spBN ₂ 800AIC
PAH ₂ 600C1	2AH ₂ 600CB	5dAH ₂ 200to300AIDB (5dDB)	1spBN ₂ 800AIB
PAH ₂ 600C6	2AH ₂ 600CDB	5eAH ₂ 200to300AIC (5eC)	1spBN ₂ 800AIDB
PAN ₂ 600AI1	2AN ₂ 600CC	5eAH ₂ 200to300AIB (5eB)	2spBN ₂ 800AIC
PAN ₂ 600AI6	2AN ₂ 600CDB	5eAH ₂ 200to300AIDB (5eDB)	2spBN ₂ 800AIB
PAN ₂ 600C1	3rd series	5fAN ₂ 800AIC (5fC)	2spBN ₂ 800AIDB
PAN ₂ 600C6	3AH ₂ 600CC	5fAN ₂ 800AIB (5fB)	3spAH ₂ 450to550AIDB (3spDB)
1st series	3AH ₂ 600CB	5fAN ₂ 800AIDB (5fDB)	4spAH ₂ 450to550AIDB (4spDB)
1AH ₂ 800AIC	3AH ₂ 600CDB	5gAN ₂ 800AIC (5gC)	Isostatically pressed samples
1AH ₂ 800AIB	3AN ₂ 600AIC	5gAN ₂ 800AIB (5gB)	CIPH ₂ 450to550AIB1 (CIP1)
1AH ₂ 800AIDB	3AN ₂ 600AIB	5gAN ₂ 800AIDB (5gDB)	CIPH ₂ 450to550AIB2 (CIP2)
1BH ₂ 800AIC	3AN ₂ 600AIDB	5hAN ₂ 800AIC (5hC)	HIPH ₂ 450to550AIDB (HIP)
1BH ₂ 800AIDB	4th series	5hAN ₂ 800AIB (5hB)	-
1AN ₂ 800CC	4AN ₂ 800AIC	5hAN ₂ 800AIDB (5hDB)	-
1AN ₂ 800CDB	4AN ₂ 800AIB	5iAN ₂ 800AIC (5iC)	-
1AH ₂ 600AIC	4AN ₂ 800AIDB	5iAN ₂ 800AIB (5iB)	-
1AH ₂ 600AIDB	4AH ₂ 600CC	5iAN ₂ 800AIDB (5iDB)	-

4.2 Pressed samples

In this chapter the pressed sample's results will be presented and discussed.

4.2.1 Mass loss and shrinkage of the pressed samples

In this subchapter the mass loss and the shrinkage are presented and discussed from thermal debinding to the fully sintered samples. Fig. 13 and Fig. 14 show the results for each sample of this series.

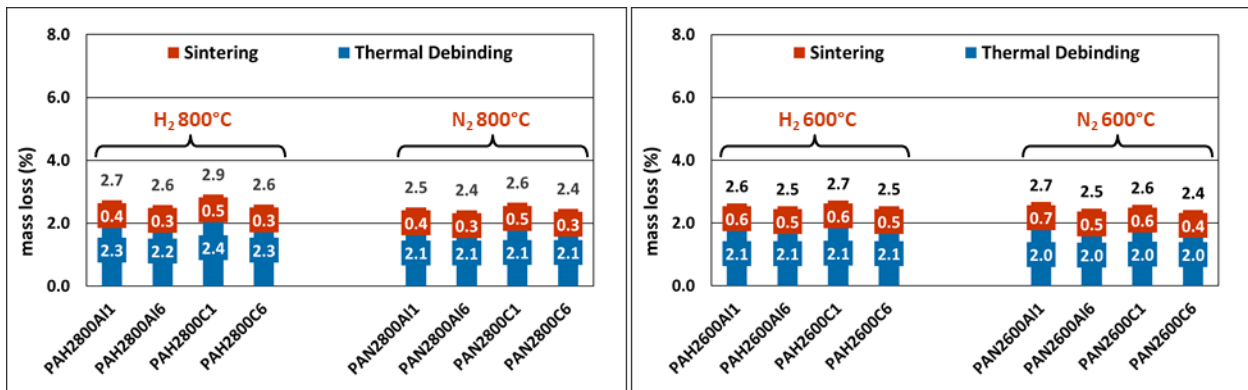


Fig. 13 Mass loss of the pressed samples

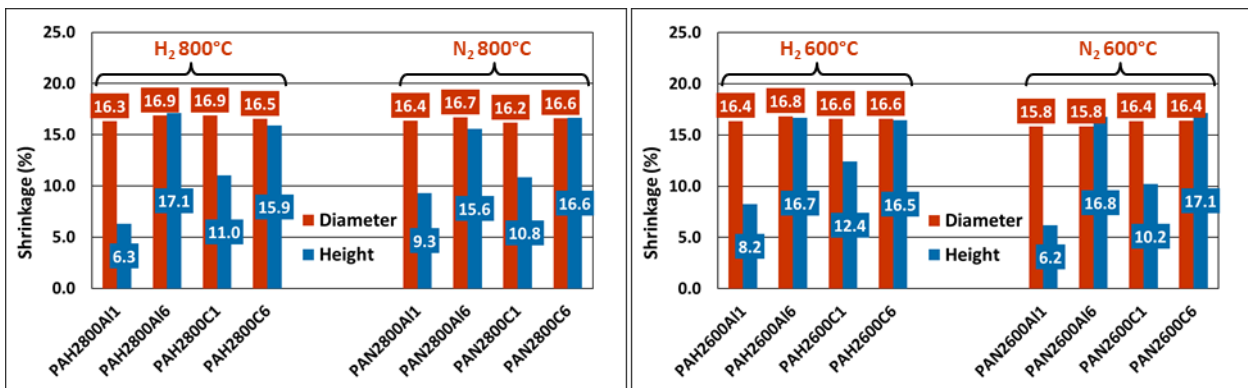


Fig. 14 Shrinkage of the pressed samples

The mass loss of the pressed samples during thermal debinding is higher under H₂ than under N₂, as well as higher for a maximum temperature of 800°C, compared to a maximum temperature of 600°C. The reason is the higher reactivity at higher temperatures and when using a reactive gas atmosphere like H₂, which removes C easily. The total mass loss of the thin samples is higher than the one of the thick samples but a significant impact of the support plate material on the mass loss could not be observed.

The shrinkage regarding the diameter is similar throughout the samples, meaning that the different parameters during thermal debinding had little to no effect on the shrinkage behaviour, (except PAN₂600A11 and PAN₂600A16 for unknown reasons). The shrinkage regarding the height of the samples is only representative for the thick samples and is comparable to the shrinkage in diameter. Strong bending of the thin samples led to difficulties in the measurement voiding the results.

4.2.2 Magnetic properties of the pressed samples

In this subchapter the magnetic properties are presented and discussed. Fig. 15 and Fig. 16 show the results for each sample of this series.

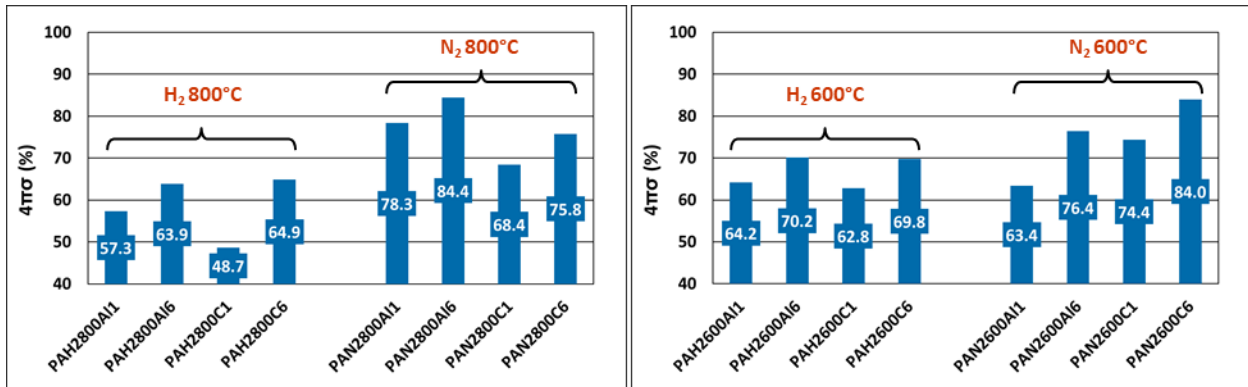


Fig. 15 Magnetic saturation of the pressed samples

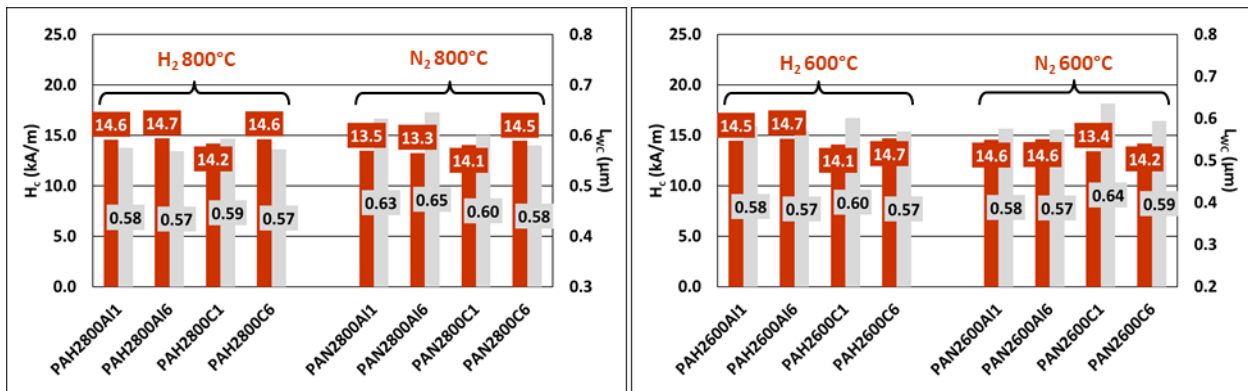


Fig. 16 Coercive force and L_{WC} of the pressed samples

The strongest impact on the magnetic saturation is seen at the samples which were debinded under H₂ up to 800°C, as these conditions lower the C level significantly and the samples drop into the η region. The magnetic saturation is lower for the thinner samples as the conditions during thermal debinding affect the whole sample volume and thus the C level faster compared to the thicker samples. H₂ and heating up to 600°C lowers the C level and the magnetic saturation significantly but not as much as heating up to 800°C. The highest magnetic saturation values are obtained during thermal debinding under N₂, even though no clear difference can be seen between 600 and 800°C, except that the results are inverse for the different support plate materials for unknown reasons.

The coercive force values are about the same for each sample, except for the two samples on the Al₂O₃ plate, which were debinded under N₂ up to 800°C. The reason for this small difference is unknown. The mass loss during thermal debinding corresponds to the 2% wax content which is included in the RTP powder according to the powder manufacturers. These are the magnetic properties of the samples out of Hyperion powder without any organic components except the powder manufacturers RTP wax, making a comparison to the printed feedstock samples with a higher starting C level unnecessary

as the pressing wax for example, is already dissolved in cyclohexane and therefore cannot be removed during thermal debinding anymore.

4.2.3 LOM results of the pressed samples

In this subchapter the LOM images are presented and discussed. Fig. 17 to Fig. 22 show the images for each sample of this series. All images of the pressed samples were made at 200x magnification.

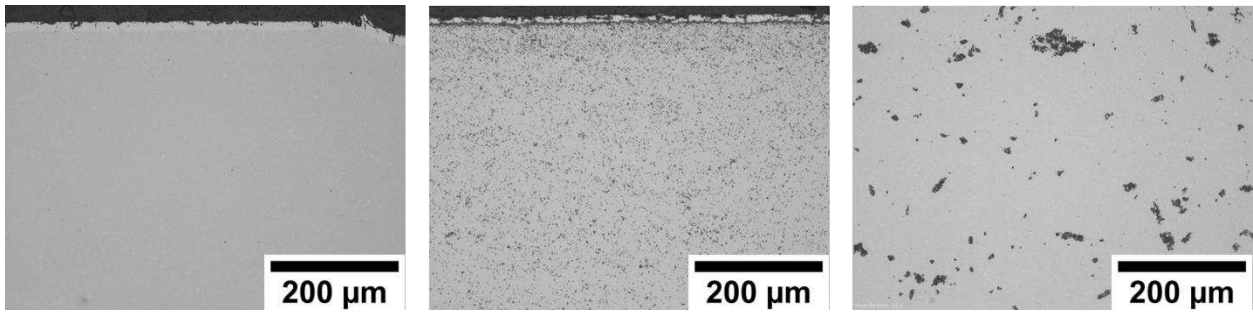


Fig. 17 From left to right: PAH₂800A11 unetched, PAH₂800A11 etched, PAH₂800A16 etched

On the left side an unetched sample is presented as an example with A00B00C00 porosity. The respective etched sample shows a fine dispersed η phase, whereas the right sample, which shows the thick version of the same sample, exhibits a coarse η phase.

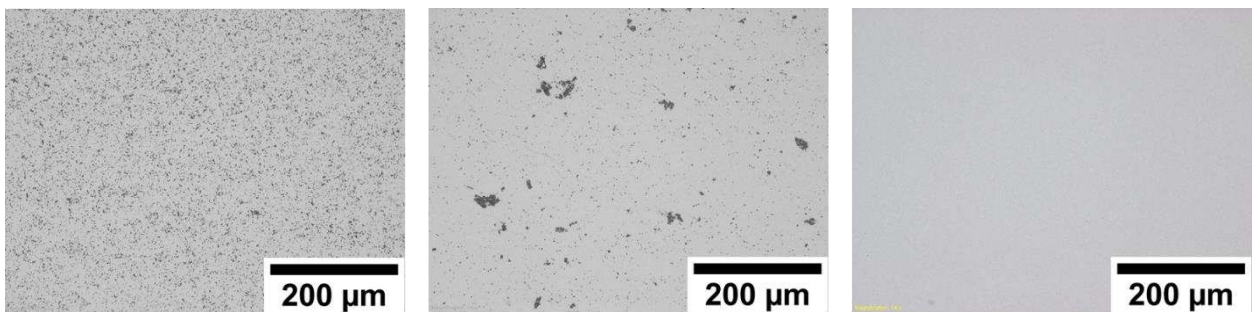


Fig. 18 From left to right: PAH₂800C1, PAH₂800C6, PAN₂800A11

The left sample has a fine dispersed η phase, the thicker middle sample a coarse η phase. The right sample debinded under N₂ lies in the two-phase region and has A00B00C00 porosity.

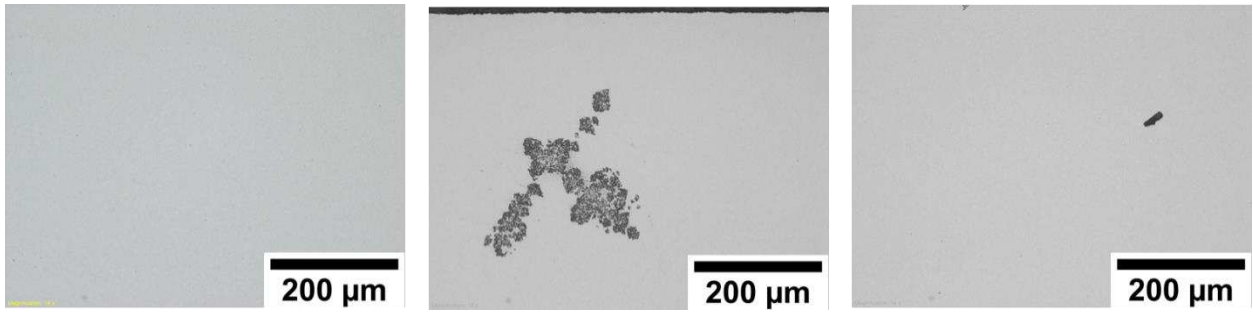


Fig. 19 From left to right: PAN₂800AI6, PAN₂800C1, PAN₂800C6

The left sample is two-phased and has A00B00C00 porosity, the middle sample shows η phase in its well-known flower resembling form and the right sample is two-phased and has A00B02C00 porosity.

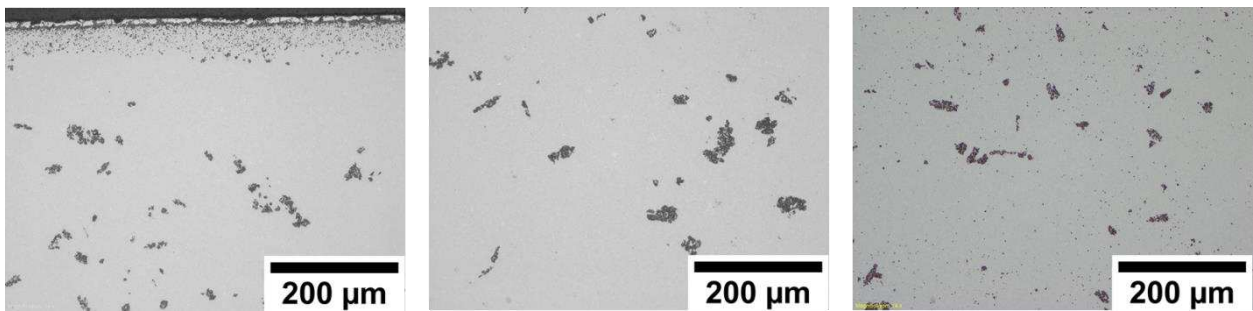


Fig. 20 From left to right: PAH₂600AI1, PAH₂600AI6, PAH₂600C1

The left sample exhibits η phase in different forms. In the sample's centre the η phase is coarse while towards the surface the η phase becomes fine dispersed. The atmosphere naturally has a stronger impact at the surface where more C is removed than in the samples centre. The middle sample shows coarse η phase as well as the right sample.

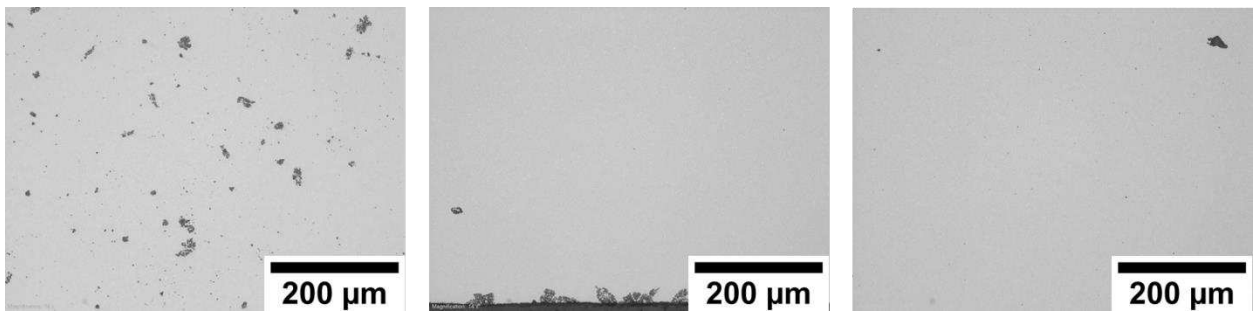


Fig. 21 From left to right: PAH₂600C6, PAN₂600AI1, PAN₂600AI6

The right sample exhibits η phase. The middle sample shows η phase only at the outmost border where too much C was removed, and the right sample is two-phased with A00B02C00 porosity.

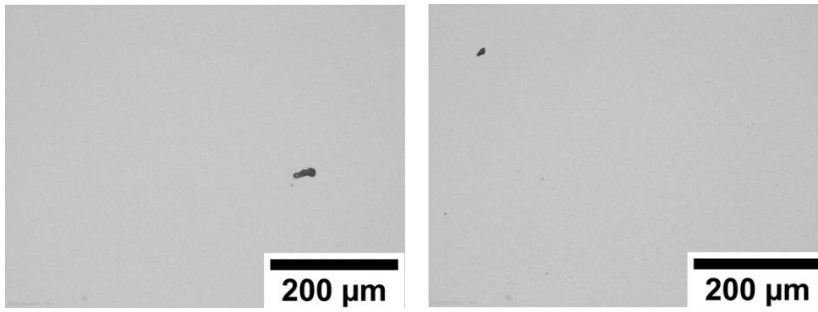


Fig. 22 From left to right: PAN₂600C1, PAN₂600C6

The two remaining samples debinded under N₂ are two-phased as well and both have A00B02C00 porosity.

4.2.4 Summary of the pressed samples

To summarize, the LOM results correspond with the magnetic saturation values. H₂ and higher debinding temperatures push the samples into the η region while N₂ and lower debinding temperatures remove just enough C for the sample to remain two-phased. The situation will however change significantly in the next chapters when additional organic material is added through the ready-to-use binder and the changing inner surface due to high levels of cavitation influences the C balance as well.

4.3 1st series

In this chapter the 1st series' results will be presented and discussed.

4.3.1 Printing parameters of the 1st series

The printing parameters are listed in Tab. 5.

Tab. 5 Printing parameters of the 1st series

	Row width (mm)	T _{Nozzle} (°C)	T _{Bed} (°C)	Print speed (mm/s)	Flow rate (%)	Nozzle diam. (mm)
Hyperion filament	0.1	250	95	12	130	0.4
Cerazitit filament	0.1	250	95	12	120	0.4

4.3.2 Mass loss and shrinkage of the 1st series

In this subchapter the mass loss and the shrinkage are presented and discussed. Fig. 23 and Fig. 24 show the results for each sample of this series.

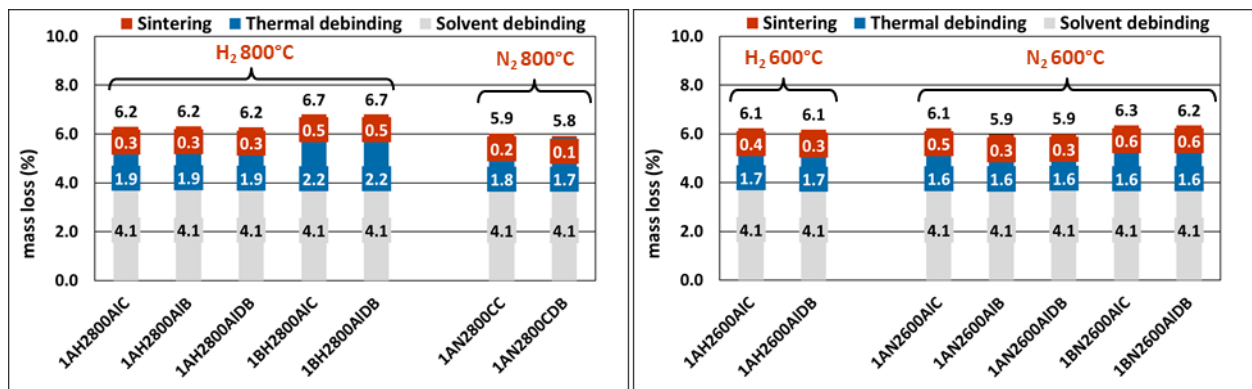


Fig. 23 Mass loss of the 1st series

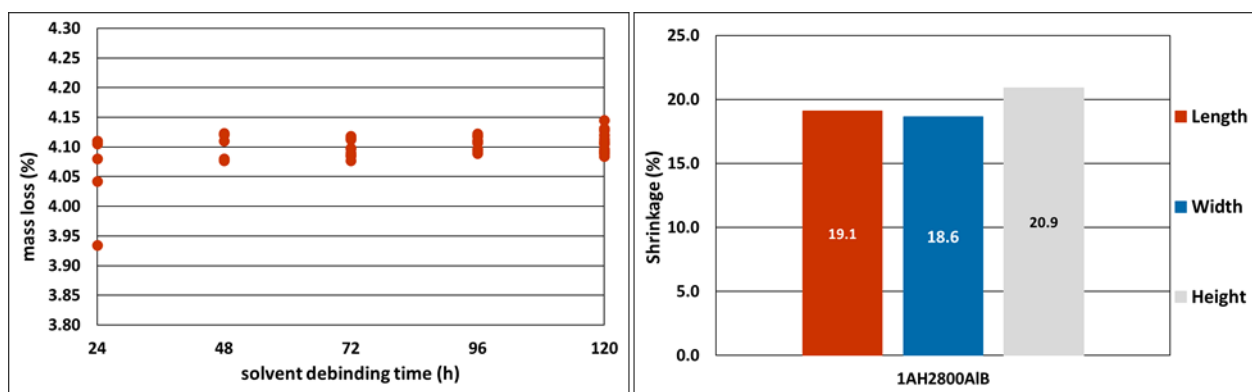


Fig. 24 Left: mass loss over time during solvent debinding of 1st series, right: shrinkage of sample 1AH₂800AIB

The mass loss during solvent debinding is similar among all samples of the 1st series in the range of 4.1 %. Like the pressed samples, the 1st series sample's mass loss during thermal debinding follows the trend: H₂, 800°C > N₂, 800°C ~ H₂, 600°C > N₂, 600°C. The total mass loss is a little smaller for the samples debinded under N₂ (exception: 1AN₂600AIC, due to a higher mass loss during sintering for reasons unknown) compared to the ones debinded under H₂. The samples made from the Ceratizit filament undergo a larger mass loss during thermal debinding, meaning the volume fraction of the polypropylene is higher compared to the Hyperion filament.

The mass loss is constant after 48 h making a prolongation of the solvent debinding step obsolete.

The shrinkage is not isometric for all directions. While the length and the width undergo about the same shrinkage, the height shrinks a little more than the other two dimensions.

4.3.3 Magnetic properties of the 1st series

In this subchapter the magnetic properties are presented and discussed. Fig. 25 and Fig. 26 show the results for each sample of this series.

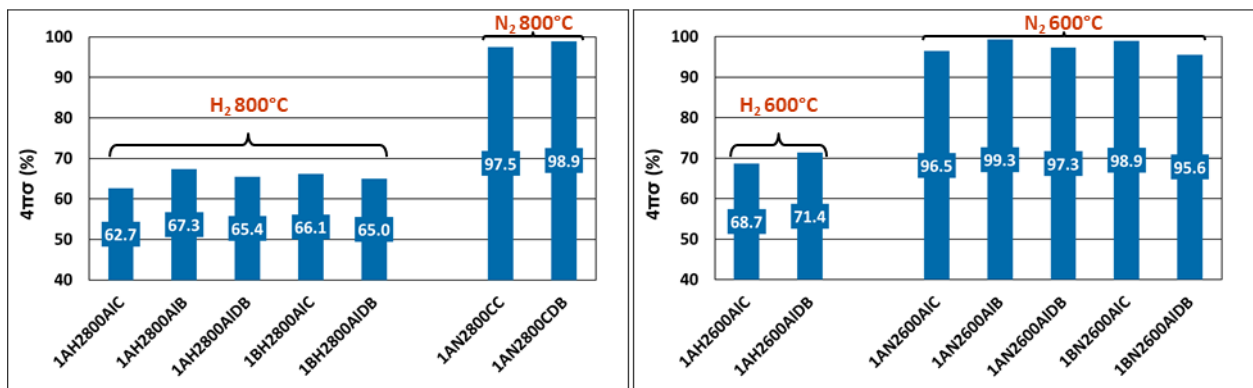


Fig. 25 Magnetic saturation of the 1st series

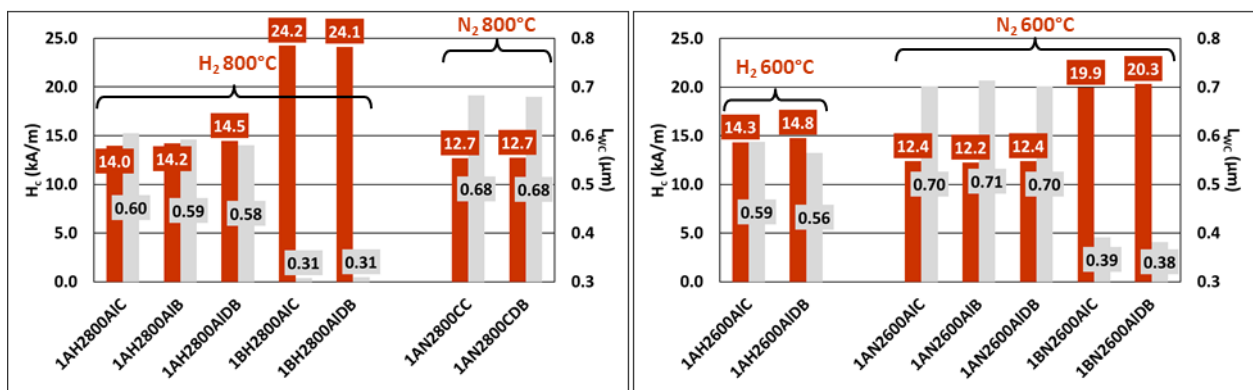


Fig. 26 Coercive force and L_{wc} of the 1st series

In correlation to the pressed samples, H₂ combined with either 600°C or 800°C maximum temperature shifts the 1st series samples into the η region, as enough C is removed in the

reactive gas atmosphere even though additional organic components are present. However, N_2 and either $600^\circ C$ or $800^\circ C$ are not enough to lower the C level to an extent to obtain two-phased samples, as the addition of organic components through the ready-to-use binder raises the starting C level drastically. Due to that, free C is present in the microstructure as will be presented in the next subchapter.

The coercive force is similar throughout the samples which were debinded under H_2 . All samples which were debinded under N_2 show similar results as well but are generally below the values of the H_2 samples. Initial N_2 treatment during the first heating in the thermal debinding step leads to a coarsening of the WC grains after sintering which in turn can be seen in the coercive force measurement. The values of the samples made from Ceratizit filament are higher. The reason is a smaller grainsize of the Ceratizit powder, compared to the Hyperion powder.

4.3.4 LOM results of the 1st series

In this subchapter the LOM images are presented and discussed. Fig. 27 to Fig. 31 show the images for each sample of this series. From this point on throughout the thesis, the figures will show a cross-section on top and below a magnified part of the sample. The scale bars are not unitised for each image, as the sample size differed, thus the scanned area was not the same and consequently the resolution of the images was not the same as well. Some images display only parts of the cross sections due to size and formatting reasons.

From the 3rd series onwards, the samples were cut at three different planes and metallographic specimen were prepared to represent the bottom, the centre, and the top of the sample. The threefold cutting of every sample was not possible in some cases due to geometrical and tool limitations.

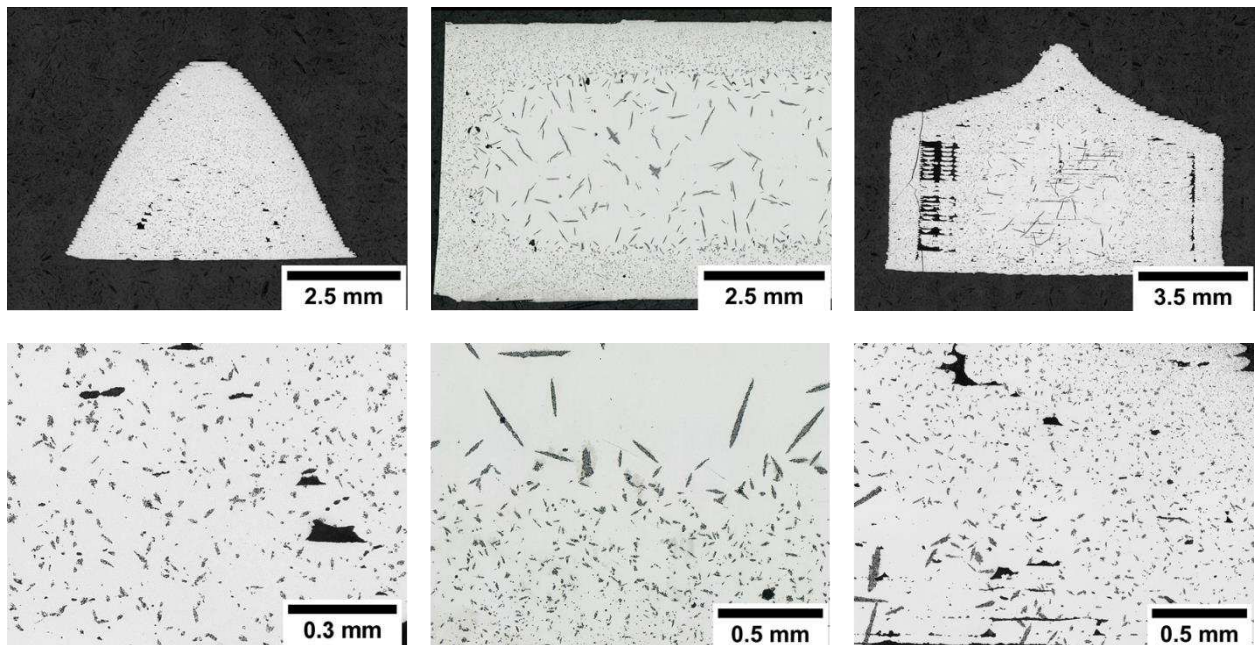


Fig. 27 From left to right: 1AH₂800AIC, 1AH₂800AIB, 1AH₂800AIDB

The left images display a cone's vertical cross section and the respective magnified part. The sample looks relatively dense, except for a curved area in the centre where cavities are present. The sample's microstructure shows fine dispersed η phase.

The central images display one half of a block's vertical cross section and the respective magnified part. The sample looks relatively dense as well except for a small number of cavities. The η phase changes from the border where fine dispersed η phase is present to the centre, where larger needles and flowers of η phase can be observed.

The right images display a drill bit's vertical cross section. Between the surface and the centre parts, large areas of cavities are present. This area is especially critical, because while a single layer is printed, a few rows that make up the rim of the layer are printed first and then the centre of the layer is filled afterwards. The interface between the border and the centre often lacks adequate bonding between the printed rows leading to the

above seen cavity areas. The drill bit sample also exhibits the gradient of different shapes and distribution of η phase like the block sample in the central images.

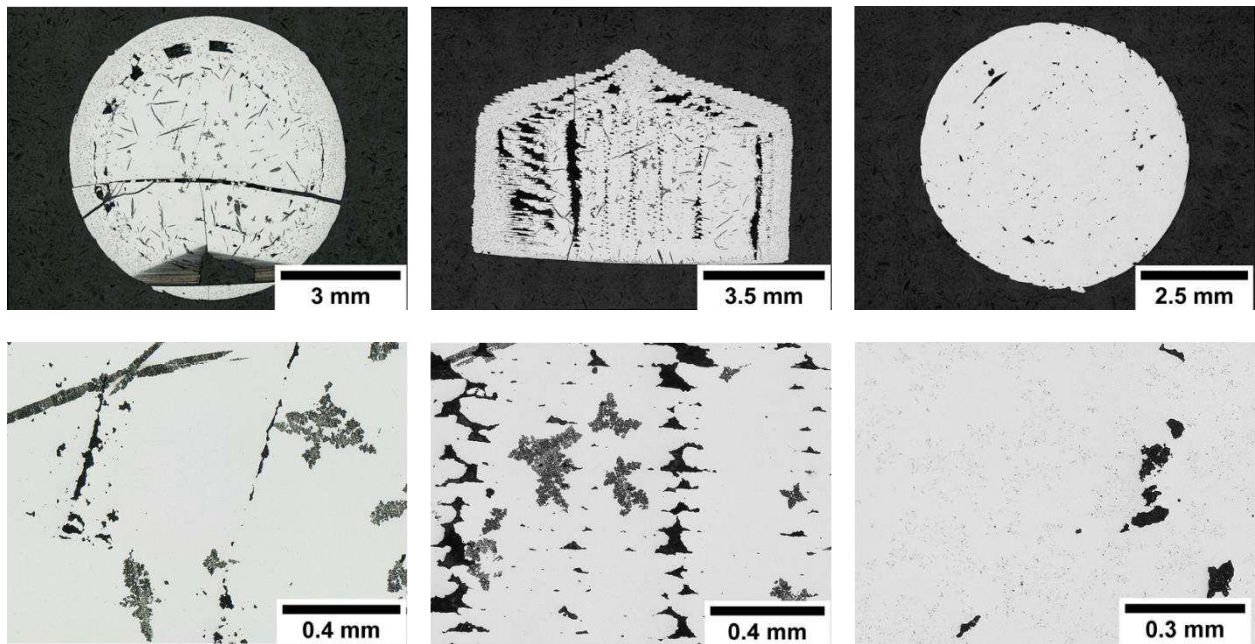


Fig. 28 From left to right: 1BH₂800AIC, 1BH₂800AIB, 1AN₂800CC

The left images show a cone's horizontal cross section and the respective magnified part. An area is seen which was not completely stripped from the embedding bakelite (bottom of the upper left image) and a few cracks resulting from the embedding process under pressure. Nevertheless, cavity areas at the border-centre-interface are observable, as well as a gradient in the η phase.

The central images show a drill bit's vertical cross section and the respective magnified part. Large cavity areas are observable as a result from poor row bonding during printing in the interface region as well as closer to the centre, especially on the left side. The distribution of η phase resembles the previous sample.

The right images show a cone's horizontal cross section and the respective magnified part. The sample has residual cavities at the beforementioned interface as well as in the centre but of a much lesser degree than the previous two samples. As expected from the magnetic saturation results, this sample exhibits a continuous free C phase throughout the whole sample volume.

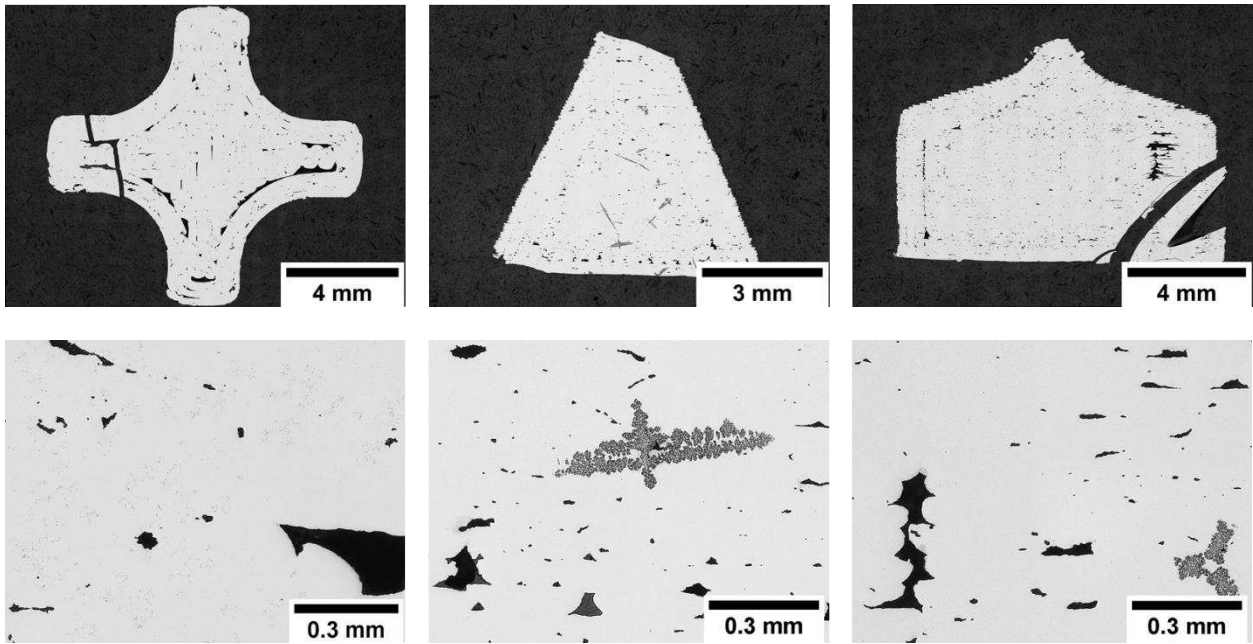


Fig. 29 From left to right: 1AN₂800CDB, 1AH₂600AIC, 1AH₂600AIDB

The left images display a drill bit's horizontal cross section and the respective magnified part with cavities along the interface between border and centre. Free C is present throughout the sample.

The central images display a cone's vertical cross section and the respective magnified part. Cavities are present, especially in the bottom region. Corresponding to the magnetic saturation results, η phase is present in the centre in the form of needles and flowers, but no η phase gradient is present.

The right images display a drill bit's vertical cross section and the respective magnified part. There is a broken piece resulting from the embedding and a covered area in bakelite. On the right side a large cavity area in the interface region between border and centre is visible. On the left half, the cavities also follow the interface region from the bottom to the top. Corresponding to the magnetic saturation, the sample only exhibits small amounts of η phase.

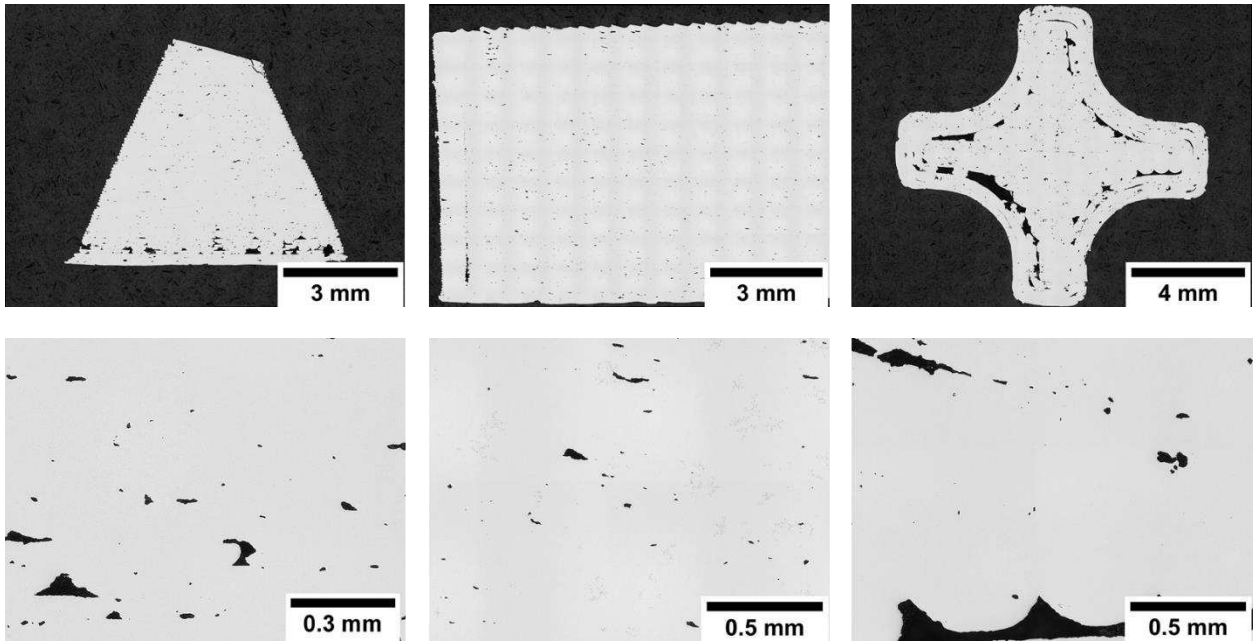


Fig. 30 From left to right: 1AN₂600AIC, 1AN₂600AIB, 1AN₂600AIDB

The right images show a cone's vertical cross section and the respective magnified part with large cavities in the bottom region. The number of cavities decreases going upwards in the sample. Contrary to the magnetic saturation values, the sample seems to be two-phased. The reason is unknown, as an error in the sample preparation did not occur knowingly nor any measurement parameters were changed (values above 95% generally are considered to lie in the free C region, but the more reliable result is always the metallographic specimen, especially if the value lies closely to the 95% like in this case).

The central images show one half of a block's vertical cross section and the respective magnified part, exhibiting a few cavities especially in the interface region on the left side. The sample exhibits free C throughout the whole sample volume.

The right images show a drill bit's horizontal cross section and the respective magnified part showing large cavities in the interface region, where the row bonding was of inadequate quality. This sample seems to be two-phased, just as the sample displayed on the left images, even though the magnetic saturation suggests otherwise. The explanation is to be found at the discussion of the left images.

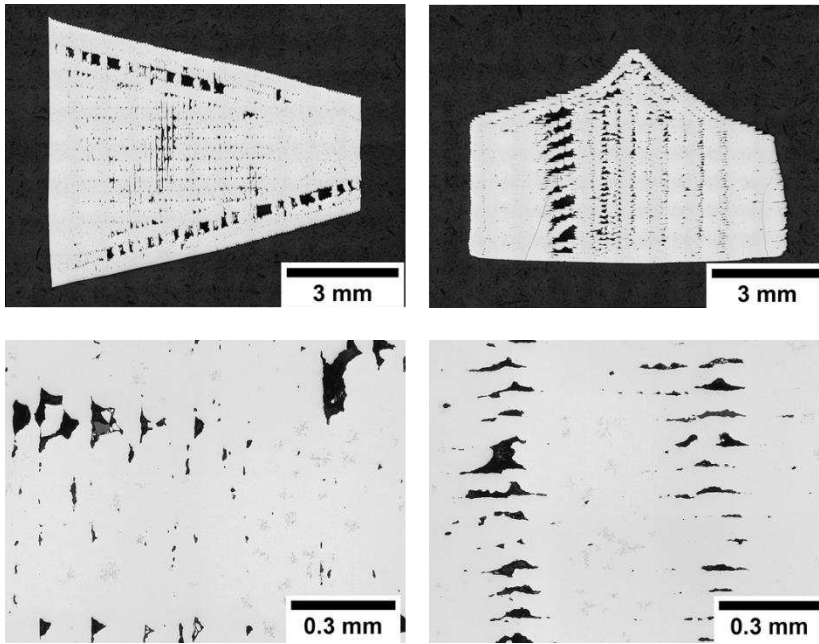


Fig. 31 From left to right: 1BN₂600AIC, 1BN₂600AIDB

The left images display a cone's vertical cross section rotated 90° to the right and the respective magnified part, exposing large cavities from bottom to top in the interface region, as well as smaller cavities in the sample's centre. Correspondingly to the magnetic saturation values, the sample exhibits free C throughout the whole volume.

The central images display a drill bit's vertical cross section and the respective magnified part showing cavities from bottom to top in the centre as well as large cavities in a certain area in the left half. Interestingly the interface region exhibits lesser cavities than the centre in this special case. Free C is present.

4.3.5 Surface quality of the 1st series

There was a significant difference in the surface quality as shown in Fig. 32. The sample made from Ceratizit filament on the left exhibits a smooth, detailed surface without errors. In the right image surface irregularities are visible at the bottom, at the middle as well as the tip. MU Leoben reported that the printing behaviour of the Ceratizit filament was better overall than of the Hyperion filament. The reason is most likely the paraffin-based RTP wax. The inorganic components are roughly the same in both powders and do not affect the printing properties as they are unaffected by the relatively low temperatures. The organic ready-to-use binder was the same according to MU Leoben, so the only remaining component that differs is the wax, which is different for every powder manufacturer. If this hypothesis is correct, the general idea of using commercially available RTP hardmetal powders is hard to put into practice as a generally applicable method is not possible to find if even the powder itself impacts the printing process in a potentially bad way.

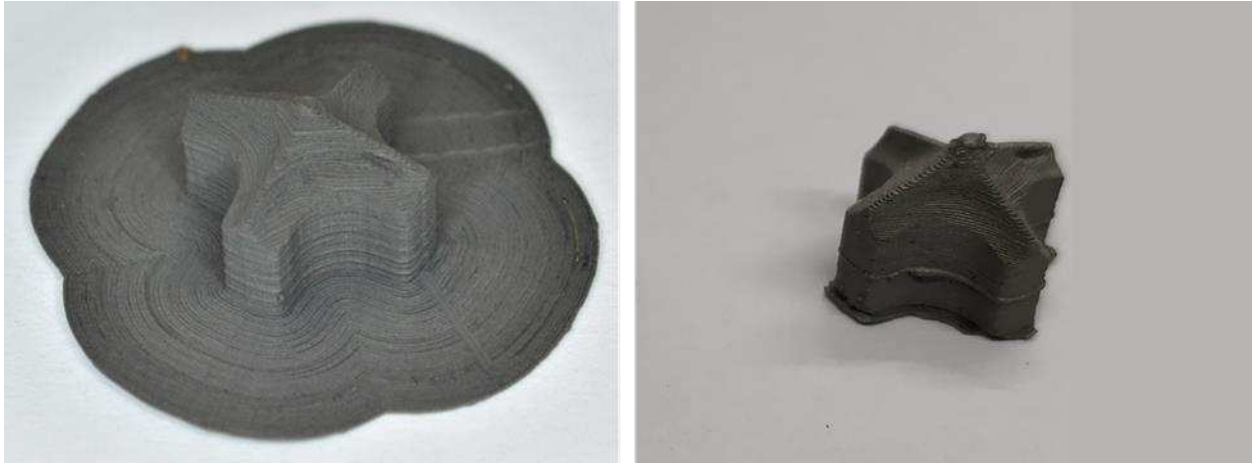


Fig. 32 Left: green body from Ceratizit filament with brim, right: green body from Hyperion filament

4.3.6 Summary of the 1st series

Concluding, H₂ at 600 as well as 800°C is enough to shift the printed samples of the 1st series into the η region. N₂ as a debinding atmosphere at the applied temperatures does not lower the C balance enough to gain two-phased samples. The LOM results correspond to the magnetic values except for two samples, which lie just above the 95% threshold which is often used as a rule of thumb to mark the border between two-phase and free C region. The printed samples have different degrees of cavity amount and size and the bonding in the interface region between border and centre is especially critical during printing, as a lot of cavities are positioned there. The mass loss during solvent debinding is around 4.1% and close to 2% during thermal debinding, which is not related to the pressed samples as the wax which made up the 2% in 4.2.1 *Mass loss and shrinkage of the pressed samples* is already removed during solvent debinding.

4.4 2nd series

In this chapter the 2nd series' results will be presented and discussed.

4.4.1 Printing parameters of the 2nd series

The printing parameters are listed in Tab. 6.

Tab. 6 Printing parameters of the 2nd series

	Row width (mm)	T _{Nozzle} (°C)	T _{Bed} (°C)	Print speed (mm/s)	Flow rate (%)	Nozzle diam. (mm)
Set 1	0.1	250	95	11	113	0.4
Set 2	0.1	250	95	16	111	0.4

4.4.2 Mass loss of the 2nd series

In this subchapter the mass loss is presented and discussed. Fig. 33 shows the results for each sample of this series.

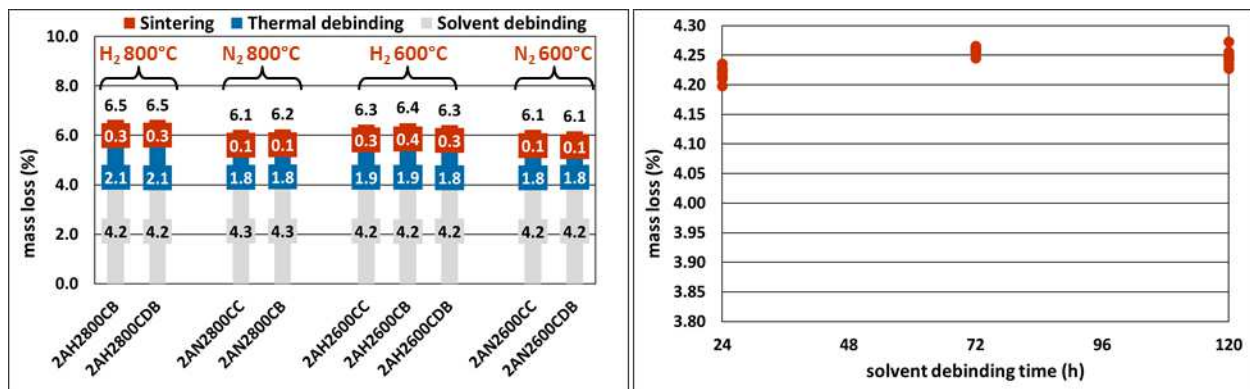


Fig. 33 Left: mass loss of the 2nd series, right: mass loss over time during solvent debinding of 2nd series

The mass loss during solvent debinding is similar among the 2nd series samples. It is generally approximately 0.1% higher than the solvent debinding mass loss of the 1st series samples. This may be due to the different printing parameters leading to more material being filled into the printed body. This hypothesis is also supported by the fact that more mass loss is observed during thermal debinding (0.1 to 0.2% compared to the 1st series samples), meaning that simply more organic material was present in the samples, because of the changed parameters. The mass loss during thermal debinding follows the previous trend again (H₂, 800°C > N₂, 800°C ~ H₂, 600°C > N₂, 600°C). There is no difference observable between the mass loss of the samples which were produced using Set 2 (2AN₂800CB, 2AN₂600CC, 2AN₂600CDB) and Set 1 (the rest).

On the right side the mass loss over time was observed, confirming the previous results, that a mass loss equilibrium during solvent debinding is reached after 48 h (4.3.2 Mass loss and shrinkage) or at the latest at 72 h as seen above.

4.4.3 Magnetic properties of the 2nd series

In this subchapter the magnetic properties are presented and discussed. Fig. 34 shows the results for each sample of this series.

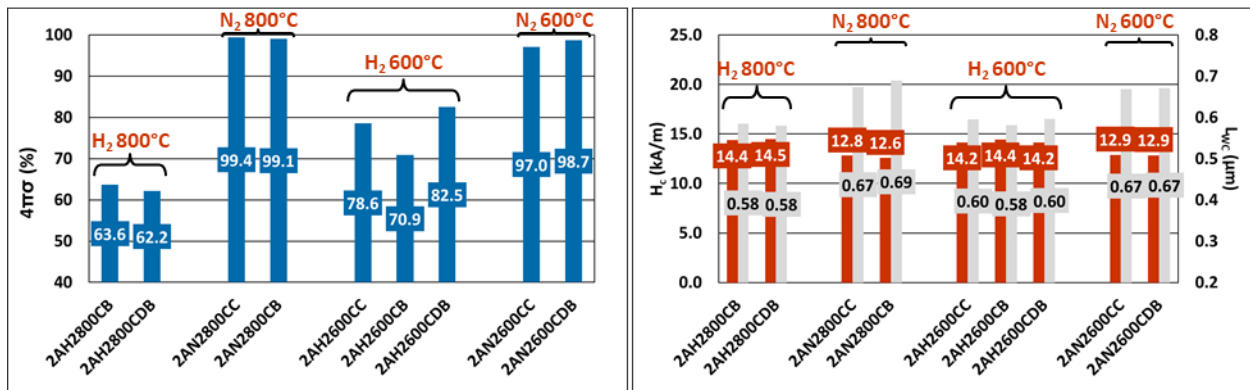


Fig. 34 Left: magnetic saturation of the 2nd series, right: coercive force and L_{WC} of the 2nd series

The magnetic properties of the 2nd show similar results as the 1st series. The magnetic saturation values of the samples which were debinded under N₂ lie in the free C region and the values of the samples which were debinded under H₂ up to 800°C lie in the η region. However, the saturation values for the samples debinded under H₂ up to 600°C show different results than the ones of the 1st series. The block has a lower magnetic saturation and is in the η region while the cone and the drill bit are in the two-phase region. The reason for the different values for the same conditions is unclear. One possible explanation is, that the cavity amount and the cavity orientation in the block sample resulted in a larger surface on the inside of the sample and thus a higher reactivity, which led to larger C loss.

The coercive force results resemble the ones from the 1st series with small differences which also might be a result of different printing parameters and thus another amount of inner surface due to cavities. The debinding under H₂ leads to finer grains than the debinding under N₂.

4.4.4 LOM results of the 2nd series

In this subchapter the LOM images are presented and discussed. Fig. 35 to Fig. 37 show the images for each sample of this series.

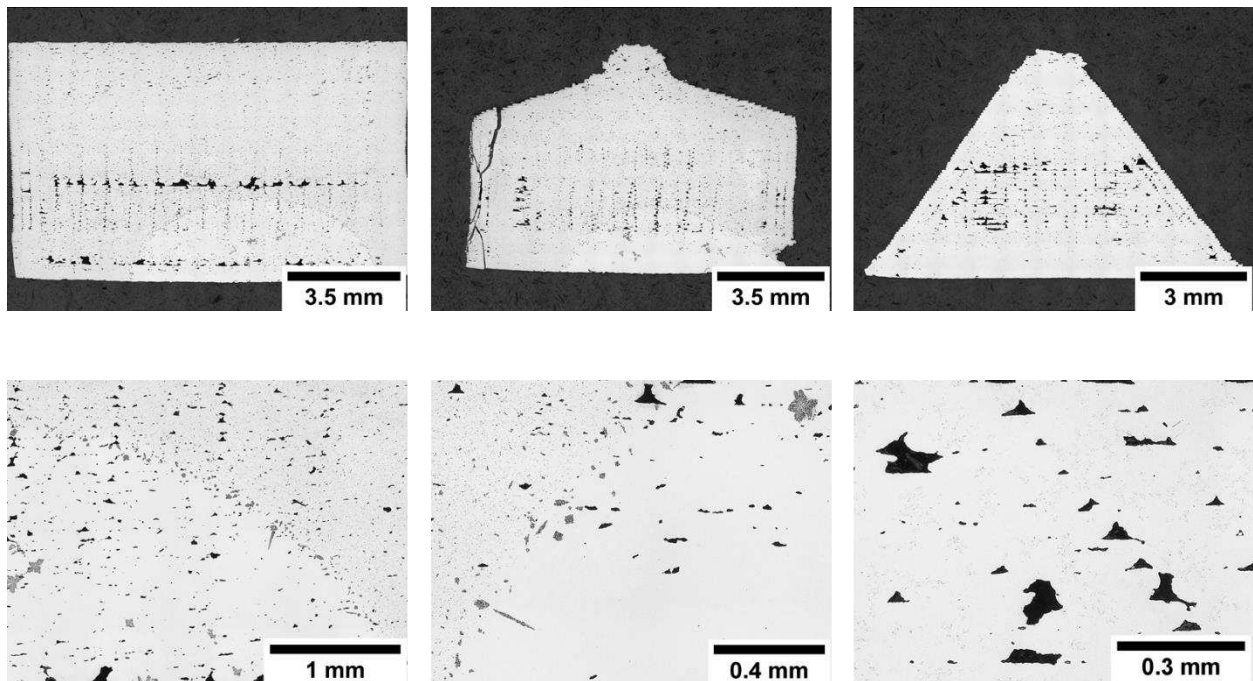


Fig. 35 From left to right: 2AH₂800CB, 2AH₂800CDB, 2AN₂800CC

The left images display a block's vertical cross section and the respective magnified part. There are two horizontal areas of larger cavities, one being at the bottom, and the other one being in the sample's centre. There are smaller cavities especially throughout the lower half of the sample, whose shape changes in the upper half. The cavities in the upper half of the block are round shaped and resemble regular macropores. There is no distinct area of particularly large cavities in the interface region between border and centre. The η phase is fine dispersed throughout the whole sample volume except for a semi-circular area at the bottom. The fine dispersion is a sign of an extremely low C balance. The coarse flower-shaped η phase area could be a result from the underlying C support plate providing an additional C source during the thermal treatments.

The central images display a drill bit's vertical cross section and the respective magnified part. Alongside some cracks resulting from the embedding process, cavities are present especially in the sample's centre and at a distinct area on the left side. The bottom exhibits a low number of cavities and at the top the cavities' geometry changes in a similar way as in the previous sample. The η phase gradient resembles the previous sample's results as well.

The right images display a cone's vertical cross section and the respective magnified part. While the bottom and the top of the sample are almost free of cavities, the centre is especially affected by areas of large cavities. Additionally, the interface region can clearly be distinguished by a line of cavities going up diagonally from bottom to top. The debinding under N₂ led to free C throughout the sample correspondingly to the magnetic saturation results.

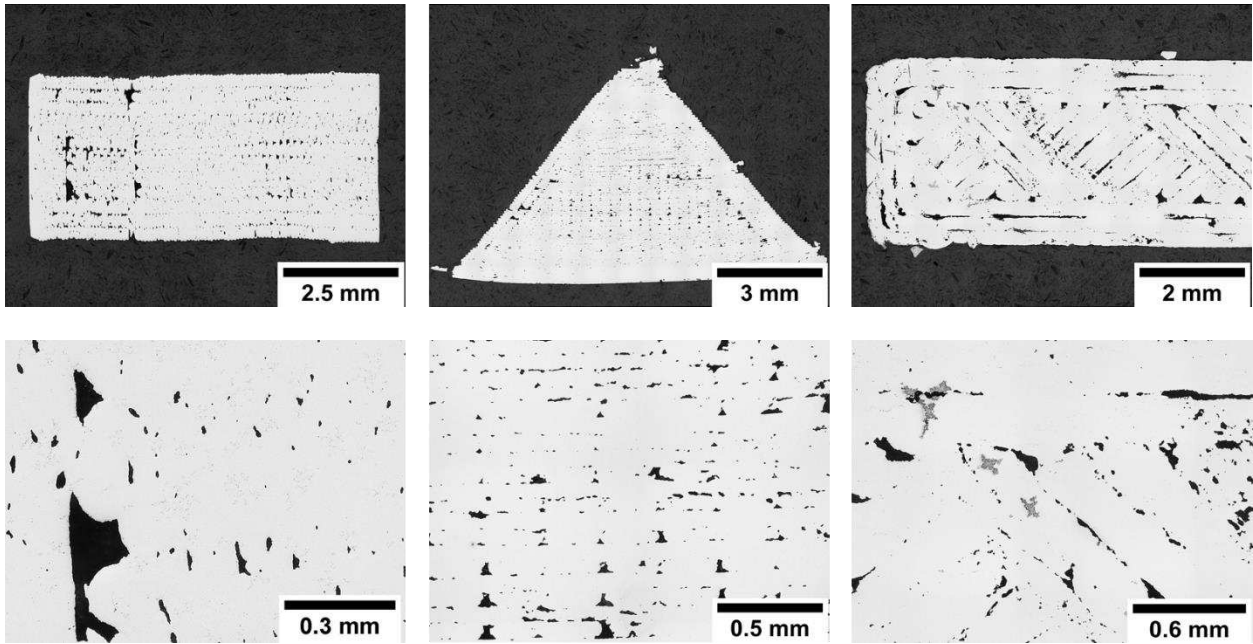


Fig. 36 From left to right: 2AN₂800CB, 2AH₂600CC, 2AH₂600CB

The left images show block's vertical cross section rotated 90° to the right and the respective magnified part. There are large cavity areas in the bottom region as well as starting at the top third. The interface region is not especially affected by cavities. The sample exhibits free C throughout the whole sample.

The central images show a cone's vertical cross-section and the respective magnified part. On the left edge the interface-induced cavity area can be observed, with some cavities being especially large. There are cavities in the centre as well, even though they are smaller than the ones on the edges. The bottom and the top do not exhibit many cavities. Corresponding to the magnetic saturation values the sample is two-phased, but at the tip formation of η -phase took place because of the small width of the sample and a faster perfusion with H₂.

The right images show one half of a block's horizontal cross section and the respective magnified part. The cavities clearly are a result of inadequate bonding during the zigzag printing, that was performed in the centre and the rectangular printing at the border region. The bonding between the two different areas is poor as well. Out of the samples which were debinded under H₂ up to 600°C, this was the one with the lowest magnetic saturation values and η phase is prominently present.

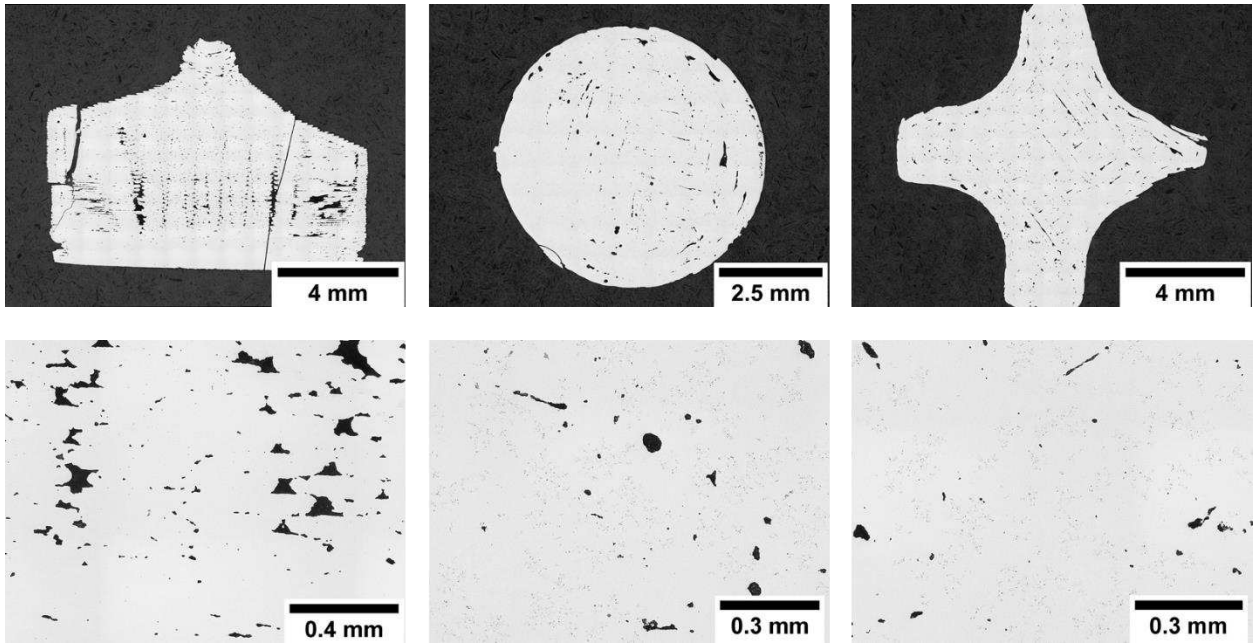


Fig. 37 From left to right: 2AH₂600CDB, 2AN₂600CC, 2AN₂600CDB

The left images show a drill bit's vertical cross section and the respective magnified part with several cracks stemming from the embedding. There are large cavity areas on both sides next to the centre reaching throughout the second third of the sample's height. On top of the centre area there are several smaller cavities and pores, whereas the first rows at the bottom seem to be cavity-free. The sample is two-phased.

The central images show a cone's cross section and the respective magnified part. Cavities in the interface region and the centre indicate the poor row bonding between the circular printed border region and the zigzag printed centre. The sample shows free C as a third phase.

The right images show a drill bit's horizontal cross section and the respective magnified part. Especially on the left and right flanks the cavities of the interface region are easily distinguishable. The ones resulting from zigzag printing in the centre are also visible in the right half of the sample. The sample exhibits free C.

4.4.5 Summary of the 2nd series

To sum up, a slightly different set of printing parameters did improve the density in some cases and in other cases worsened the cavity situation. Comparing the to different set of parameters, no clear winner is distinguishable, as Set 2 performed better for 2AN₂600CC and 2AN₂600CD but worse for 2AN₂800CB. It was also observed that the same thermal debinding conditions could impact samples of different geometries in different intensity regarding their C balance, if the printing led to larger cavities and thus a larger inner surface and a higher reactivity. In two cases the support plate made from C influenced the C level, slightly raising it in limited areas. This was the first and only observable impact of the support plate material. Also, different printing parameters lead to different material infills and thus the mass loss cannot be fully reproduced even if the dimensions of the printed samples do not change significantly.

4.5 3rd series

In this chapter the 3rd series' results will be presented and discussed.

4.5.1 Printing parameters

The printing parameters are listed in Tab. 7.

Tab. 7 Printing parameters of the 3rd series

	Row width (mm)	T _{Nozzle} (°C)	T _{Bed} (°C)	Print speed (mm/s)	Flow rate (%)	Nozzle diam. (mm)
Set 1	0.1	250	95	10	105	0.2

4.5.2 Mass loss and shrinkage of the 3rd series

In this subchapter the mass loss is presented and discussed. Fig. 38 shows the results for each sample of this series.

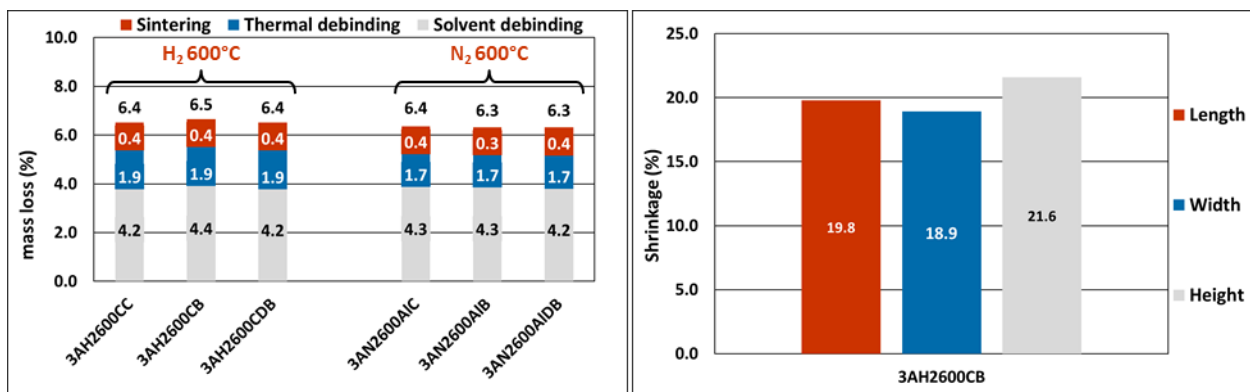


Fig. 38 Left: mass loss of the 3rd series, right: shrinkage of sample 3AH₂600CB

The mass loss during solvent debinding is similar compared to the 2nd series. The small deviations are most likely a result of different organic material infill, either because of the varied printing parameters or an inhomogeneous distribution of the ready-to-use binder and the powder. The mass loss during thermal debinding under H₂ is about the same and under N₂ by 0.2% smaller compared to the 2nd series. As nothing changed in the experimental process after the printing, the printing parameters and thus a different amount of organic binder or a different inner surface and reactivity due to a different level of cavitation are the likeliest explanations for the deviations.

The shrinkage measured on a representative sample confirms previous results where the shrinkage in height is a little larger than the shrinkage in the other two directions.

4.5.3 Magnetic properties of the 3rd series

In this subchapter the magnetic properties are presented and discussed. Fig. 39 shows the results for each sample of this series.

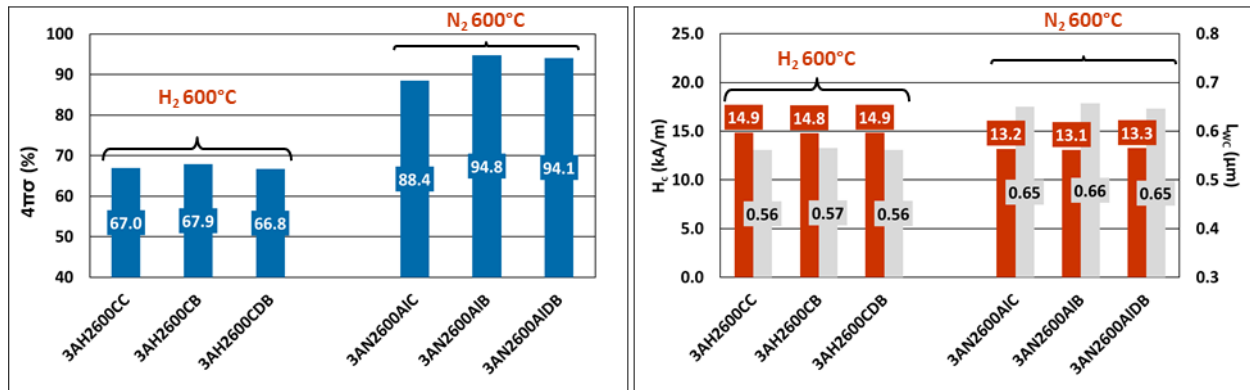


Fig. 39 Left: magnetic saturation of the 3rd series, right: coercive force and L_{WC} of the 3rd series

The magnetic saturation values of the H₂ debinded samples are lower compared to the 2nd series and lie more in the range of the 1st series. The reason could be the same hypothesis which was discussed in 4.4.3 *Magnetic properties*. As will be shown in the next subchapter, the cavity situation worsened in this sample series compared to the previous ones. A larger inner surface could be affected more by the same H₂ concentration and temperature and thus the C level would sink by a larger amount. The magnetic saturation values of the N₂ debinded samples are also lower by a small amount compared to the previous series, except for the cone sample, which is significantly lower. The reason for this difference is most likely once again the higher number of cavities and the higher reactivity towards C loss, as the samples were debinded together using the same process parameters. All samples are below the 95% threshold and are two-phased, which is a novum compared to the previous samples debinded under N₂ up to 600°C.

The coercive force values differ slightly from the ones in the previous series, which could also be due to different cavity levels and thus different reactivity. The debinding under H₂ leads to finer grains than the debinding under N₂.

4.5.4 LOM results of the 3rd series

In this subchapter the LOM images are presented and discussed. Fig. 40 to Fig. 43 show the images for each sample of this series.

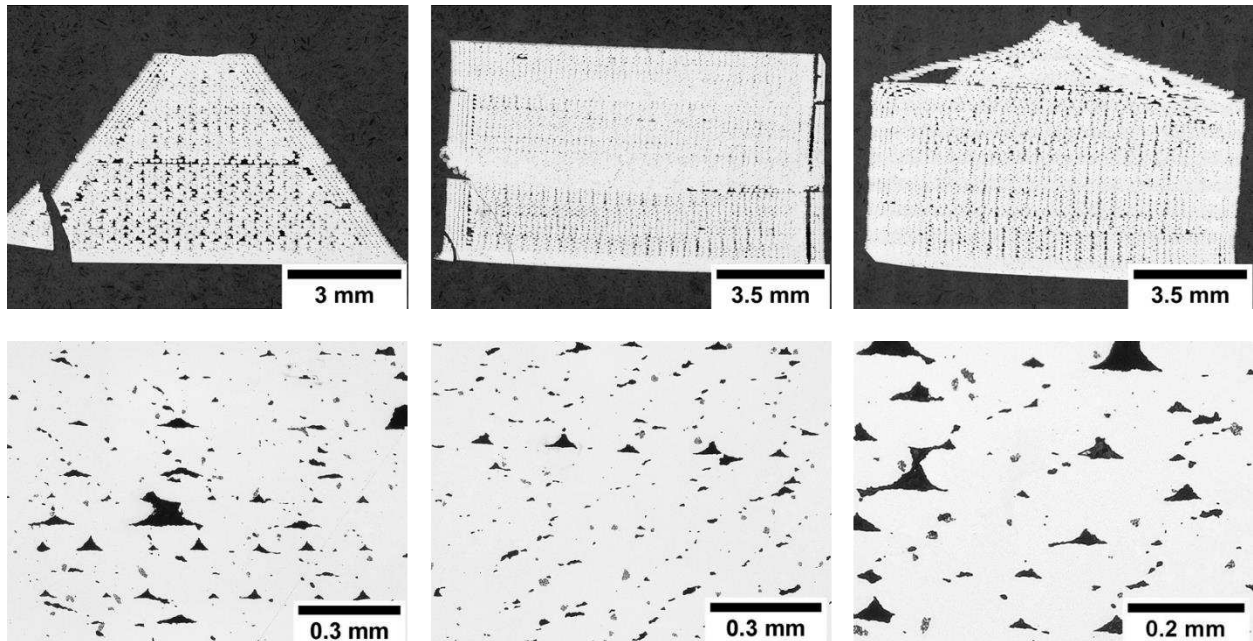


Fig. 40 From left to right: 3AH₂600CC, 3AH₂600CB, 3AH₂600CDB

The left images display a cone's vertical cross section and the respective magnified part. On the borders left and right the cavities going up diagonally can be seen which stem from the poor bonding in the interface region. In the samples centre there are larger cavities in large quantity, while the first few layers at the bottom where printed almost cavity-free. There is η phase present throughout the whole sample.

The central images display a block's vertical cross-section and the respective magnified part. Especially on the right side the interface cavities are clearly visible. There cavities are present in the whole sample except for a few layers at the bottom, a larger zone located the middle and in the first few layers of the top quarter. There is η phase present throughout the whole sample.

The right images display a drill bit's vertical cross-section and the respective magnified part. Cavities are most prominent in the centre and not as much on the sides, there is a large cavity at the left top which is a result of the cut being made exactly through an indentation which is part of the desired shape (compare to Fig. 3). There is η phase present throughout the whole sample.

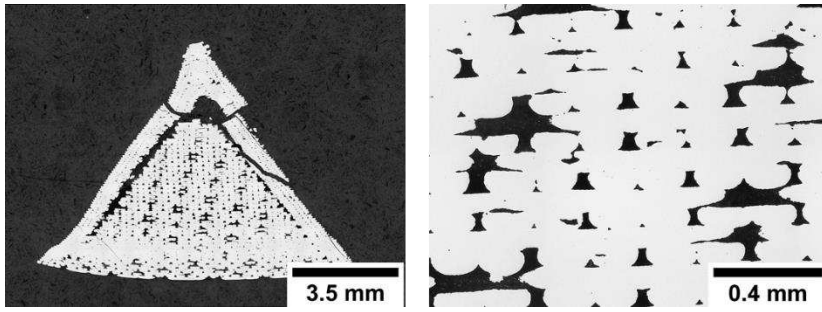


Fig. 41 From left to right: 1AN₂600AIC, 1AN₂600AIC (magnified)

The images above show a cone's vertical cross-section and the respective magnified part. Even though the tip broke off during embedding, the large cavities in the interface region are clearly visible. The rest of the sample is affected by large cavities as well, except for the border region itself and a small area after a few layers at the bottom. The sample is two-phased.

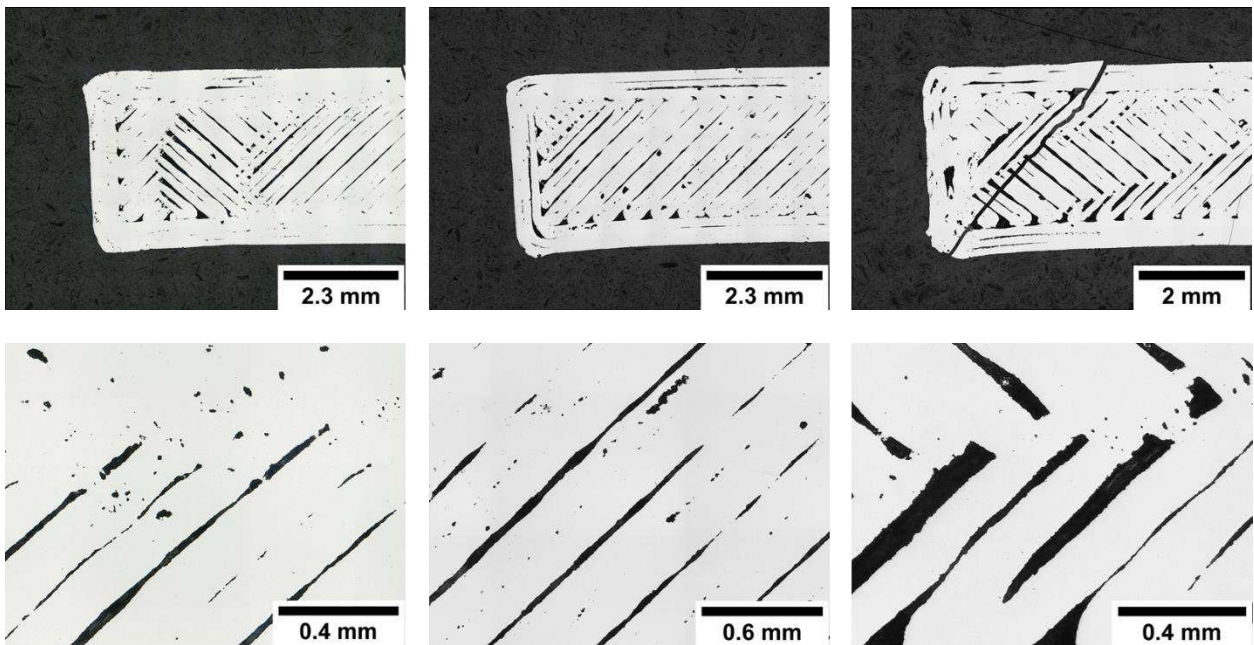


Fig. 42 From left to right: 3AN₂600AIB (bottom), 3AN₂600AIB (middle), 3AN₂600AIB (top)

The images above each show one half of a block's horizontal cross section at three different planes and the respective magnified parts. All three prepared levels of the block exhibit large cavity areas resulting from unsuccessful bonding. The rows of the zigzag printing strategy in the centre as well the ones of the rectangular printing strategy at the border are clearly visible. The sample is two-phased at all three different levels, which is in correspondence to the magnetic saturation results.

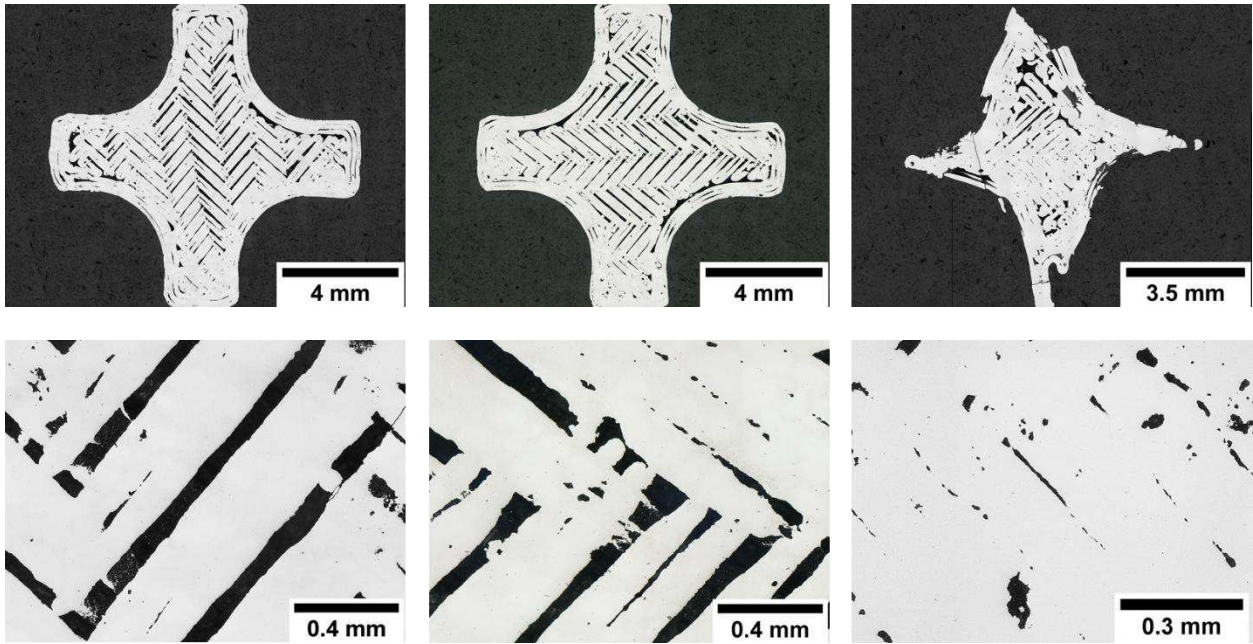


Fig. 43 From left to right: 3AN₂600AIDB (bottom), 3AN₂600AIDB (middle), 3AN₂600AIDB (top)

The images above each show one half of a drill bit's horizontal cross section at three different planes and the respective magnified parts. Just like the in previous sample, there are large cavities from poor row bonding present. The previous and this sample are an example of how the angle of the zigzag printing strategy changes after every layer by 90°. The sample is two-phased at every investigated level.

4.5.5 Summary of the 3rd series

Concluding, the 3rd series exhibited large cavity areas compared to the previous series which also led to a higher C loss at the same thermal debinding parameters, deeming the set of printing parameters used for the 3rd series unfavourable compared to the other parameter sets. While the H₂ debinded samples showed the presence of η phase, the N₂ debinded samples were two-phased opposed to the previous samples, even though the thermal debinding program was not changed. This underlines the different impact of the same conditions on samples of different cavity levels, sizes, and orientations. Interestingly though the mass loss during thermal debinding was lower compared to the 2nd series even though the 2nd series samples showed higher C levels both for the H₂ and the N₂ debinded samples (compare 4.5.3 *Magnetic properties of the 3rd series* with 4.4.3 *Magnetic properties of the 2nd series*). The mass loss during solvent debinding however was slightly higher, meaning that the large cavities of the 3rd series might have led to additional organic material already being dissolved in cyclohexane. Therefore, not being removable anymore during thermal debinding, led to additional C originally stemming from the hardmetal powder itself being removed leading to a lower C balance at lower mass loss during thermal debinding.

4.6 4th series

In this chapter the 4th series' results will be presented and discussed.

4.6.1 Printing parameters of the 4th series

The printing parameters are listed in Tab. 8.

Tab. 8 Printing parameters of the 4th series

	Row width (mm)	TNozzle (°C)	TBed (°C)	Print speed (mm/s)	Flow rate (%)	Nozzle diam. (mm)
Set 1	0.1	250	95	10	122	0.2

4.6.2 Mass loss and shrinkage of the 4th series

In this subchapter the mass loss is presented and discussed from thermal debinding to the fully sintered samples. Fig. 44 shows the results for each sample of this series.

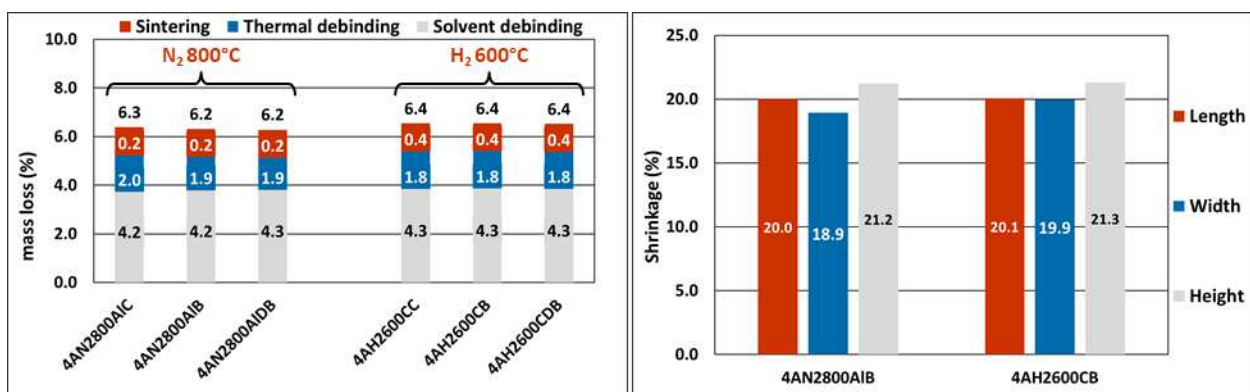


Fig. 44 Left: mass loss of the 4th series, right: shrinkage of sample 4AN₂800AIB and 4AH₂600CB

The mass loss during solvent debinding resembles the mass loss results of the 2nd and 3rd series and is slightly higher compared to the 1st series. The mass loss during thermal debinding under N₂ up to 800°C is higher compared to the 1st and 2nd series by 0.1 to 0.3%. A slower printing speed and a similar flow rate might have led to more feedstock and thus organic binder being filled into the printed part, which could be an explanation for the higher mass loss, however it is unclear why the mass loss during solvent debinding did not rise as well. The mass loss under H₂ up to 600°C debinding resembles the previous results

The shrinkage results of the investigated samples correspond to previous samples, where the shrinkage in height was a little larger than in the other two directions.

4.6.3 Magnetic properties of the 4th series

In this subchapter the magnetic properties are presented and discussed. Fig. 45 shows the results for each sample of this series.

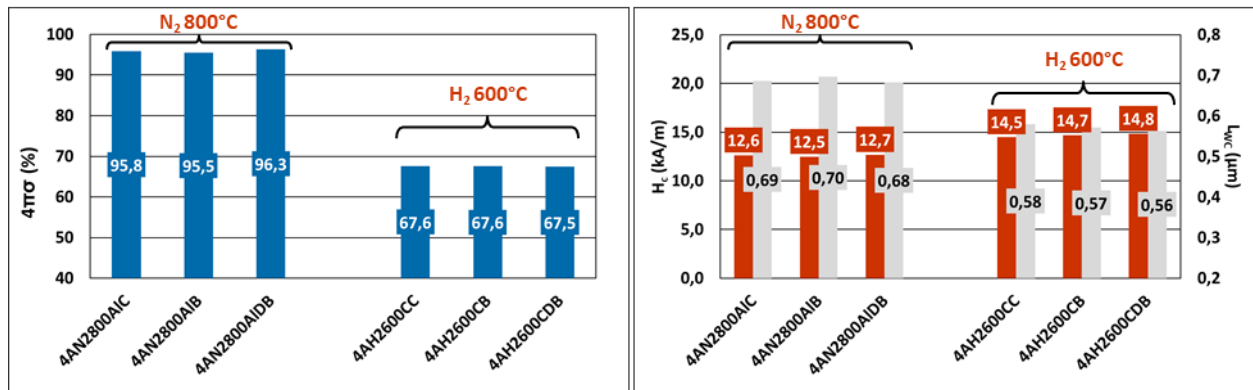


Fig. 45 Left: magnetic saturation of the 4th series, right: coercive force and L_{WC} of the 4th series

The samples that were debinded under N₂ lie in the free C region slightly over the 95% threshold, whereas the samples which were debinded under H₂ lie in the η region. The values of the N₂ debinded samples are slightly lower than the ones from the 1st and 2nd series and are almost in the two-phase region. The results of the H₂ debinded samples resemble the results of the 1st and the 3rd series.

The coercive force values confirm the previous results in which N₂ leads to coarse grains than H₂.

4.6.4 LOM results of the 4th series

In this subchapter the LOM images are presented and discussed. Fig. 46 to Fig. 51 show the images for each sample of this series.

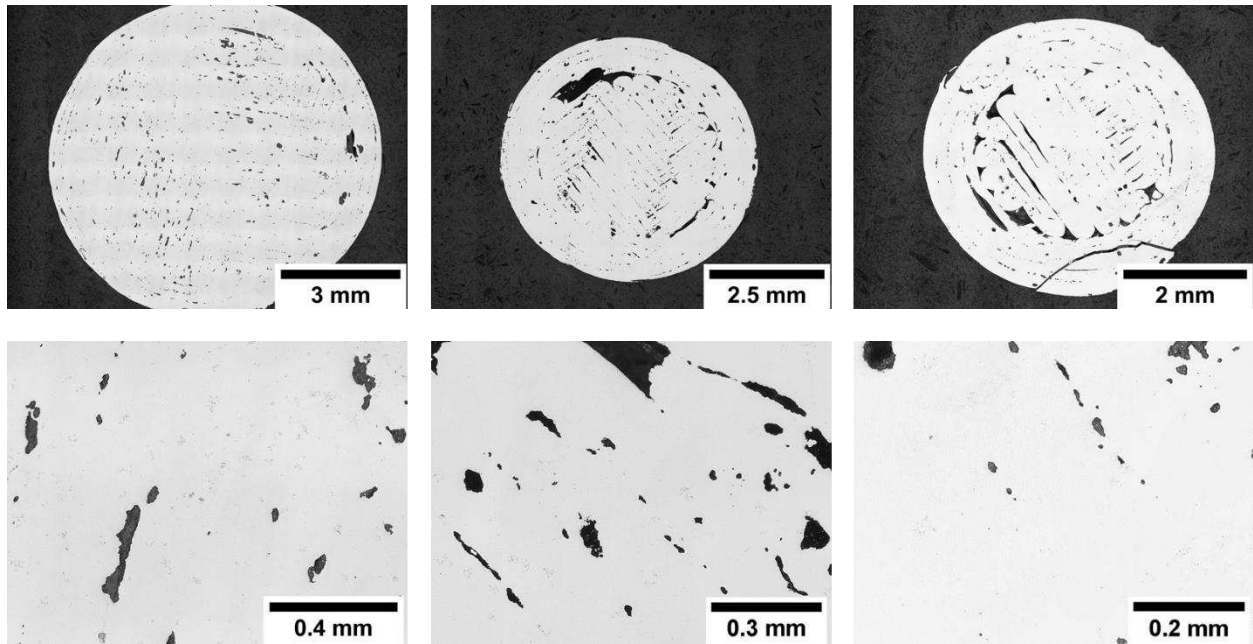


Fig. 46 From left to right: 4AN₂800AIC (bottom), 4AN₂800AIC (middle), 4AN₂800AIC (top)

The images above each show a cone's horizontal cross section at three different planes and the respective magnified parts. Especially in the central and the right images the interface region cavities are observable. The circular border printing strategy as well as the zigzag printing strategy in the centre led to inadequate bonding just as in the previous series. The bottom of the sample seems to be less affected by cavities than the middle and the top. The whole sample displays free C.

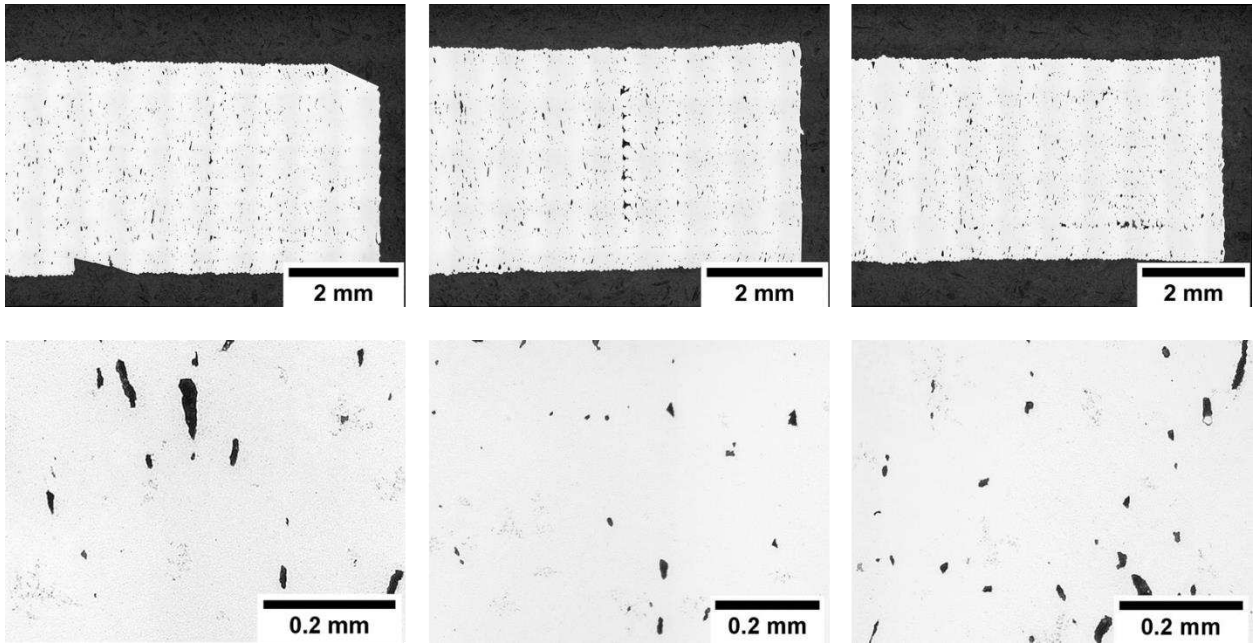


Fig. 47 From left to right: 4AN₂800AIB (left), 4AN₂800AIB (middle), 4AN₂800AIB (right)

The images above each show one half of a block's vertical cross section at three different planes rotated 90° to the left and the respective magnified parts. Except for a small region in the centre of the middle cross section and one on the upper left edge of the right cross section, no large cavities are visible. The residual cavities throughout the sample are smaller and round shaped resembling conventional pores. Corresponding to the magnetic saturation results, the sample exhibits free C.

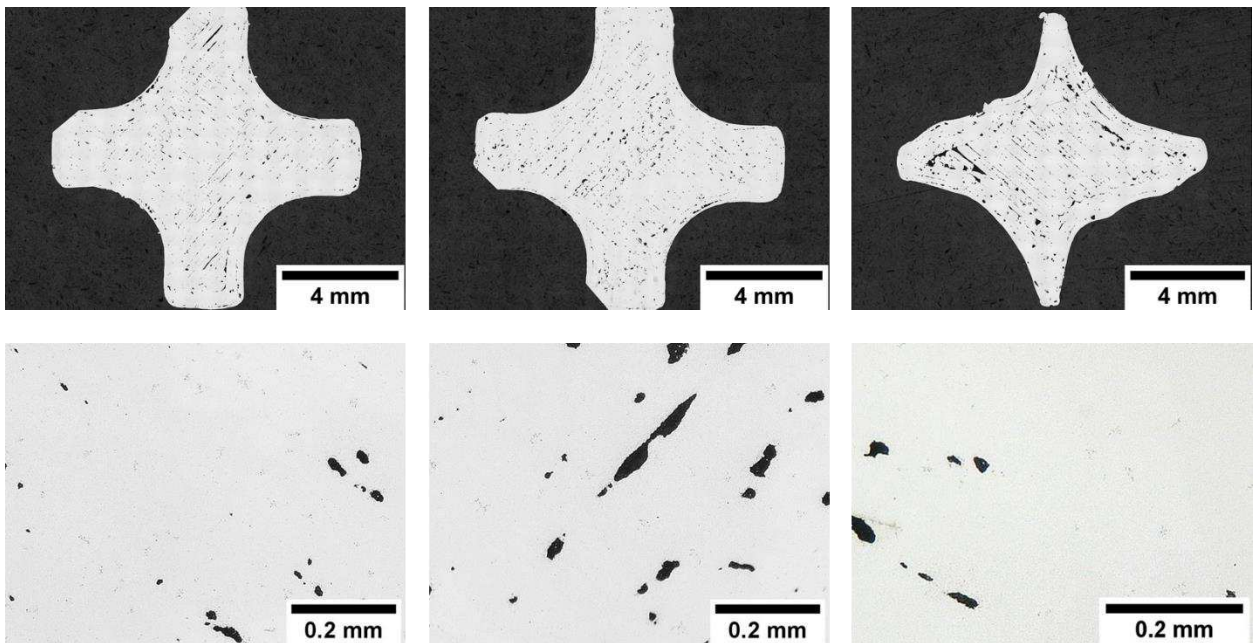


Fig. 48 From left to right: 4AN₂800AIDB (bottom), 4AN₂800AIDB (middle), 4AN₂800AIDB (top)

The images above each show a drill bit's horizontal cross section at three different planes and the respective magnified parts. The interface cavities between rim and centre can be

observed at the bottom flank of the bottom cross section and prominently at the top cross section. The cavities stemming from poor bonding during the zigzag printing are visible at all three cross sections. All three cross section exhibit free C.

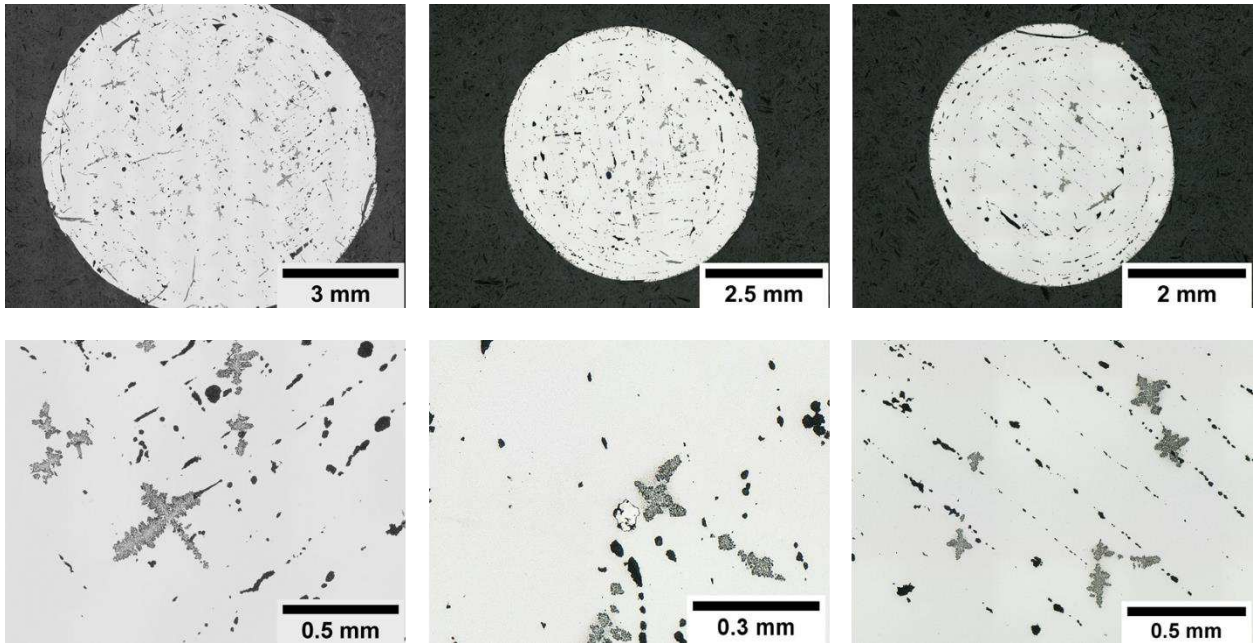


Fig. 49 From left to right: 4AH₂600AIC (bottom), 4AH₂600AIC (middle), 4AH₂600AIC (top)

The images above each show a cone's horizontal cross section at three different planes and the respective magnified parts. In all three planes the border, interface and zigzag cavities are present. The cavities only indicate the printing strategy though, as they are round shaped and not connected, especially at the bottom and the middle cross section. All three cross sections display η phase.

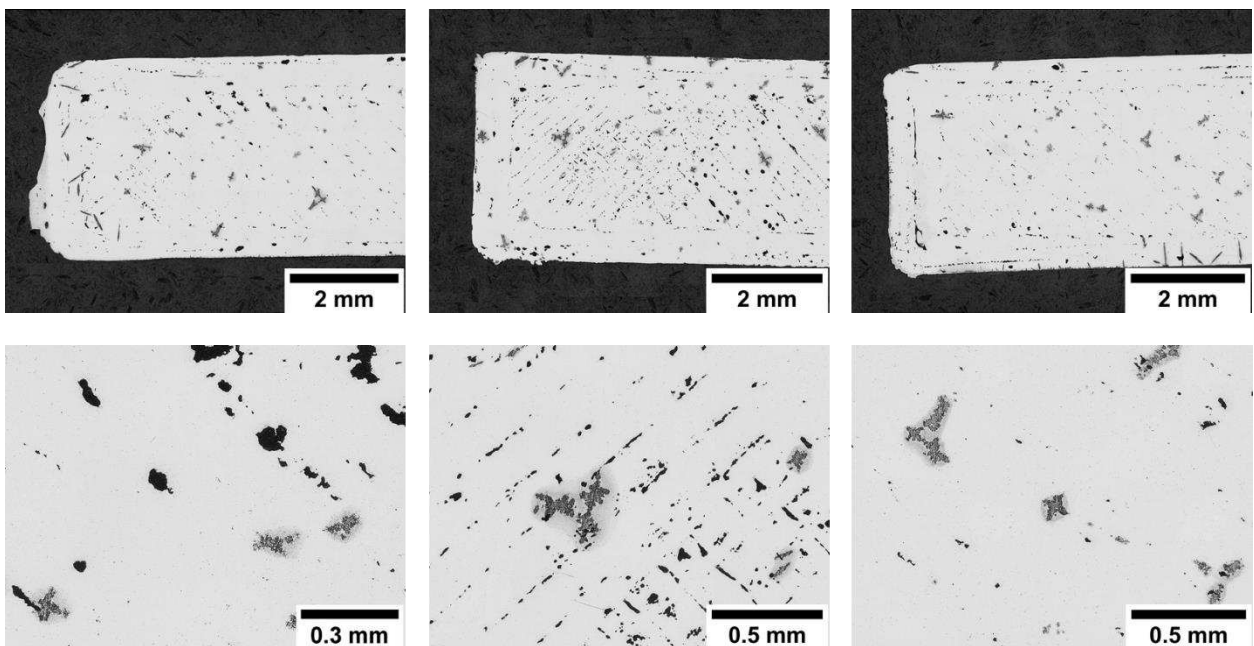


Fig. 50 From left to right: 4AH₂600AIB (bottom), 4AH₂600AIB (middle), 4AH₂600AIB (top)

The images above each show one half of a block's horizontal cross section at three different planes and the respective magnified parts. At all three levels cavities are present in the border region, the interface region, and in the centre each in their distinguished form resulting from the nozzle path. η phase is observable at the bottom, the middle and the top cross section.

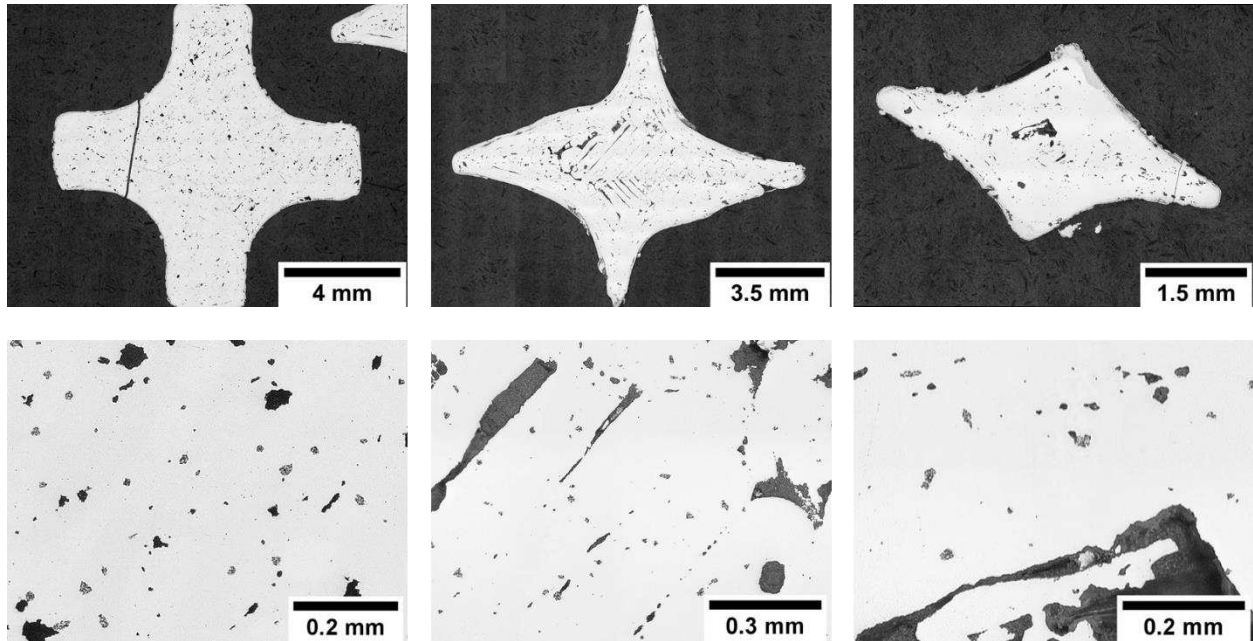


Fig. 51 From left to right: 4AH₂600AIDB (bottom), 4AH₂600AIDB (top), 4AH₂600AIDB (tip)

The images above each show a drill bit's vertical cross section at three different planes and the respective magnified parts. The cavities are prominent in the sample's upper region, where the printing path can be seen clearly. The bottom seems denser and the cavities are smaller. The η phase looks small and atypical compared to the flowers and is distributed throughout the whole sample. At the outermost surface, a fine dispersed η phase can be seen.

4.6.5 Summary of the 4th series

The 4th series was produced using a slower printing speed which resulted in generally denser bodies compared to the previous series except for a few samples from the 2nd series (2N₂600CC, 2AN₂600CDB). The mass loss during solvent debinding resembled previous series. The mass loss during thermal debinding under N₂ up to 800°C was slightly higher than the one in the 1st and 2nd series but the one under H₂ up to 600°C was similar to the previous results. The magnetic saturation results and the metallographic specimen corresponded. While the H₂ atmosphere lowered the samples into the η region, the debinding under N₂ was not enough to lower the sample into the two-phase region. The last part is especially interesting as N₂ and heating up to only 600°C was enough for the previous series to drop into the two-phase region, while heating up to higher temperatures did not result in two-phased samples in this series.

4.7 5th series

In this chapter the 5th series' results will be presented and discussed.

4.7.1 Printing parameters of the 5th series

The printing parameters are listed in Tab. 9.

Tab. 9 Printing parameters of the 5th series

	Row width (mm)	T _{Nozzle} (°C)	T _{Bed} (°C)	Print speed (mm/s)	Flow rate (%)	Nozzle diam. (mm)
5a 5c, 5d, 5e, 5f	0.1	250	95	10	layer 0 to 19: 100 layer 20 to end: 115	0.2
5b	0.1	250	95	9	layer 0 to 10: 100 layer 11 to end: 115	0.2
5g	0.1	250	95	layer 0 to 5: 10 layer 6 to 40: lin. increase to 23 layer 41 to 80: 23 layer 81 to end: 13	layer 0 to end: 117	0.2
5h	0.1	250	95	layer 0 to 3: 10 layer 4 to 85: 23 layer 86 to end: 13	layer 0 to end: 117	0.2
5i, 5j, 5k, 5l	0.1	250	95	layer 0 to 3: 10 layer 4 to end: 23	layer 0 to end: 117	0.2

In the 5th series a new approach was chosen. The print speed and the flow rate were no longer kept constant and were varied depending on the current height of the printed object. In the first experiments the print speed was kept constant and the flow rate was varied. The flow rate of the first printed was lower than the one of the previous series and was raised to a value resembling the previous sample's flow rates. From "5g" onwards the flow rate was kept constant and the print speed was raised during printing. While the print speed of the first few layers roughly resembled the value from previous series, it was set to 23 mm/s afterwards, which is faster than in the previous series. The parameters were changed manually depending on the infill quality determined by the operator at MU Leoben.

4.7.2 Mass loss and shrinkage of the 5th series

In this subchapter the mass loss and the shrinkage are presented and discussed from thermal debinding to the fully sintered samples. Fig. 52 to Fig. 54 show the results for each sample of this series.

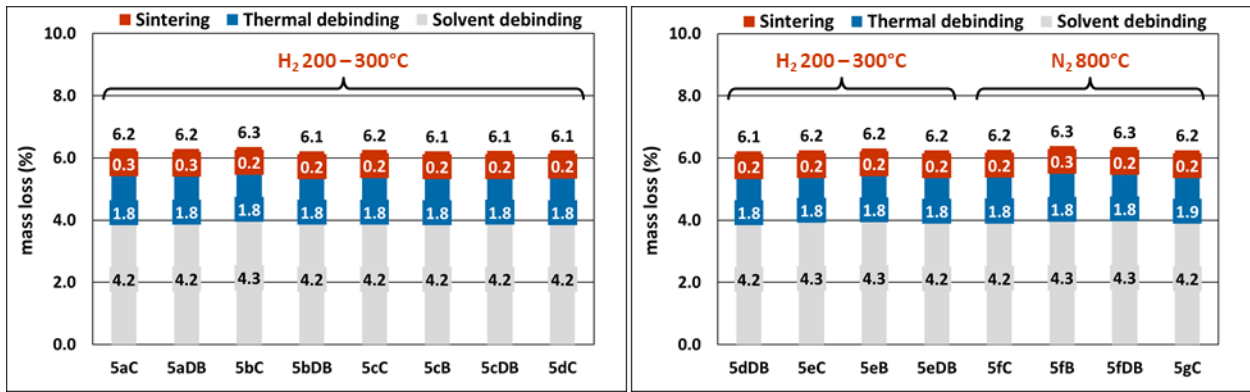


Fig. 52 Mass loss of the 5th series

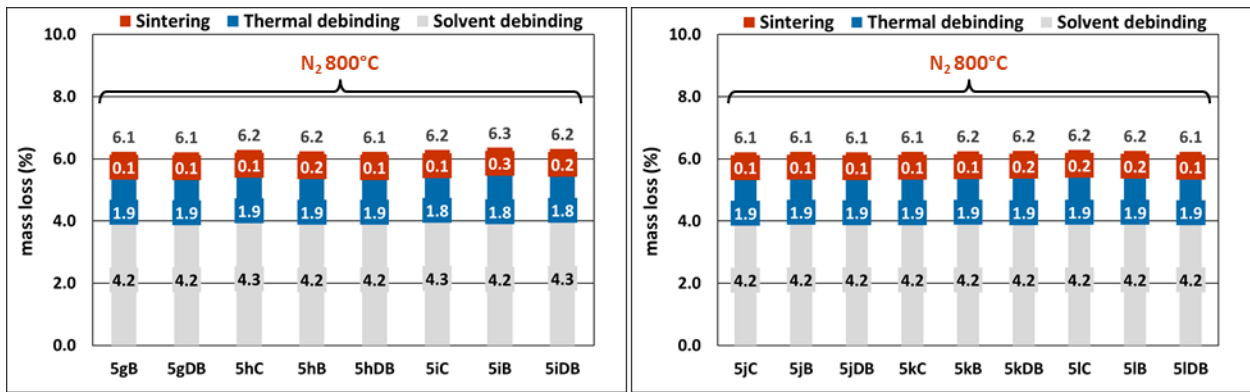


Fig. 53 Mass loss of the 5th series (continuation)

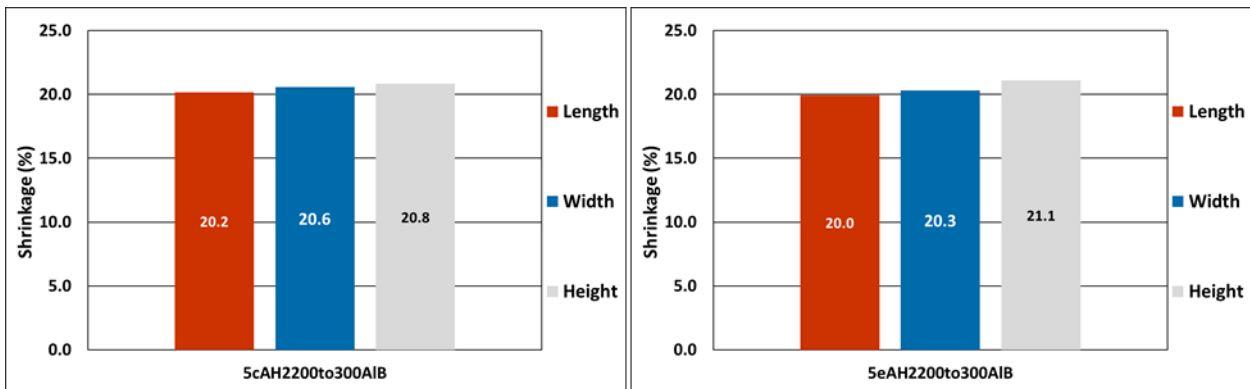


Fig. 54 Shrinkage of sample 5cAH₂200to300AIB and 5eAH₂200to300AIB

The mass loss during solvent debinding is similar throughout all the samples of the 5th series. A mass loss of approximately 4.2% corresponds to the previous series. The mass loss during thermal debinding of 1.8 to 1.9% corresponds to the previous results as well. On some samples of the 5th series a mixed gas treatment was applied during thermal debinding. The samples were debinded under N₂ and from 200 to 300°C the atmosphere was switched do H₂. The two different approaches do not result in a different mass loss during thermal debinding. There is also difference in mass loss depending on the printing strategy.

The shrinkage results of two representative block samples confirm previous results where the shrinkage of the samples height is larger than the shrinkage of the other two dimensions.

4.7.3 Magnetic properties of the 5th series

In this subchapter the magnetic properties are presented and discussed. Fig. 55 to Fig. 58 show the results for each sample of this series.

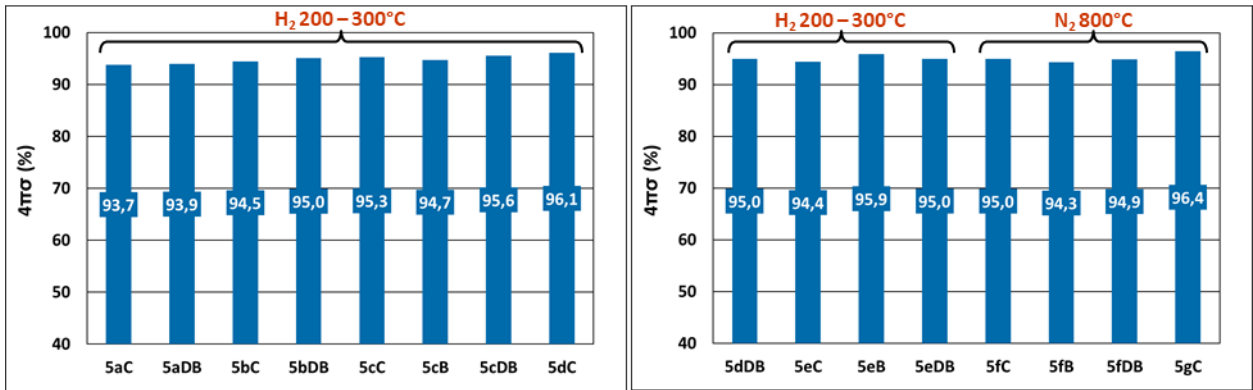


Fig. 55 Magnetic saturation of the 5th series

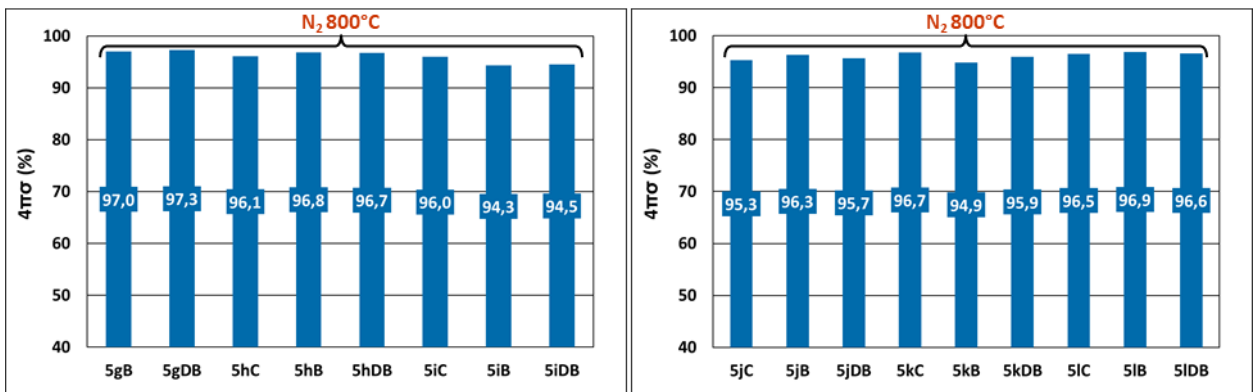


Fig. 56 Magnetic saturation of the 5th series (continuation)

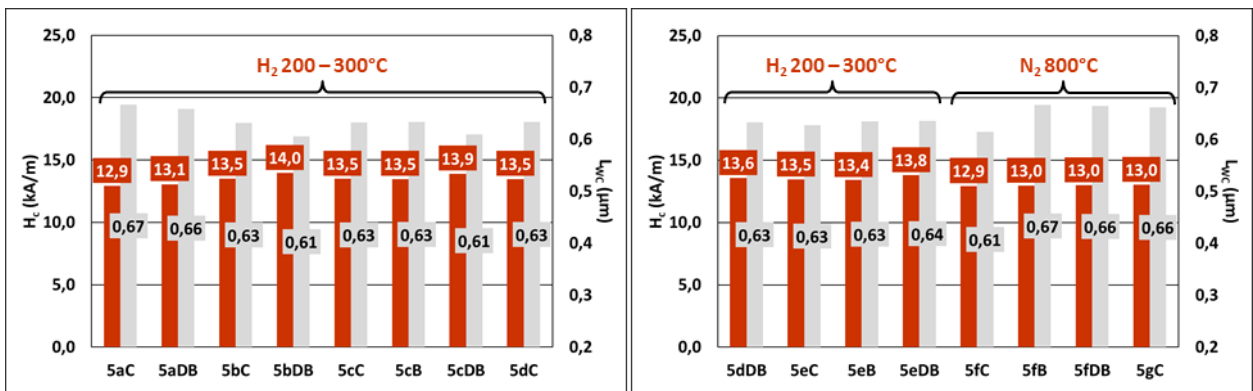


Fig. 57 Coercive force of the 5th series

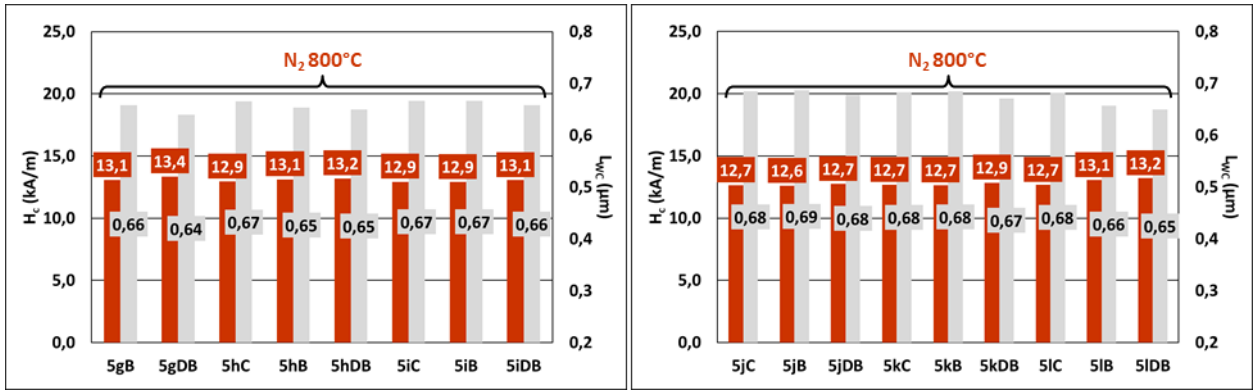


Fig. 58 Coercive force of the 5th series (continuation)

The magnetic saturation results are all similar throughout the 5th series' samples. The samples debinded under N₂ result in saturation values of roughly 95% which is exactly the threshold towards the free C region. Whether the samples are in the two-phase region or in the free C region will be determined through the metallographic specimen. The treatment with mixed atmospheres produces the same results as the samples which were debinded solely under N₂. This is an indication that the treatment under H₂ happened at too low temperatures or was of too short duration to lower the C balance enough to reach the two-phase region.

The coercive force values confirm that there is no significant difference in the results of the different debinding programs. The partial treatment with H₂ was not impactful enough to prevent the grain growth process through N₂.

4.7.4 LOM results of the 5th series

In this subchapter the LOM images are presented and discussed. Fig. 59 to Fig. 86 show the images for each sample of this series.

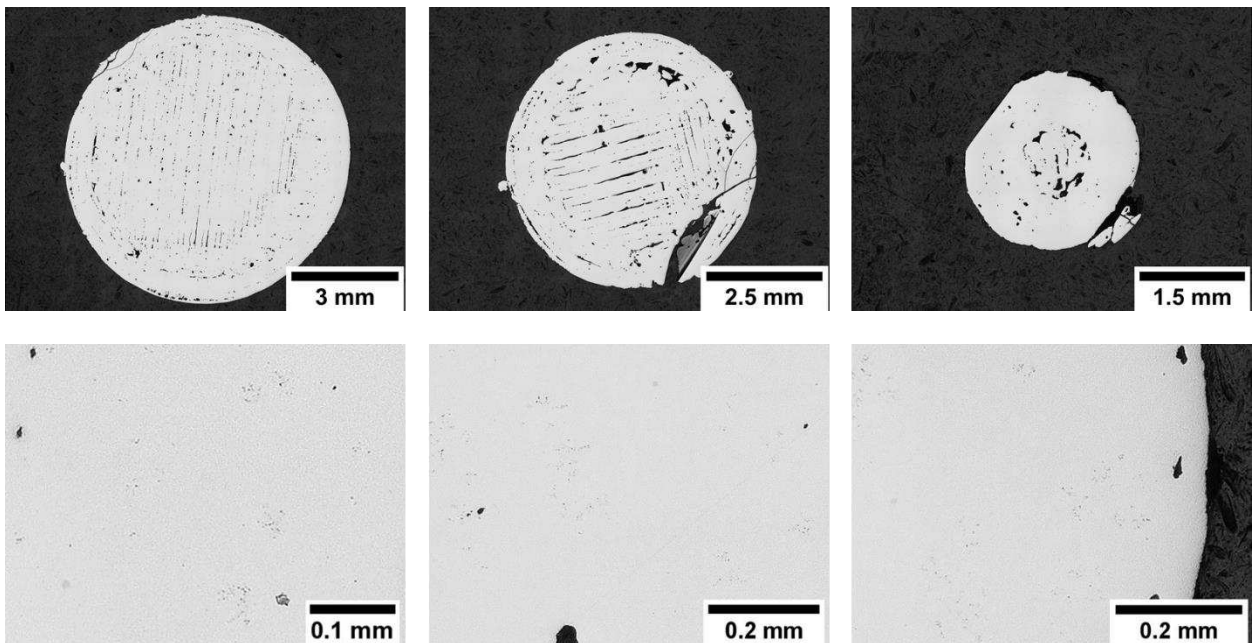


Fig. 59 From left to right: 5aC (bottom), 5aC (middle), 5aC (top)

The images above each show a cone's horizontal cross section at three different planes and the respective magnified parts. At all three levels the sample shows the typical cavities stemming from the interface region and the centre region, each with their characteristic shape. While the middle and the top of the sample are more affected, the bottom seems to be of better quality, although not free from cavities. The sample exhibits free C at all three cross sections.

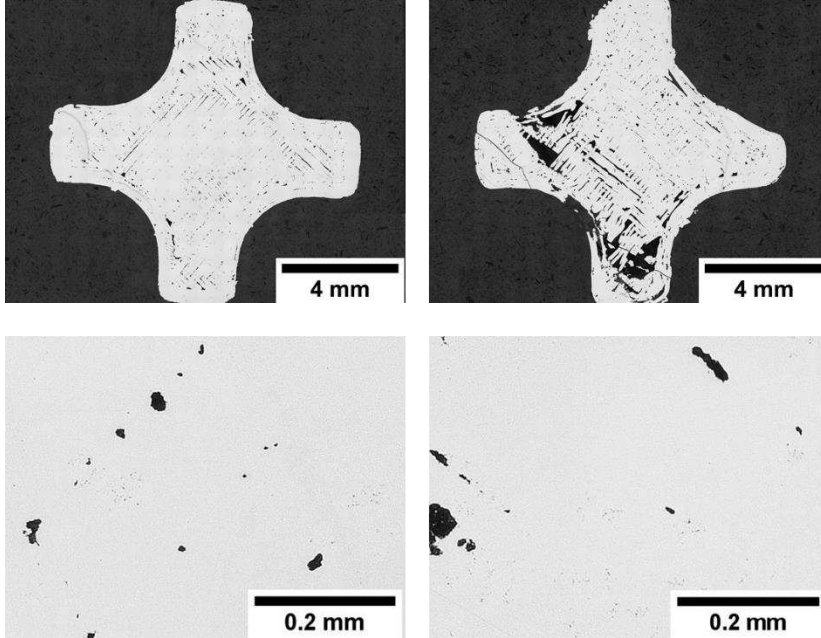


Fig. 60 From left to right: 5aDB (bottom), 5aDB (top)

The images above each show a drill bit's horizontal cross section at two different planes and the respective magnified parts. The border region does not exhibit many cavities. The interface and centre cavities are prominently present especially at the top cross section. The bottom cross section does not have as many cavities, but they are still clearly visible. Free C is present in the whole sample.

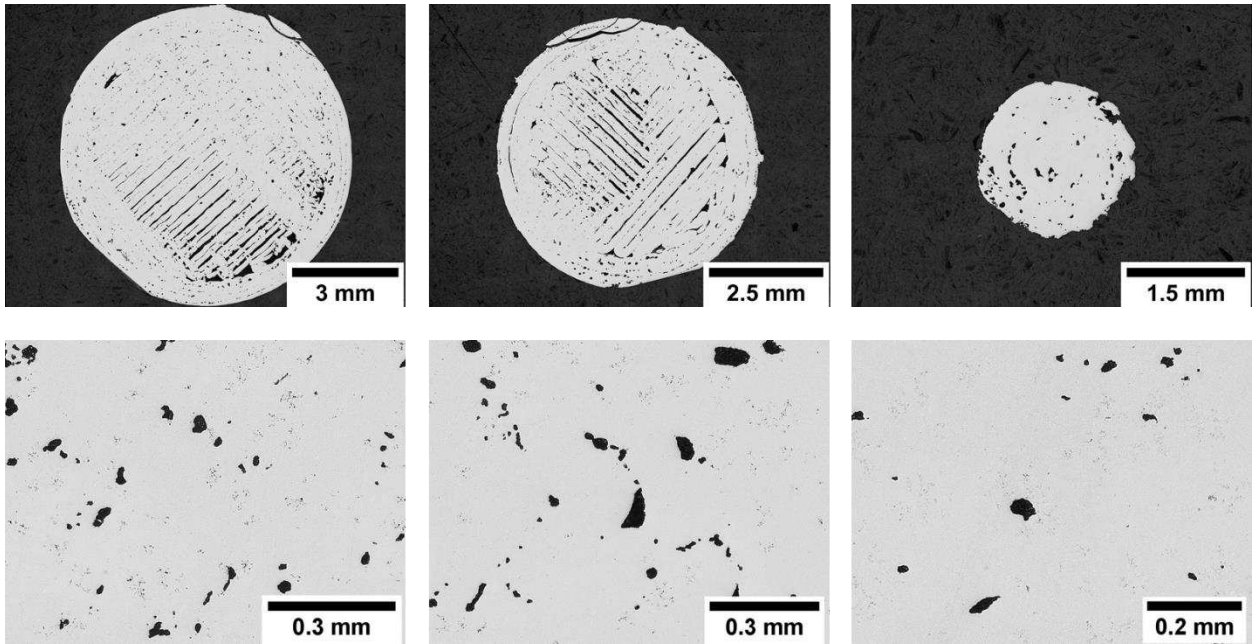


Fig. 61 From left to right: 5bC (bottom), 5bC (middle), 5bC (top)

The images above each show a cone's horizontal cross section at three different planes and the respective magnified parts. The interface and centre cavities are visible especially at the bottom and the middle cross section. The top cross section exhibits lesser cavities. Free C is present in the whole sample.

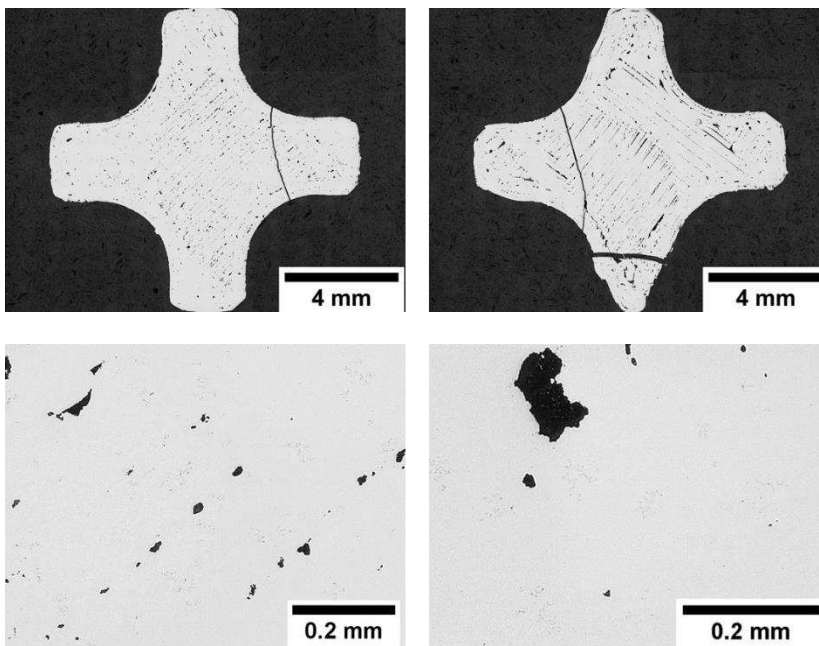


Fig. 62 From left to right: 5bDB (bottom), 5bDB (top)

The images above each show a drill bit's horizontal cross section at two different planes and the respective magnified parts. Alongside some cracks resulting from embedding, the sample exhibits cavities in the centre showing the zigzag printing path. The top cross section shows a higher level of cavitation than the bottom, although this sample seems

of slightly better quality than the previous samples in this series. Free C is visible from bottom to top.

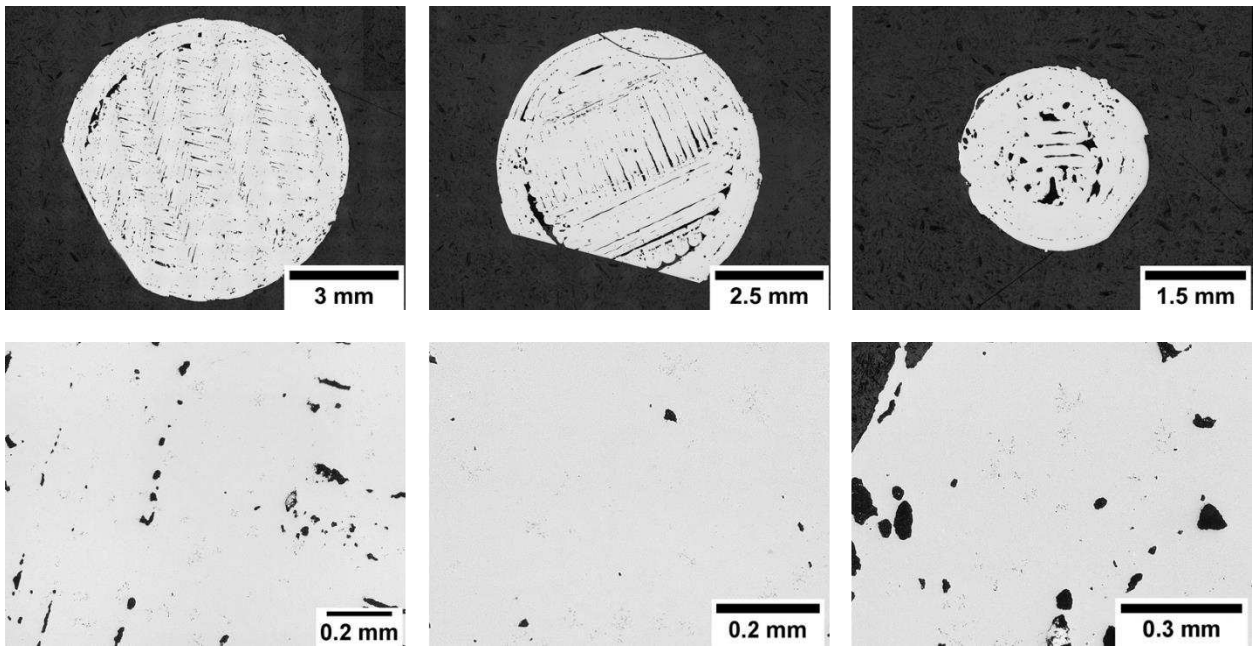


Fig. 63 From left to right: 5cC (bottom), 5cC (middle), 5cC (top)

The images above each show a cone's horizontal cross section at three different planes and the respective magnified parts. In the bottom and the middle cross section a piece of the sample was not stripped entirely from bakelite. Other than that, the sample shows all three types of cavities. The border rows which were printed circular and the zigzag rows in the centre did not bond adequately among themselves. Furthermore, the interface region is also porous as the rows of the different printing paths did not bond with each other, which can be seen in the middle cross section. The whole sample displays free C.

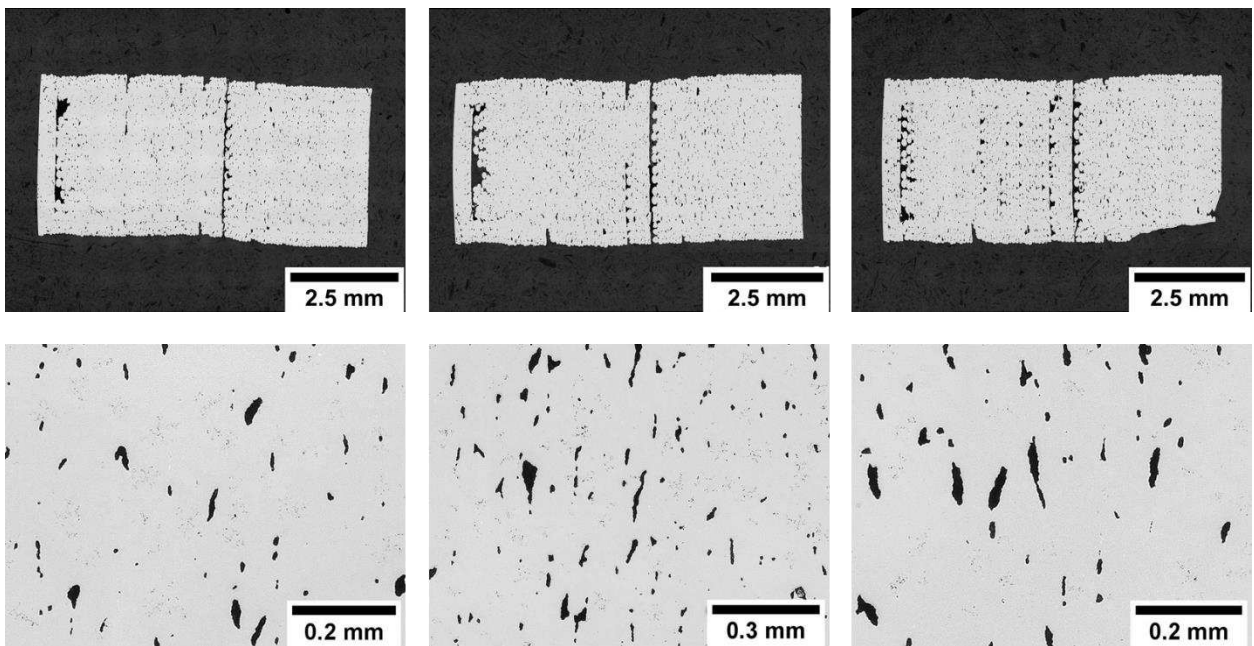


Fig. 64 From left to right: 5cB (left), 5cB (middle), 5cB (right)

The images above each show one half of a block's vertical cross section at three different planes rotated 90° to the right and the respective magnified parts. At all three cross sections two large cavity areas at the sample's bottom and one more in the centre are visible. The cavities which indicated the poor row bonding are not clearly distinguishable in this case. The cavities look round shaped and resemble macropores. Free C is displayed at all three cross sections.

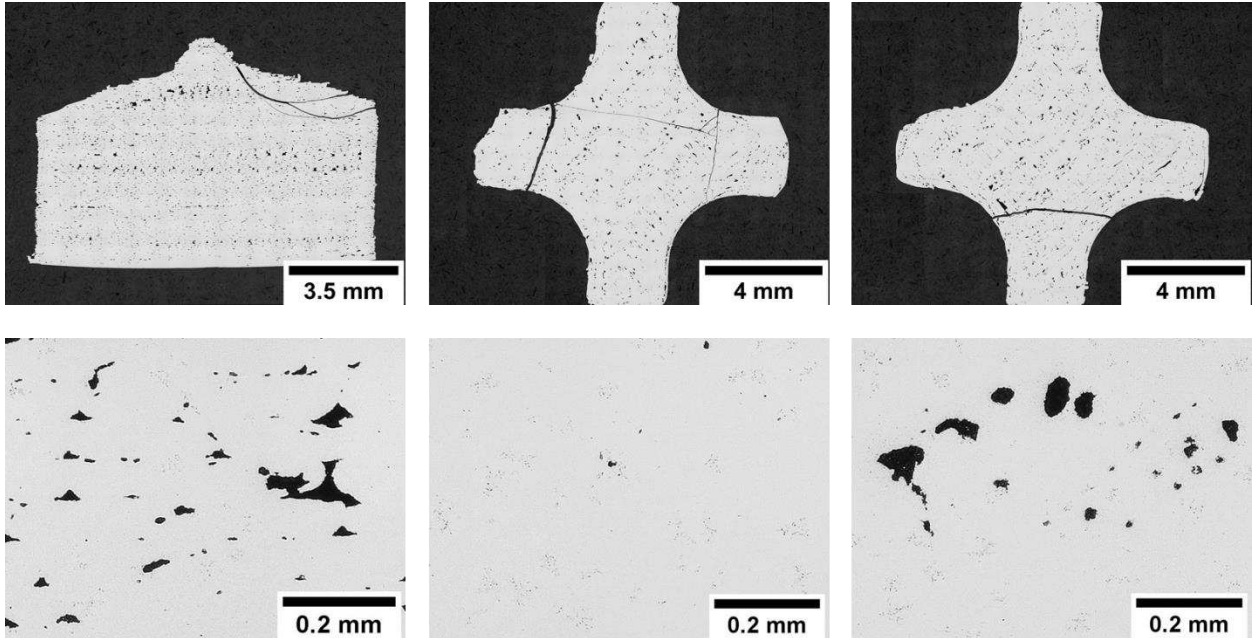


Fig. 65 From left to right: 5cDB, 5dDB (bottom), 5dDB (top)

Two different samples are shown in the images above. The images to the left show a drill bit's vertical cross section and the respective magnified part. The border and the bottom region do not exhibit many cavities compared to the slightly more affected region in the centre. Under the drill bit's tip is a larger area of cavities present. The sample exhibits free C throughout the whole sample volume.

The middle and right images each show a drill bit's horizontal cross section at two different planes and the respective magnified parts. Compared to the previous samples a small number of cavities indicate the printing strategies at the border and the centre. The level of cavitation is about the same for the sample's bottom and the top. Both cross sections show free C.

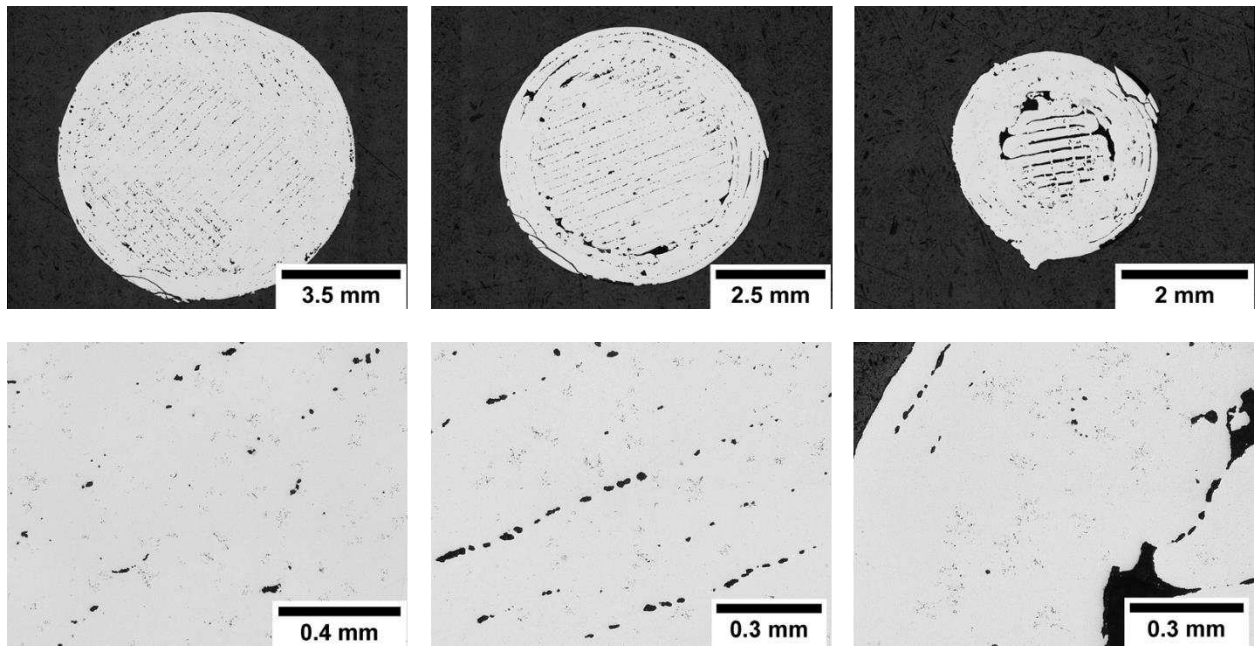


Fig. 66 From left to right: 5dC (bottom), 5dC (middle), 5dC (top)

The images above each show a cone's horizontal cross section at three different planes and the respective magnified parts. The sample displays the typical border, interface and centre cavities resulting from the printing process. The sample's bottom is not as affected as the middle and the top. Free C is present in the whole sample.

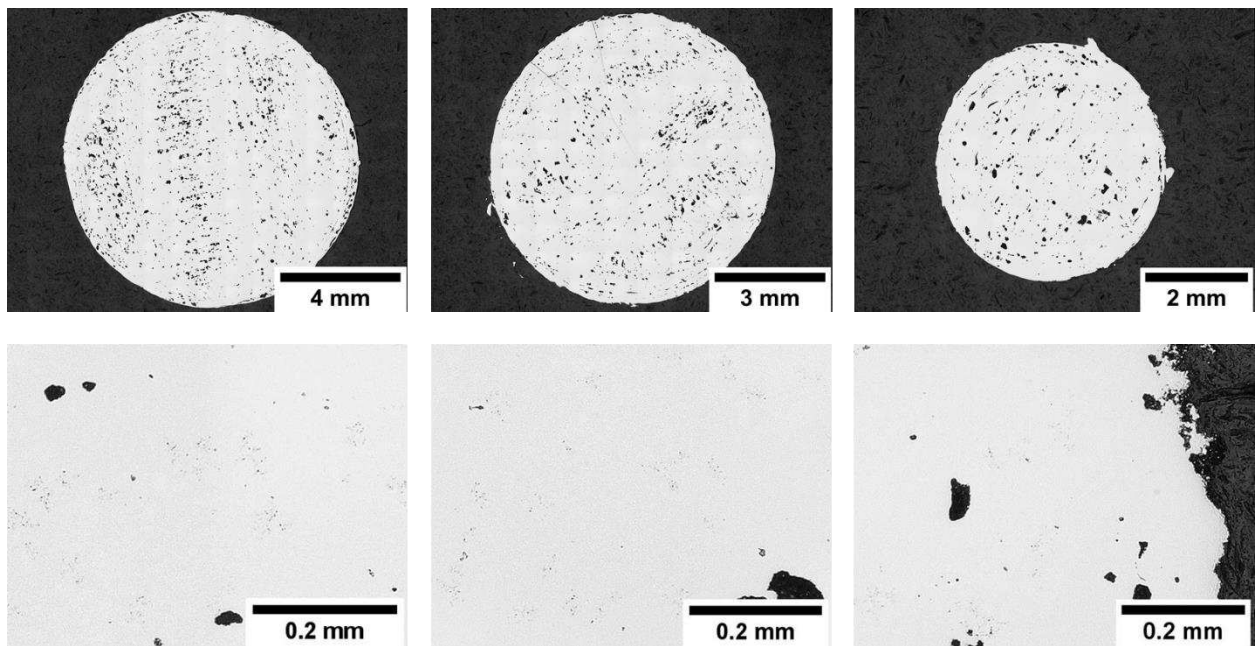


Fig. 67 From left to right: 5eC (bottom), 5eC (middle), 5eC (top)

The images above each show a cone's horizontal cross section at three different planes and the respective magnified parts. All three cross sections exhibit cavities in large amounts but the typical form, stemming from the printing path is not visible anymore. Instead, the cavities are round shaped and resemble regular pores. All cross sections exhibit cavities of the same amount. Free C is visible in every cross section.

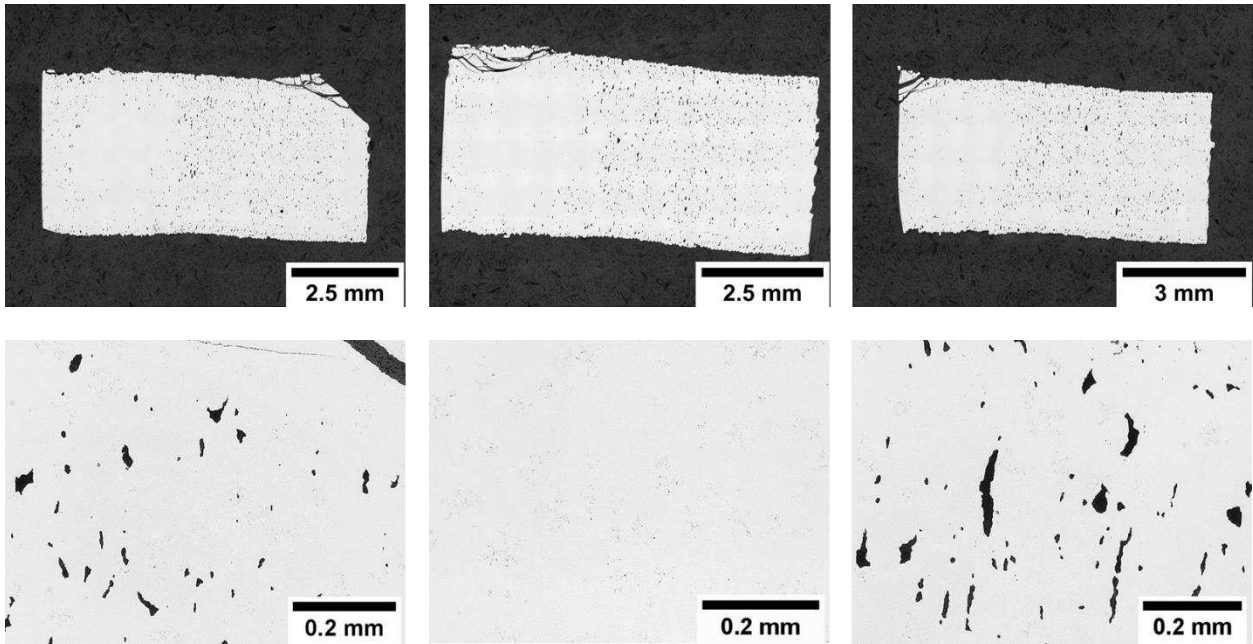


Fig. 68 From left to right: 5eB (left), 5eB (middle), 5eB (right)

The images above each show one half of a block's vertical cross section at three different planes rotated 90° to the right and the respective magnified parts. This sample has a distinct area in the bottom third, that is almost cavity free. The rest of the sample exhibits fewer cavities which are not assignable to any printing path and are round shaped just as in the previous sample.

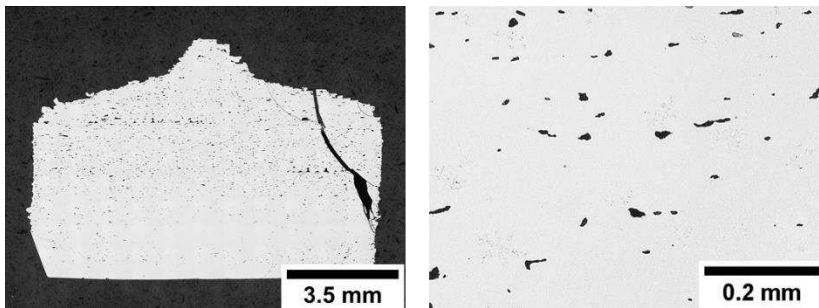


Fig. 69 From left to right: 5eDB, 5eDB (magnified)

The images above display a drill bit's vertical cross section and a magnified part next to it. The sample shows very few cavities in the bottom third which increase going upwards. Some of the cavities are smaller and round shaped and some have the typical shape resulting from poor row bonding especially starting at the top third and next to the right edge. Free C is visible throughout the whole sample.

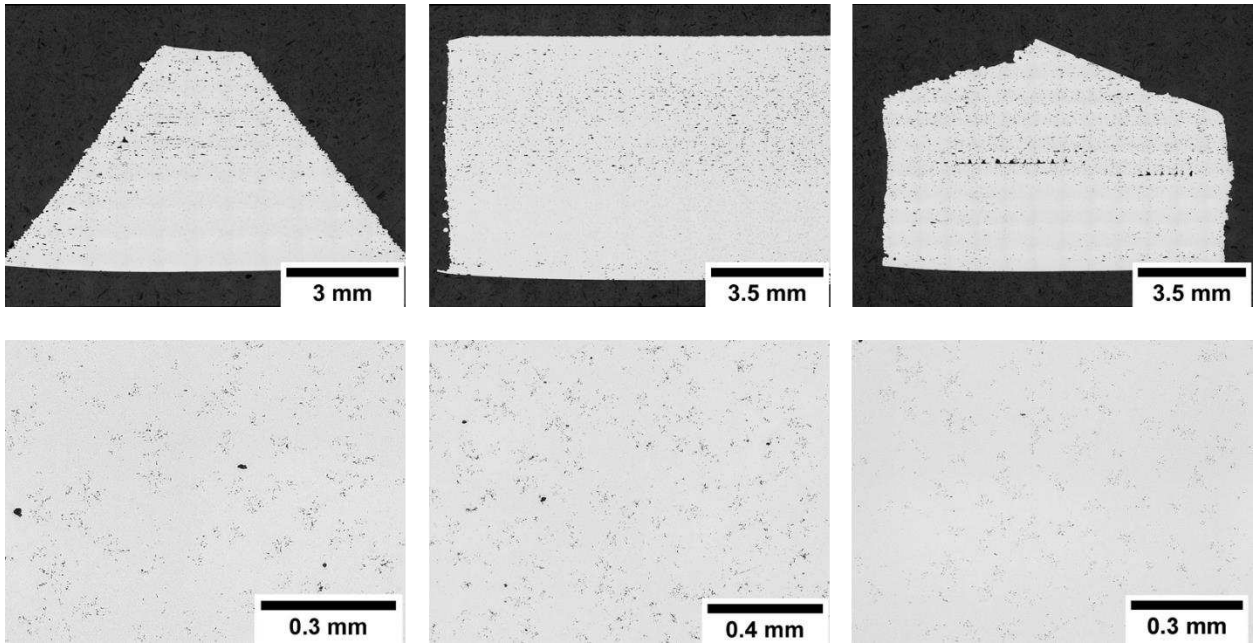


Fig. 70 From left to right: 5fC, 5fB, 5fDB

The left images display a cone's vertical cross section and the respective magnified part. A semi-circular region in the centre of the bottom third is almost dense and only a few small pores are present. The rest of the sample has a variation of cavities, some being round shaped and some larger ones having the typical shape resulting from inadequate row bonding. The sample displays free C.

The middle images display a block's vertical cross section and the respective magnified part. Just as like the previous cone sample, the block is almost dense in the bottom third with rising levels of round cavities which cannot be assigned to a printing path going upwards. Free C is present in the whole sample.

The right images display a drill bit's vertical cross section and the respective magnified part. The cavity situation is the same as in the previous two samples with an almost dense bottom third and a worsening situation going upwards. The drill bit exhibits more cavities than the previous two samples but follows the same trend. In the middle of the sample there is a linear area of larger cavities. Free C is present in the whole sample.

Compared to the 5a, 5c and the 5d samples, which were produced using the same set of printing parameters, in which the flow rate was varied, the 5eB, 5eDB and all 5f samples display a much better cavity situation. This proves that reproducibility of a dense sample is difficult to achieve with this printer setup, let alone when the same set of parameters is used on different geometries and is not tailored to a certain shape.

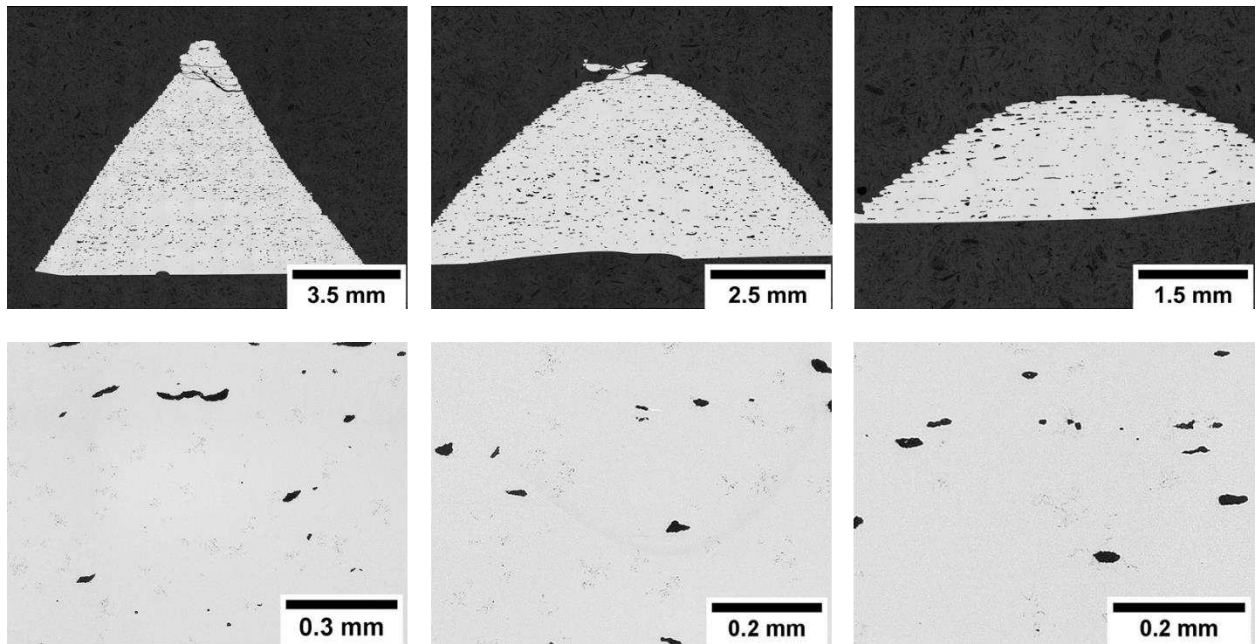


Fig. 71 From left to right: 5gC (cut made: half), 5gC (cut made: third) 5gC (cut made: quarter)

The images above each show a cone's vertical cross section at three different planes and the respective magnified parts. In this case the interface region between border and centre seems to be the densest region in the sample. The rest of the sample is filled with many round cavities not assignable to a printing path. Free C is present at each cross section.

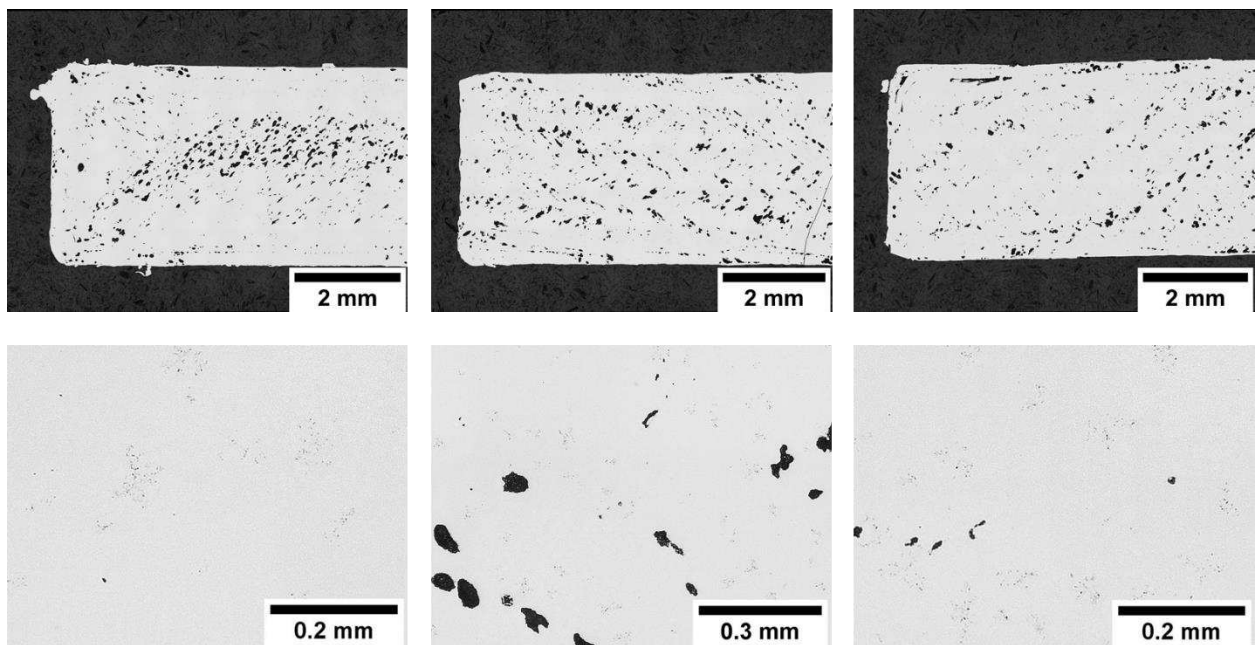


Fig. 72 From left to right: 5gB (bottom), 5gB (middle), 5gB (top)

The images above each show a block's horizontal cross section at three different planes and the respective magnified parts. It is difficult to assign the cavities to a certain printing path as they are round shaped and irregularly distributed. The zigzag printing path is

somehow visible in the middle images but not as clear as in previous samples. There are some areas that are affected more than others with no clear trend being deducible. At each cross section free C is displayed.

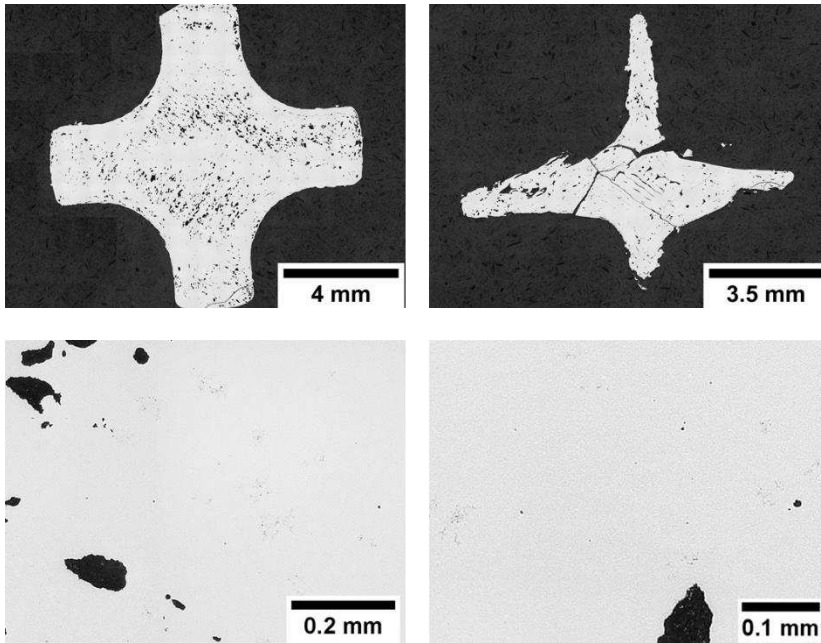


Fig. 73 From left to right: 5gDB (bottom), 5gDB (tip)

The images above each show a drill bit's horizontal cross section at two different planes and the respective magnified parts. While at the bottom cross section the cavities are round shaped, the zigzag path is still identifiable. Some areas (centre and region between the centre and the upper flank) are denser while the area enclosing the centre more affected by cavities. The centre of the tip cross section displays the cavities stemming from the zigzag printing strategy in the centre. Free C is visible at both cross sections.

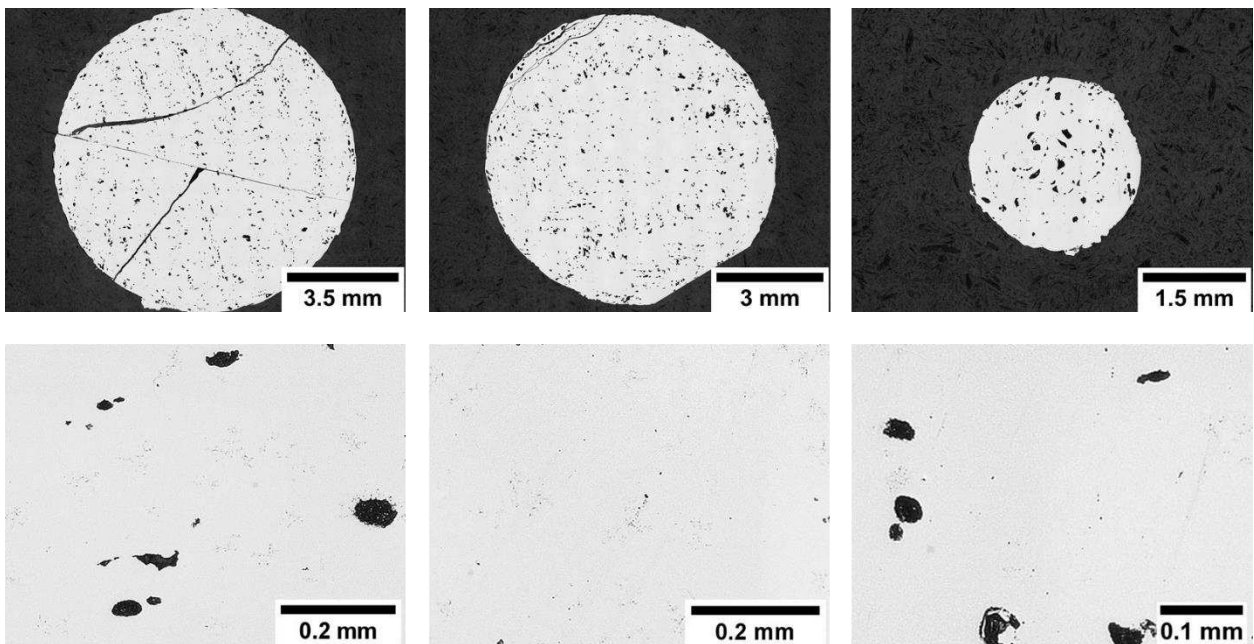


Fig. 74 From left to right: 5hC (bottom), 5hC (middle), 5hC (top)

The images above each show a cone's horizontal cross section at three different planes and the respective magnified parts. The cavities are round shaped. The original printing path is only recognizable in certain areas anymore, especially in the bottom cross section. Every cross section displays free C.

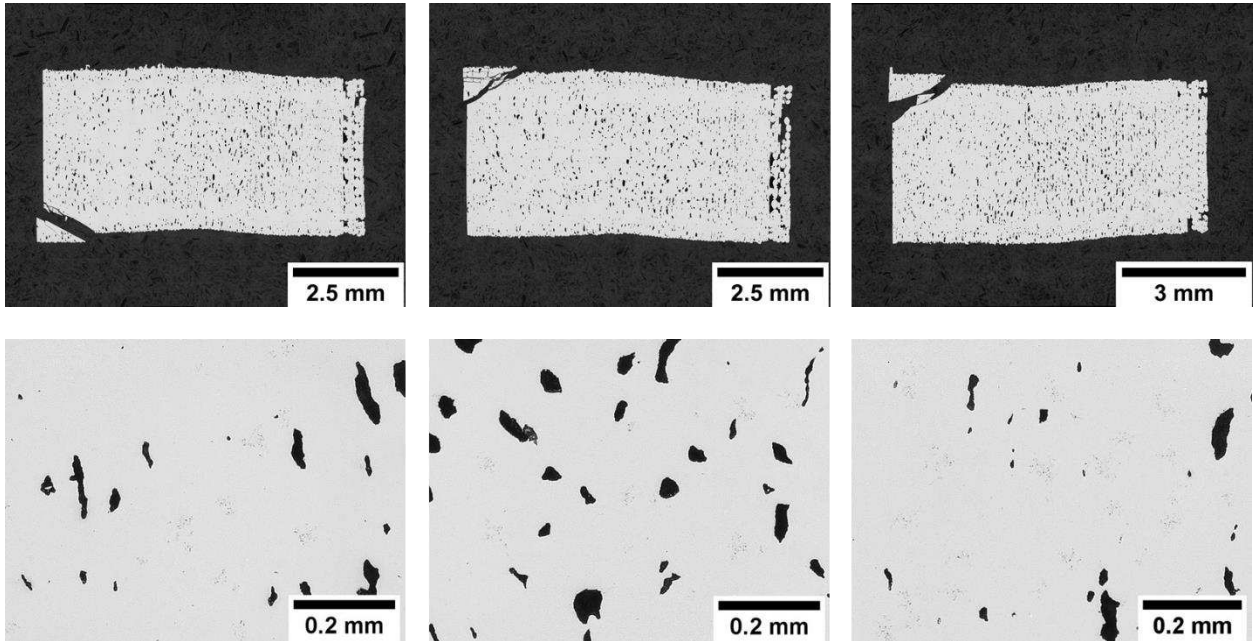


Fig. 75 From left to right: 5hB (left), 5hB (middle), 5hB (right)

The images above each show one half of a block's vertical cross section at three different planes rotated 90° to the right and the respective magnified parts. The cavities are round shaped and uniformly distributed throughout the sample, except a stronger affected area in the topmost layers. Like sample 5gC the area with the least cavities seems to be the interface area between border and centre. Free C is present at all three levels.

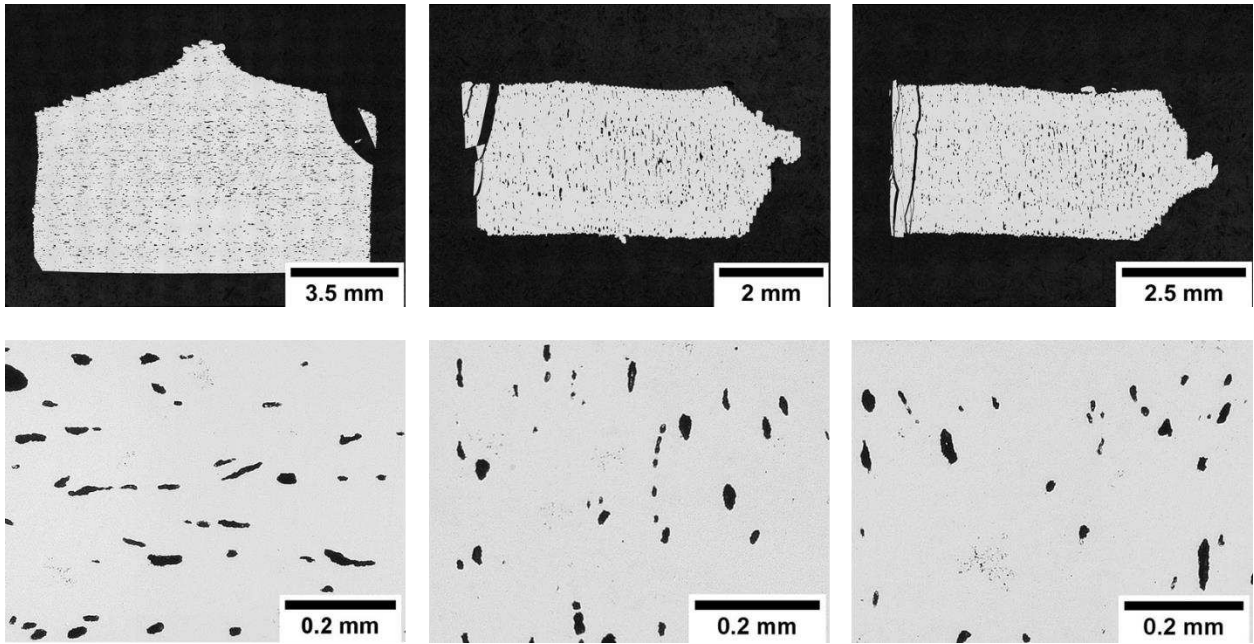


Fig. 76 From left to right: 5hDB, 5hDB (flank 1), 5hDB (flank 2)

The images above show a drill bit's vertical cross section as well as cross sections of two of the drill bit's flanks and the respective magnified parts. In all three images the cavities are round shaped resembling regular porosity and uniformly distributed. There are no distinguishable areas where lesser cavities are present. Free C is visible at each cross section.

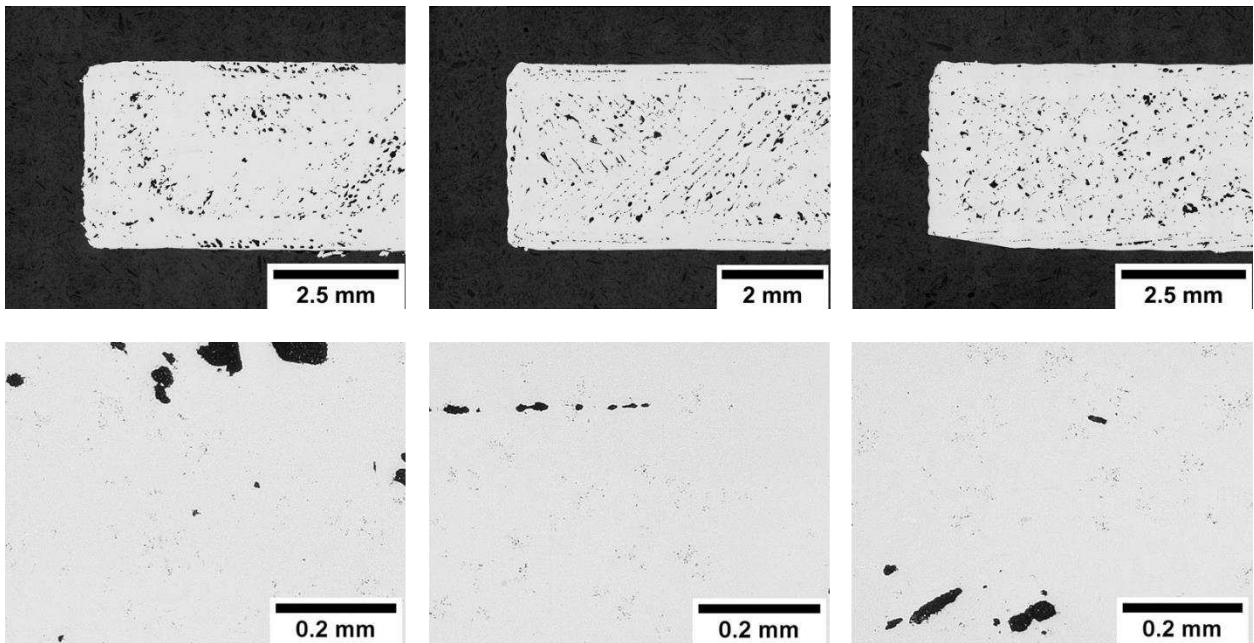


Fig. 77 From left to right: 5iB (bottom), 5iB (middle), 5iB (top)

The images above each show one half of a block's horizontal cross section at three different planes and the respective magnified parts. While the central zigzag printing strategy is only visible at a closer look at the left and the right cross section, it is clearly visible in the middle cross section where the typical poor row bonding took place. The

cavities in the border region are also observable in each of the three images. Free C is present throughout the whole sample.

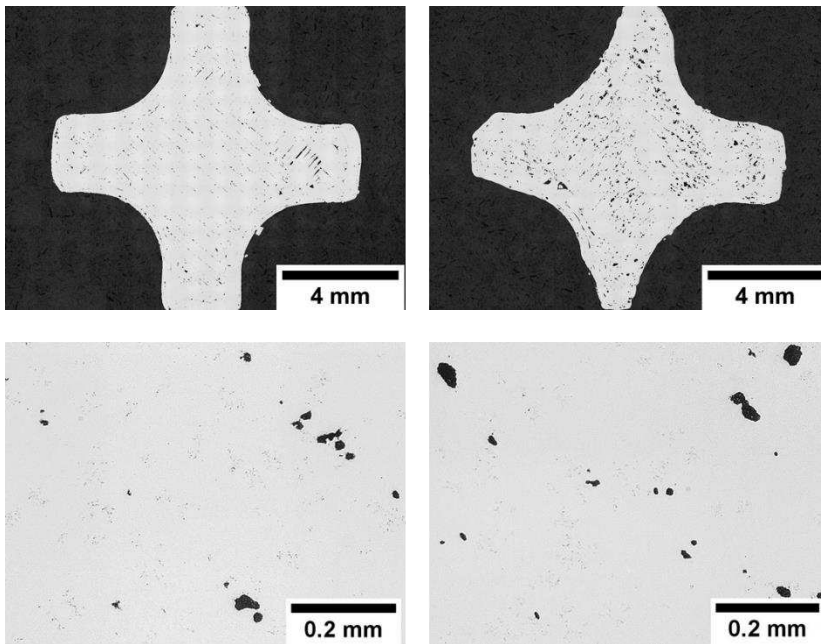


Fig. 78 From left to right: 5iDB (bottom), 5iDB (top)

The images above each show a drill bit's horizontal cross section at two different planes and the respective magnified parts. The cavities resulting from the zigzag printing are visible in both samples, although the number of cavities in general is higher in the top cross section. The sample above looks the most promising from the samples produced at a varied printing speed. Free C is visible in both cross sections.

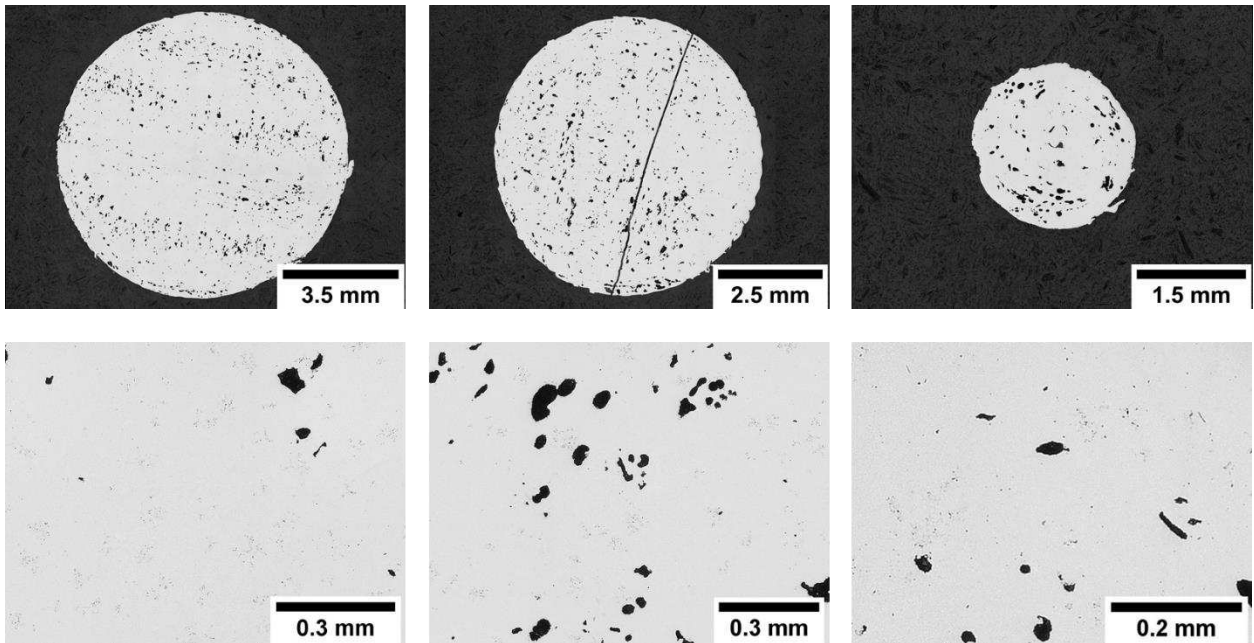


Fig. 79 From left to right: 5jC (bottom), 5jC (middle), 5jC (tip)

The images above each show a cone's horizontal cross section at three different planes and the respective magnified parts. The cavity situation worsens from bottom to top. The zigzag printing path is visible at a closer look, but the cavities are round shaped in general and resemble macropores. Free C is present in all three cross sections.

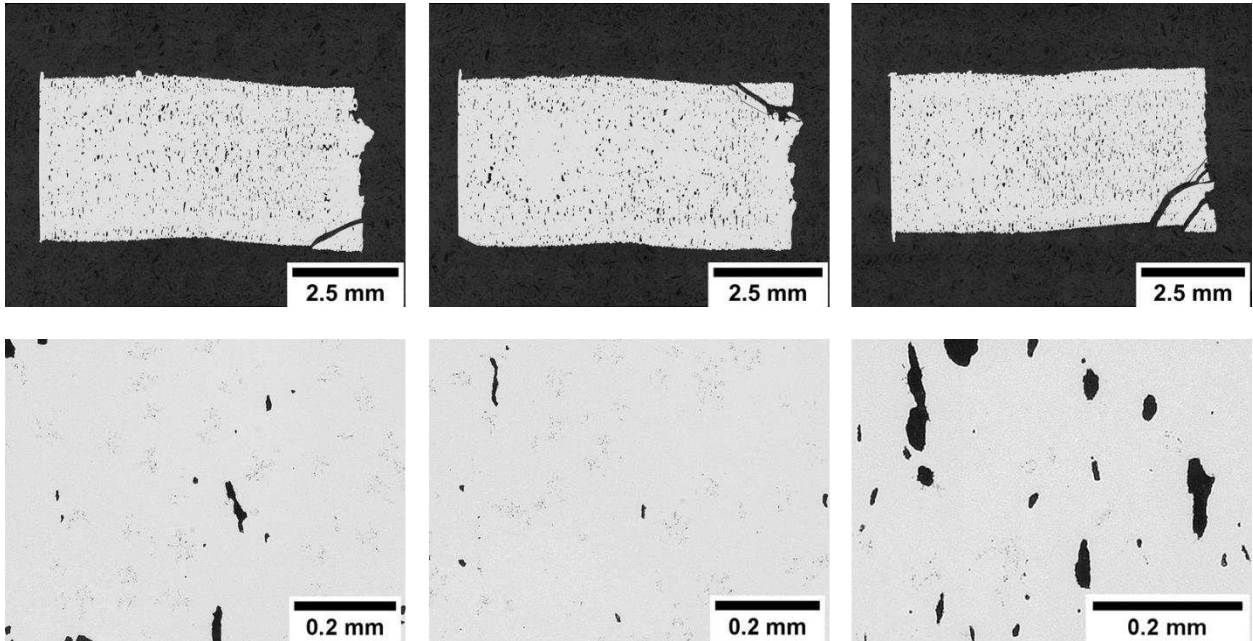


Fig. 80 From left to right: 5hB (left), 5hB (middle), 5hB (right)

The images above each show one half of a block's vertical cross section at three different planes rotated 90° to the right and the respective magnified parts. The cavities in all three cross sections are round shaped and uniformly distributed. There are some areas with lesser cavities especially in the interface region between border and centre. In all three cross sections free C is visible.

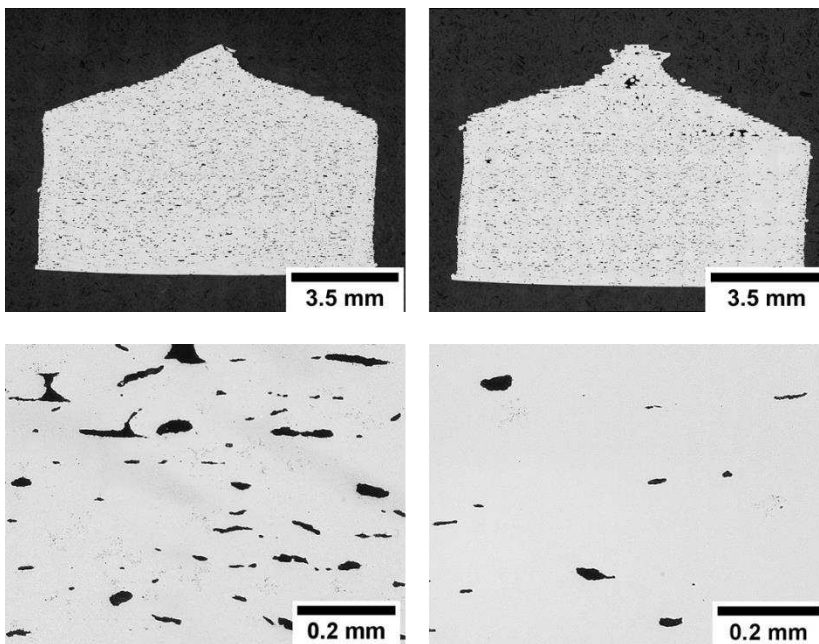


Fig. 81 From left to right: 5jDB, 5IDB

The images above each show a different drill bit's vertical cross section and the respective magnified parts. The left drill bit has round cavities without that do not like the typical ones known from previous series that stem from inadequate row bonding. The right one shows similar results, except two areas where the size and morphology of the cavities looks like the previous series' samples. Both samples display free C throughout the whole sample.

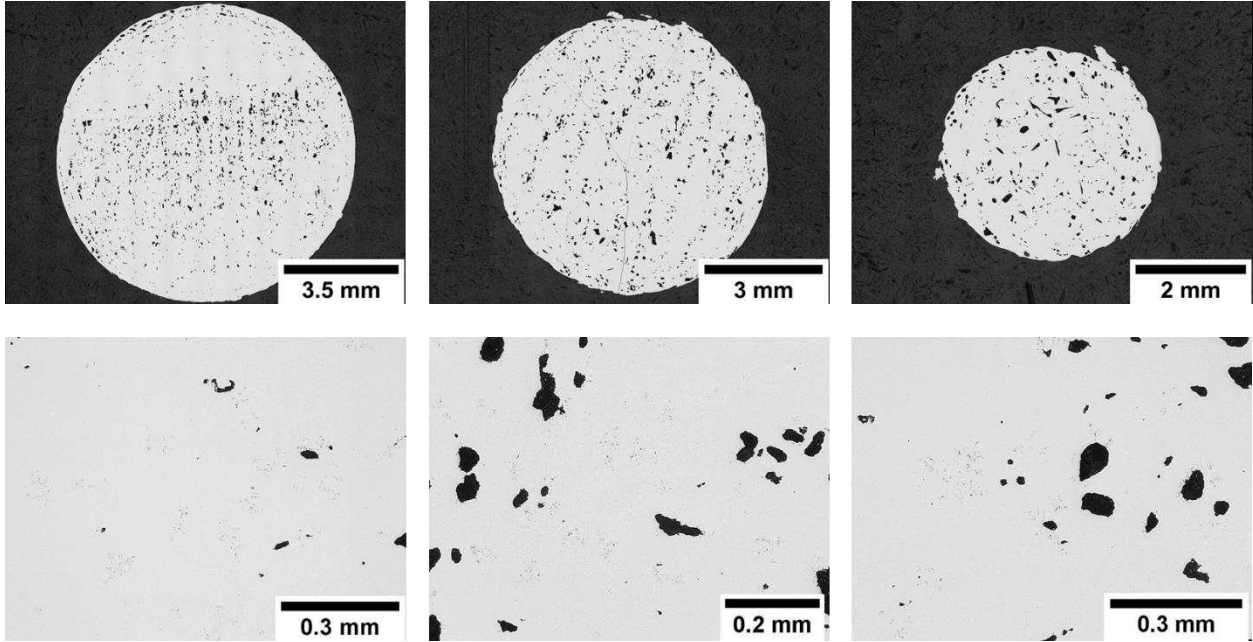


Fig. 82 From left to right: 5kC (bottom), 5kC (middle), 5kC (top)

The images above each show a cone's horizontal cross section at three different planes and the respective magnified parts. In all three cross sections the cavities are round shaped, and the original zig zap printing path is only recognisable at a closer look. Free C is visible at each cross section.

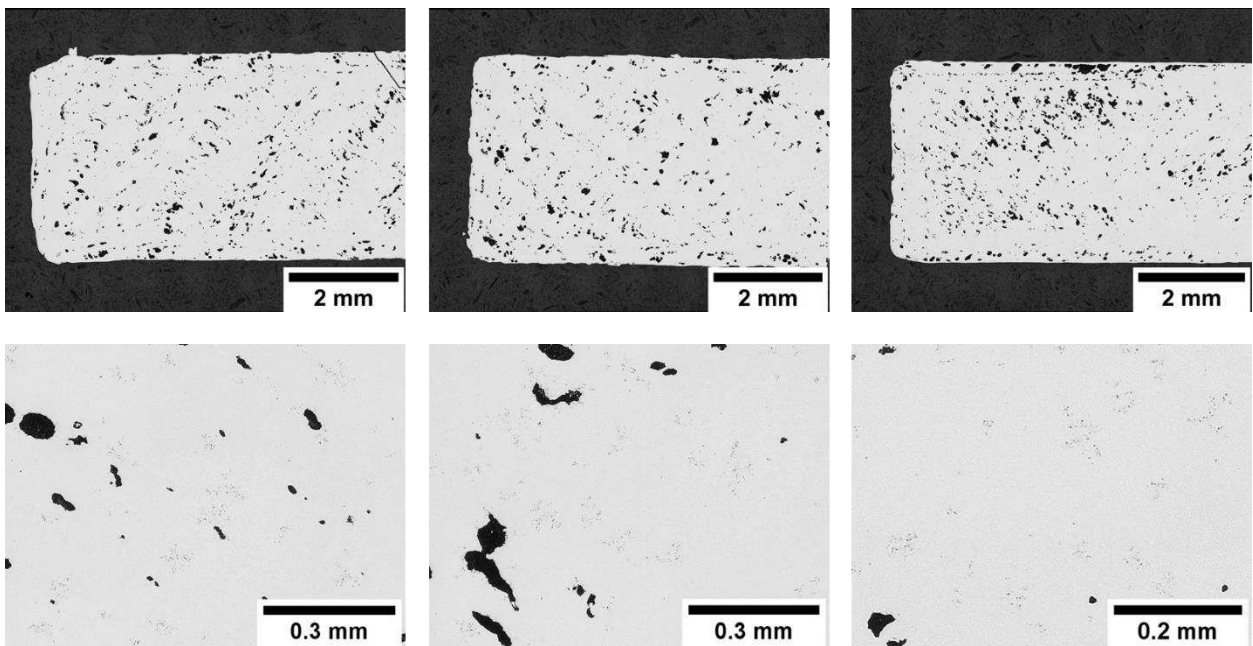


Fig. 83 From left to right: 5kB (bottom), 5kB (middle), 5kB (top)

The images above each show a block's horizontal cross section at three different planes and the respective magnified parts. The zigzag printing strategy is recognisable as the round shaped cavities follow a certain path but the rows themselves are not distinguishable anymore. Free C is present in every cross section.

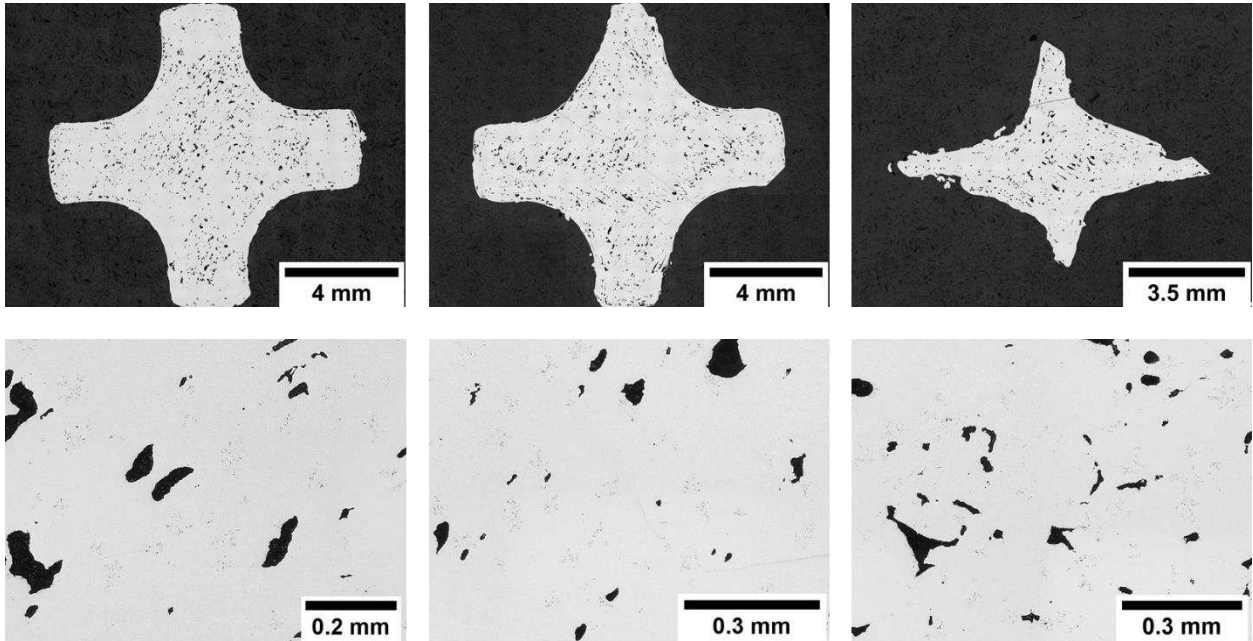


Fig. 84 From left to right: 5kDB (bottom), 5kDB (middle), 5kDB (top)

The images above each show a drill bit's horizontal cross section at three different planes and the respective magnified parts. Corresponding to the previous sample the round shaped follow the zigzag path even though the single rows are not distinguishable anymore, except for a small area at the centre of the top cross section. Cavities at the border indicate inadequate row bonding while printing the rim. Free C can be seen at each cross section.

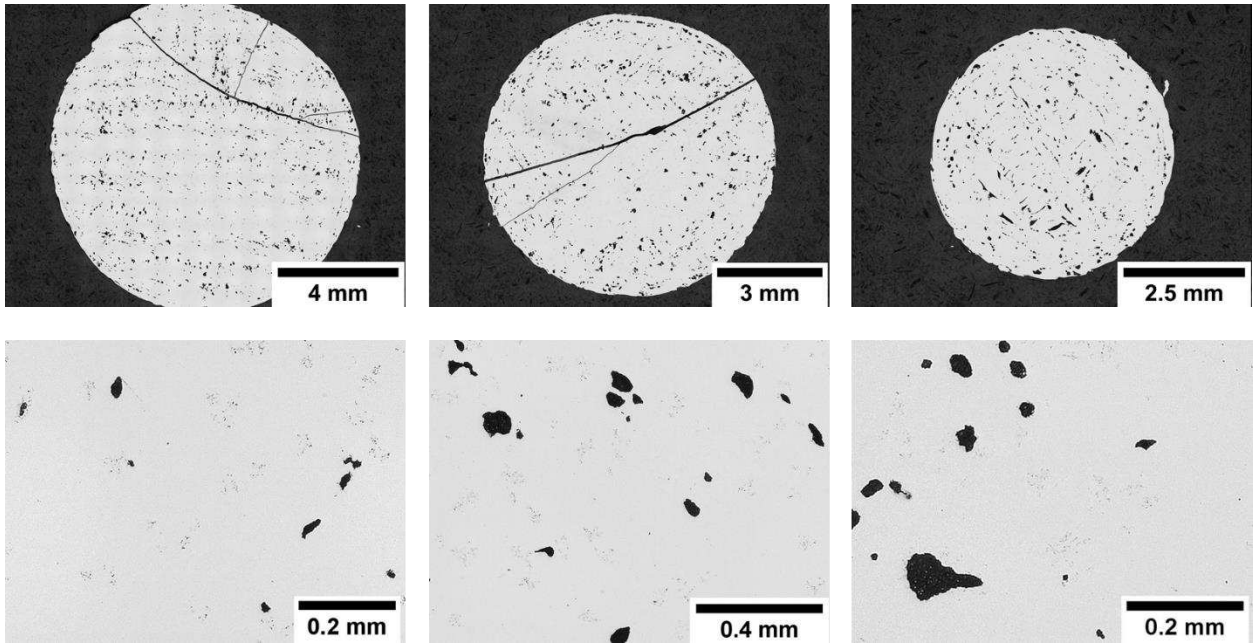


Fig. 85 From left to right: 5IC (bottom), 5IC (middle), 5IC (top)

The images above each show a cone's horizontal cross section at three different planes and the respective magnified parts. While at the top cross section the cavities stemming from the zigzag printing are especially prominent, they are only indicated in the middle and the bottom cross section by the path the round shaped cavities follow. The poor bonding between the border rows is also recognizable by the shape and path of some cavities. All cross sections exhibit free C.

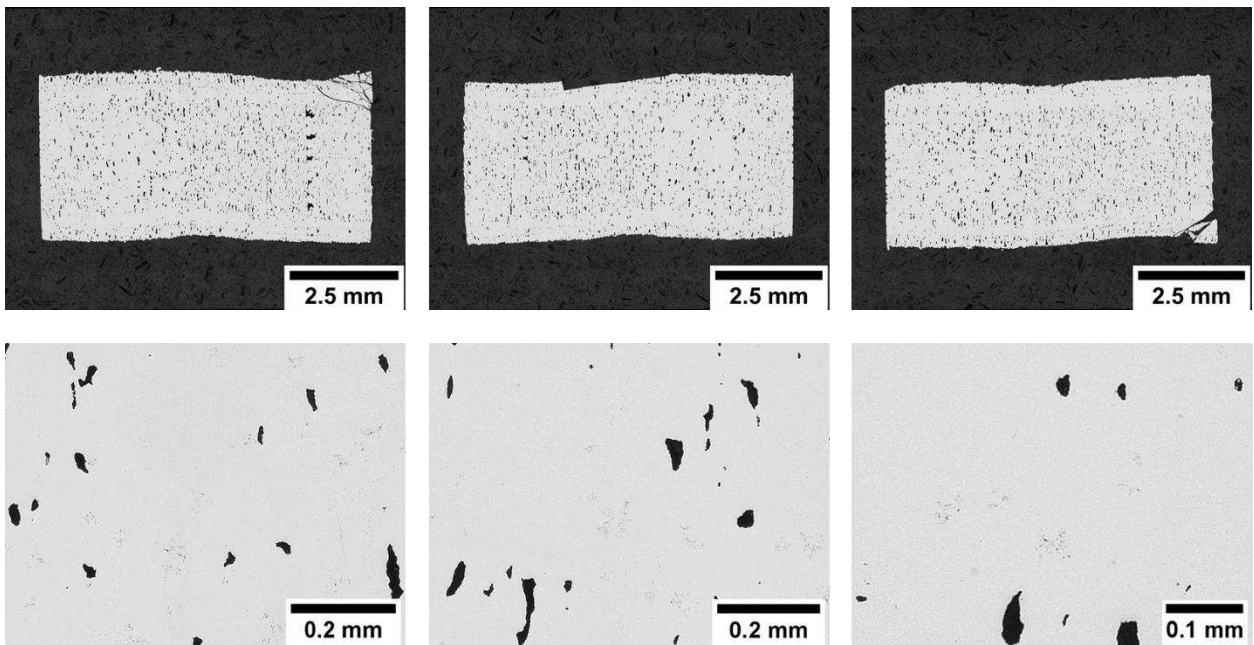


Fig. 86 From left to right: 51B (left), 51B (middle), 51B (right)

The images above each show one half of a block's vertical cross section at three different planes rotated 90° to the right and the respective magnified parts. The cavities are uniformly distributed, except for an area in the left cross section where larger cavities are

visible. The region with the least cavities is the interface region. Free C is visible throughout the whole sample.

4.7.5 Summary of the 5th series

In the 5th series the printing parameters were changed mainly regarding the flow rate and the printing speed, which were varied during the printing process compared to previous series where it was kept constant. When varying the flow rate, the cavities did not change their shape but in some cases (5eB, 5eDB, 5f) the situation in general improved greatly. The samples in whose printing process the printing speed was varied, displayed cavities whose shape changed and the large cavities which were entire lines of unbonded material transformed to many single round shaped cavities which only indicated the original printing path. The fact that some samples had almost completely dense areas, although they were produced with the same set of parameters as other samples, which did have higher levels of cavitation, questions the general reproducibility while using this printer setup. The mass loss corresponded to previous series and the magnetic properties as well. A thermal debinding process with a mixed atmosphere did not have any impact, as the temperatures at which H₂ was applied were too low.

4.8 Self-printed series

In this chapter the self-printed series' results will be presented and discussed.

4.8.1 Printing parameters of the self-printed series

The printing parameters are listed in Tab. 10.

Tab. 10 Printing parameters of the self-printed series

	Row width (mm)	T _{Nozzle} (°C)	T _{Bed} (°C)	Print speed (mm/s)	Flow rate (%)	Nozzle diam. (mm)
Set 1	0.1	250	95	10	100	0.4
Set 2	0.1	250	95	10	100	0.2
Set 3	0.1	250	95	10	105	0.2
Set 4	0.1	250	95	10	110	0.2

4.8.2 Mass loss of the self-printed series

In this subchapter the mass loss is presented and discussed from thermal debinding to the fully sintered samples. Fig. 87 shows the results for each sample of this series.

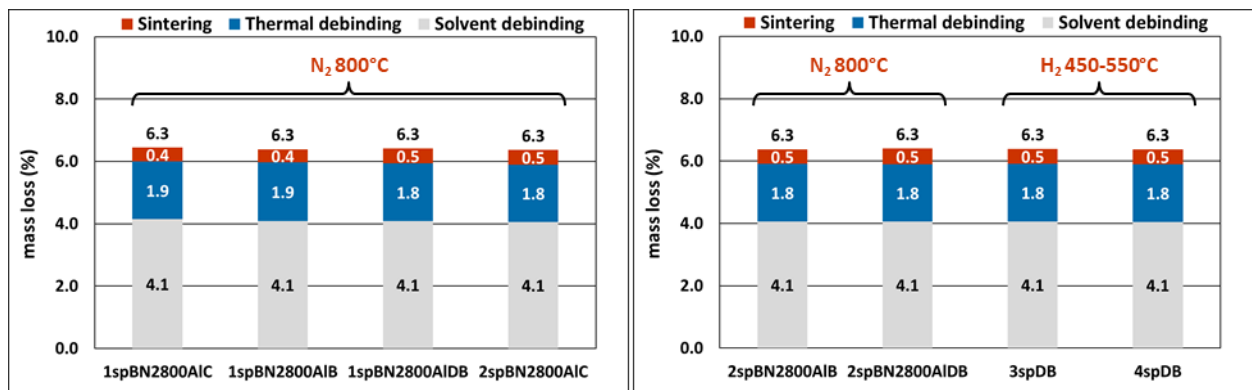


Fig. 87 Mass loss of the self-printed series

The mass loss for solvent debinding corresponds to the 1st series and is slightly lower compared to the later series done by MU Leoben. Even though the 1st and the 2nd self-printed series were produced using the Ceratizit filament, they do not differ from the last two self-printed samples out of Hyperion filament. The mass loss during thermal debinding and consequently the total mass loss is very similar throughout all the self-printed samples even though the thermal debinding parameters slightly changed, as the

last two samples were debinded under N_2 up to $600^\circ C$, except between 450 and $550^\circ C$ where H_2 was applied. The 1st and the 2nd series on the other hand were thermally debinded under pure N_2 up to $800^\circ C$. The

4.8.3 Magnetic properties of the self-printed series

In this subchapter the magnetic properties are presented and discussed. Fig. 88 shows the results for each sample of this series.

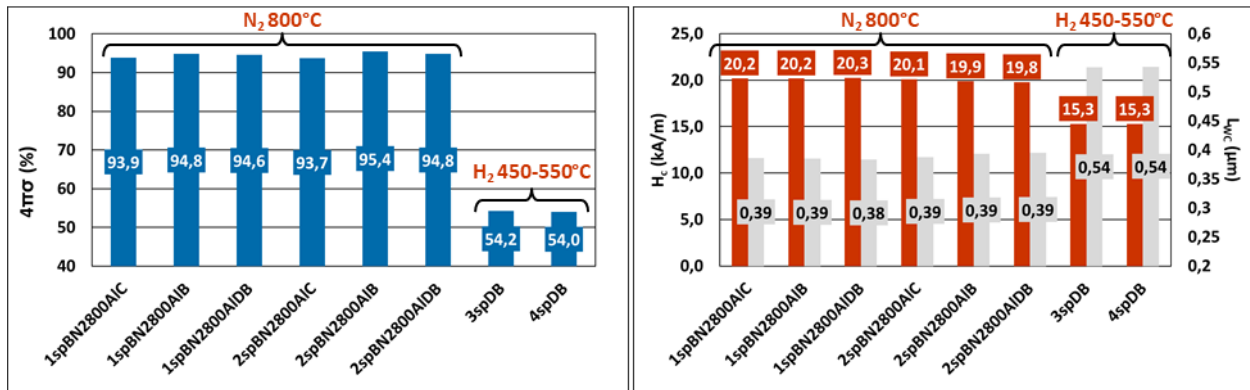


Fig. 88 Left: magnetic saturation of the self-printed series, right: coercive force and L_{WC} of the self-printed series

The magnetic saturation results correspond to the previous series. Debinding under pure N_2 only lowers the C balance enough to roughly reach the threshold of 95%, that is not changed by the fact that another filament was used, meaning the volume fractions of the organic binder in the two filaments is about the same. Debinding under N_2 up to $600^\circ C$ and switching to H_2 from 450 to $550^\circ C$ seemingly removed lots of C and shifted the samples deep into the η region, however those values result from incomplete sintering due to an error in the process. The samples were cooled very rapidly almost quenched so to speak, as it came to a shut down of the generator providing the induction furnace with power. The phase equilibria and the dissolved elements were frozen as they are at maximum temperature as no diffusion could take place anymore because of the rapid cooling. This resulted in very low magnetic saturation values, as the magnetic saturation represents the level of dissolved elements in the binder phase and at high temperatures the solubility is significantly higher than at low temperatures. As will be shown in the next chapter the cross sections of the respective samples appear to be two-phased, although it can not be guaranteed that a normal cooling would yield the same results as dissolved elements, even C, might reprecipitate in form of different phases such as free C or η phase.

The coercive force results correspond to the results of the 1st series where Ceratizit filament was also investigated. The starting powder has a finer starting grain size which leads to higher coercive force values. However, the values above are still lower than the ones yielded in the 1st series which were debinded under H_2 confirming the trend, that N_2 leads to coarse hard phase grains than H_2 . The last two samples are not to be considered as incompletely sintered samples can not be compared to fully sintered samples regarding the grain size.

4.8.4 LOM results of the self-printed series

In this subchapter the LOM images are presented and discussed. Fig. 89 to Fig. 93 show the images for each sample of this series.

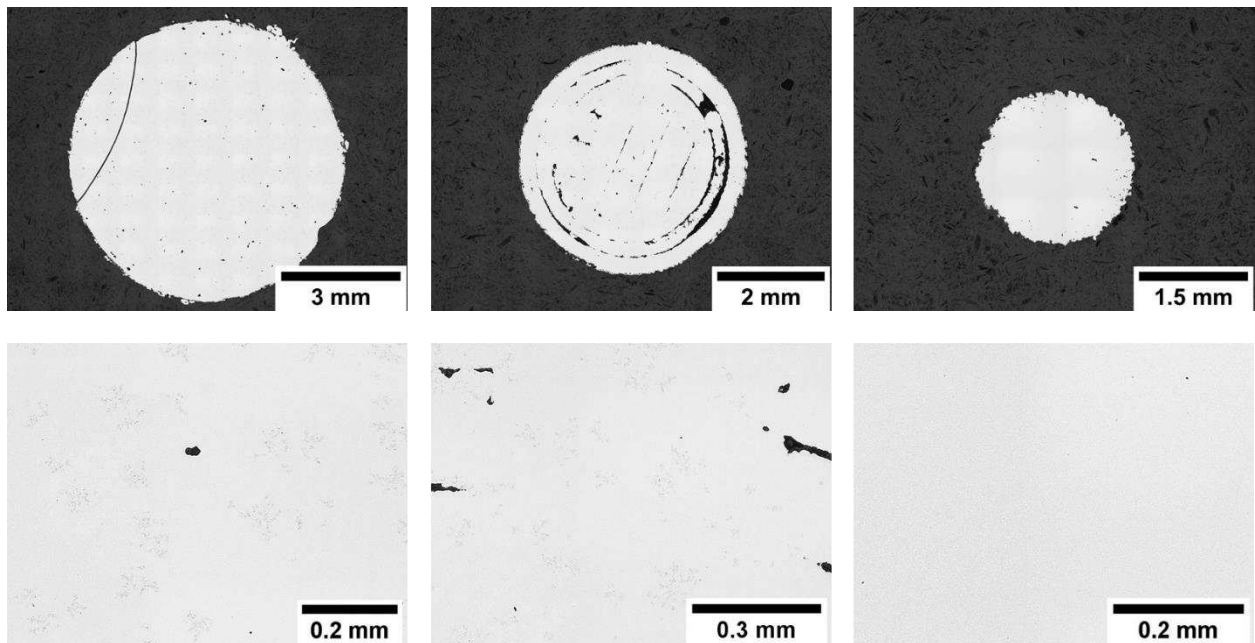


Fig. 89 From left to right: 1spBN2800AIC (bottom), 1spBN2800AIC (middle), 1spBN2800AIC (tip)

The images above each show a cone's horizontal cross section at three different planes and the respective magnified parts. The bottom and the top cross section are almost free of cavities. The residual pores could also be regular macropores resulting from the vacuum sintering process. The middle cross section displays the typical cavities resulting from poor row bonding in the border region as well as cavities indicating the zigzag printing strategy. Free C is present in the bottom and the middle cross section. The right cross section represents the topmost part of the sample. It is seemingly C free.

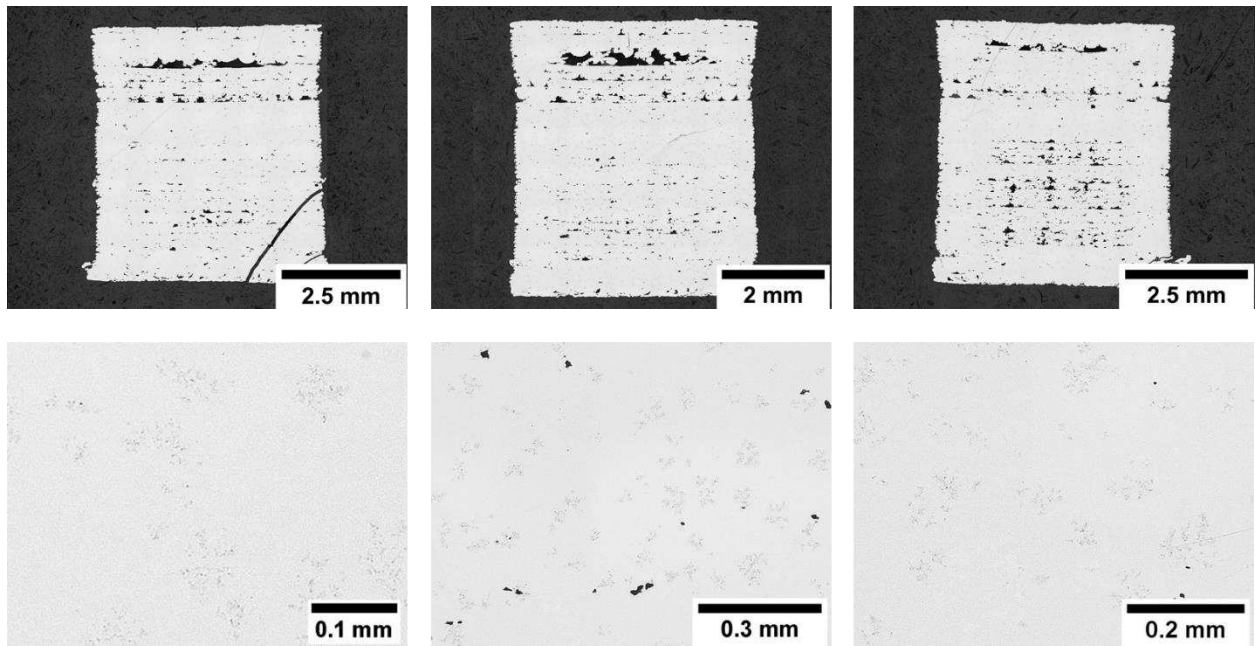


Fig. 90 From left to right: 1spBN2800AIB (bottom), 1spBN2800AIB (middle), 1spBN2800AIB (tip)

The images above each show a block's vertical cross section at three different planes and the respective magnified parts. Despite some areas close above the centre and at the bottom which have fewer cavities, the sample displays areas of large cavities especially in the top third and the centre reaching downwards. Free C is visible at all cross sections.

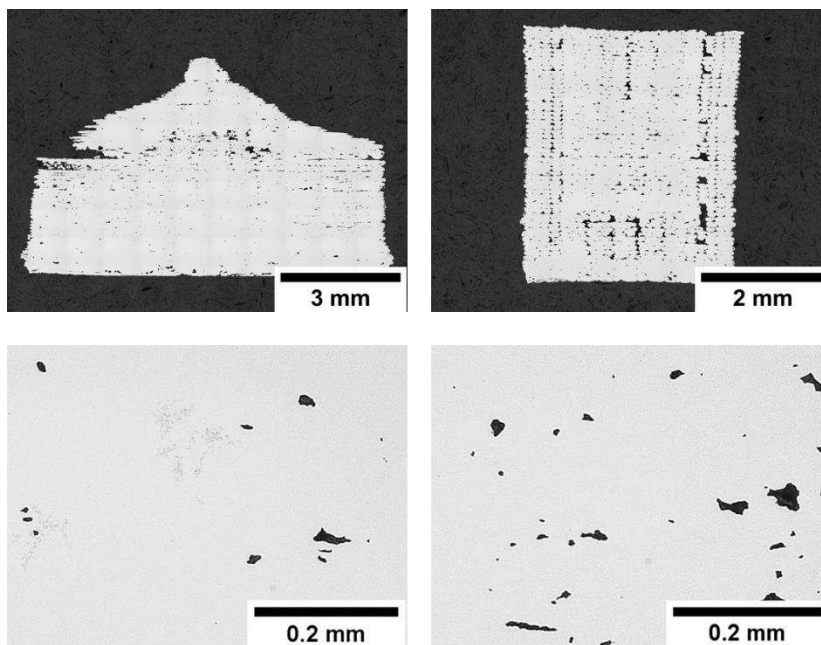


Fig. 91 From left to right: 1spBN2800AIDB, 2spBN2800AIB

The left images show a cone's vertical cross section and the respective magnified part. In the bottom and centre regions, the sample shows very few cavities. The top region is

also hardly affected but between the centre and the top region there is a small area where larger cavities are present. The sample exhibits free C.

The right images show a block's vertical cross section and the respective magnified parts. The cavities stemming from the poor row bonding in the interface region between border and centre are visible going upwards bottom to top. The rest of the sample is also affected by large cavities especially in the bottom quarter. The bottom is the least affected area. Even though the sample was thermally debinded with the other samples it shows no additional phases and its cavity configuration might have led to the drop below the threshold of free C.

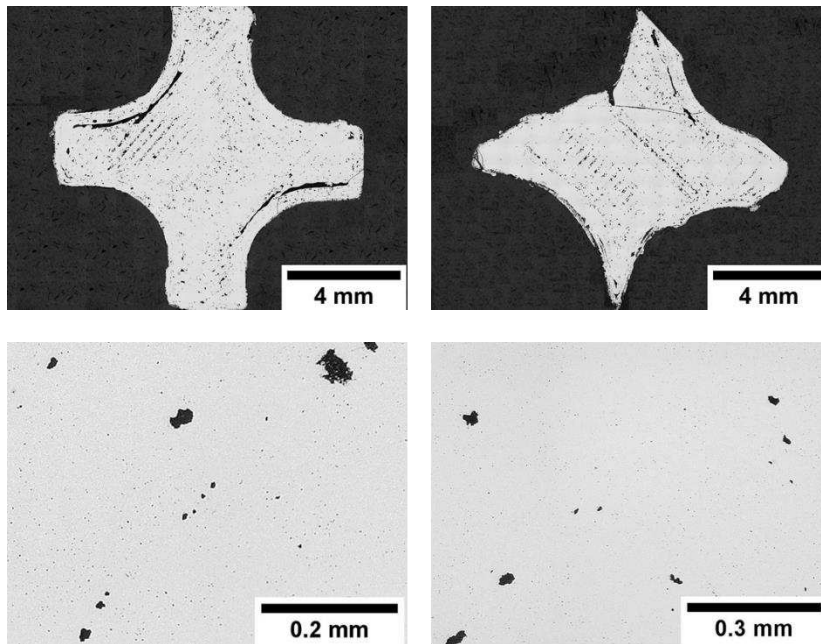


Fig. 92 From left to right: 3spDB (bottom), 3spDB (top)

The images above each show a drill bit's horizontal cross section at two different planes and the respective magnified parts. The cross sections each show large cavities in the interface region between border and centre. Furthermore, the zigzag printing path is indicated by single round shaped cavities in the centre. The sample seems to be two-phased. This is one of the samples whose sintering cycle was interrupted so the sample exhibits a lot of microporosity. Due to the interruption the C balance phase status should also be questioned compared to a regularly sintered sample, as regular cooling might have led to reprecipitation.

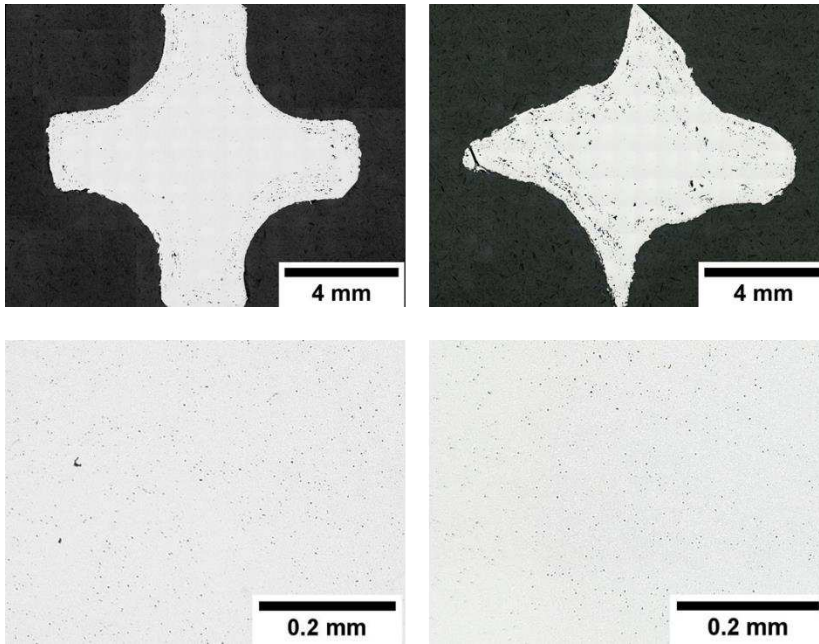


Fig. 93 From left to right: 4spDB (bottom), 4spDB (top)

The images above each show a drill bit's horizontal cross section at two different planes and the respective magnified parts. The sample above shows one of the most promising results throughout the thesis as especially at the bottom cross section the sample seems to be almost free of cavities except some small cavities in the border region. The level of cavitation worsened a bit in the top cross section but is still better than most samples in the top region. Just as the sample before the sample is two-phased. Microporosity is present throughout the whole sample.

4.8.5 Surface quality of the self-printed series

Just as in the 1st series there was a significant difference in surface quality when using the Ceratizit filament and the Hyperion filament as shown in Fig. 94.

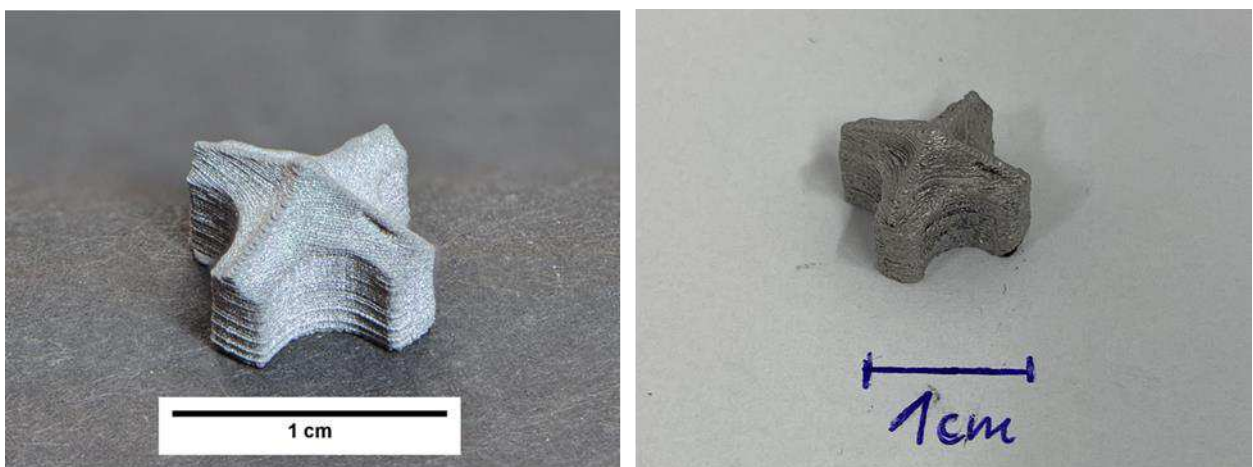


Fig. 94 Left: drill bit produced from Ceratizit filament, right: drill bit produced from Hyperion filament

Ceratizit filament leads to smooth surfaces without any blobs or filament curling. The handling during printing regarding adhesion and clogging was also more comfortable than with Hyperion filament, which led to surface irregularities especially visible between the front flanks in the right image. The reason is most likely again the different RTP wax, as the other components do not affect the printing behaviour or are the same for both feedstocks.

4.8.6 Summary of the self-printed series

Starting from the printing parameters MU Leoben used in the 5th series as a reference, own sets of printing parameters in which only the flow rate was changed were investigated, as faster printing speeds did not remove but only change the cavity morphology in the 5th series and the experiments with faster printing speeds led to delamination during printing and whole areas being empty due to improper row bonding. The experiments were carried out with Ceratizit filament at first, as the green bodies displayed far better surface quality and the filament had a better extrusion behaviour. In some samples certain areas were produced cavity free, while others showed large cavity agglomerations. Especially the last sample can act as a foundation for further research, as it shows that producing cavity-free green bodies by FFF is certainly possible, but the printing parameters have to be tailored exactly to one desired geometry. The mass loss and the magnetic saturation corresponded with previous samples and the magnetic saturation aligned with the metallographic specimen. Unfortunately, the sintering of the last two samples was interrupted, questioning the two-phased microstructure.

4.9 Isostatically pressed samples

In this chapter the isostatic pressing experiment's results will be presented and discussed.

4.9.1 Printing parameters of the isostatically pressed samples

The printing parameters are listed in Tab. 11.

Tab. 11 Printing parameters of the isostatically pressed samples

	Row width (mm)	T _{Nozzle} (°C)	T _{Bed} (°C)	Print speed (mm/s)	Flow rate (%)	Nozzle diam. (mm)
CIP 1	0.1	250	95	11	113	0.4
CIP 2	0.1	250	95	16	111	0.4
HIP	0.1	250	95	9	layer 0 to 10: 100 layer 11 to end: 115	0.2

4.9.2 Mass loss and shrinkage of the isostatically pressed samples

In this subchapter the mass loss is presented and discussed from thermal debinding to the fully sintered samples. Fig. 95 shows the results for each sample of this series.

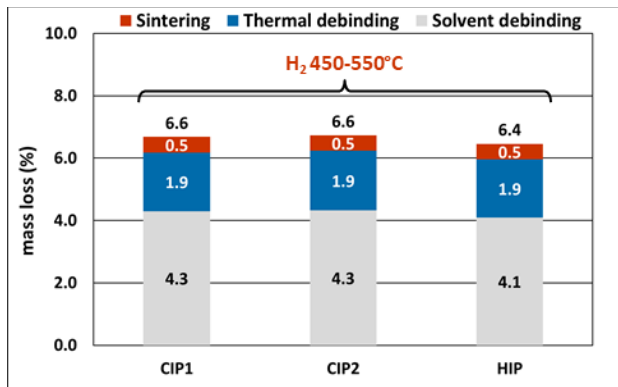


Fig. 95 Mass loss of the isostatic pressing experiments

The mass loss corresponds to the previous series and thermal debinding programs applied in the self-printed series.

4.6.3 Magnetic properties of the isostatically pressed samples

In this subchapter the magnetic properties are presented and discussed. Fig. 96 shows the results for each sample of this series.

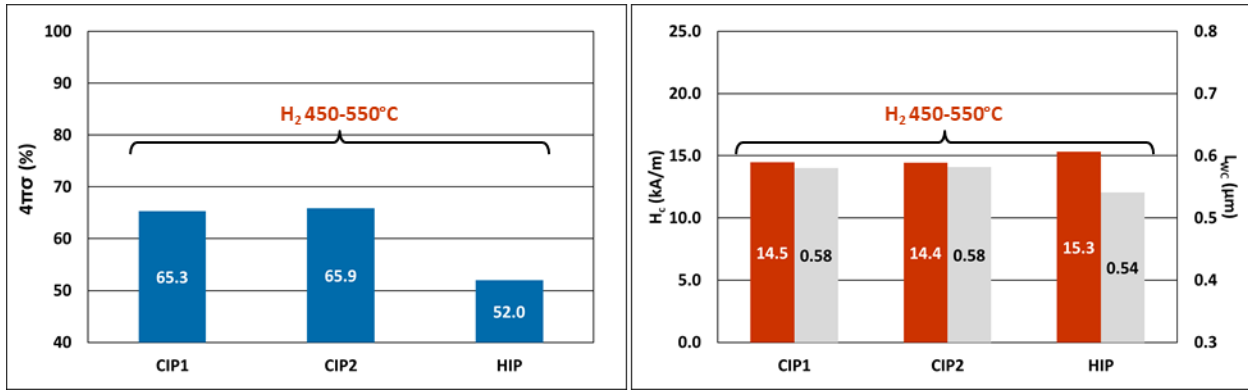


Fig. 96 Left: magnetic saturation of the isostatic pressing experiments, right: coercive force and L_{WC} of the isostatic pressing experiments

The magnetic saturation results must be differentiated. The HIP sample was debinded together with 3spDB and 4spDB from the self-printed series and thus was part of the interrupted sintering cycle. The CIP samples are fully sintered and represent the actual magnetic saturation values resulting from this thermal debinding program. As expected, the reprecipitation of C and other elements (mostly W) led to a rise in the magnetic saturation but unfortunately not enough to reach the two-phase region. That means that debinding under N_2 up to $600^\circ C$, while switching to H_2 between 450 and $550^\circ C$ lowers the C balance into the η region. Debinding under N_2 up to $600^\circ C$, while switching to H_2 between 200 and $300^\circ C$ on the other hand is not enough to lower the C balance to reach the two-phase region and produces free C containing samples, as seen while discussing the 5th series in *4.7.3 Magnetic properties of the 5th series*. The right thermal debinding program may lie between the chosen temperatures, but as seen before, even the application of pure H_2 and pure N_2 led to two-phased samples which a mixture could not until now. The debinding program is too dependent on the level of cavitation and unless a dense sample is produced, the one and only thermal debinding program will hardly be established, making the process of reaching a two-phased sample affected by cavities kind of a lottery.

4.9.4 LOM results the isostatically pressed samples

In this subchapter the LOM images are presented and discussed. Fig. 97 to Fig. 99 show the images for each sample of this series.

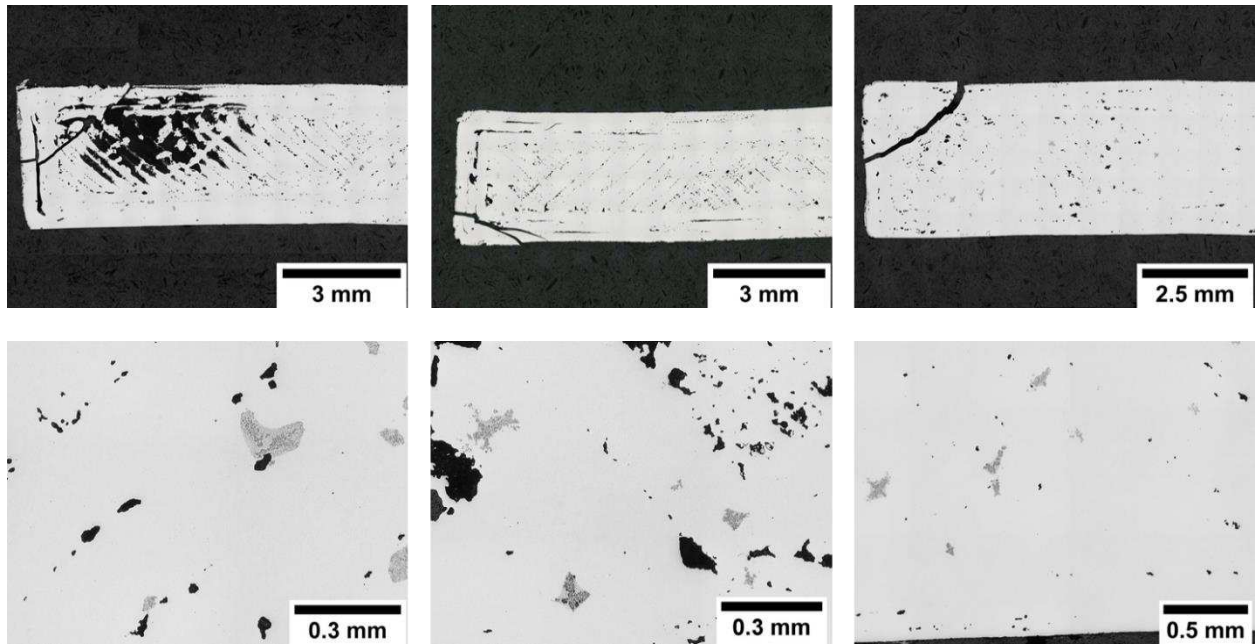


Fig. 97 From left to right: CIP1 (bottom), CIP1 (middle), CIP1 (top)

The images above each show a cone's horizontal cross section at three different planes and the respective magnified parts. Especially in the central and the right images the interface region cavities are observable. The circular border printing strategy as well as the zigzag printing strategy in the centre led to inadequate bonding such as in many samples of the previous series. The top of the sample seems to be less affected by cavities than the bottom and the middle. The whole sample displays free C.

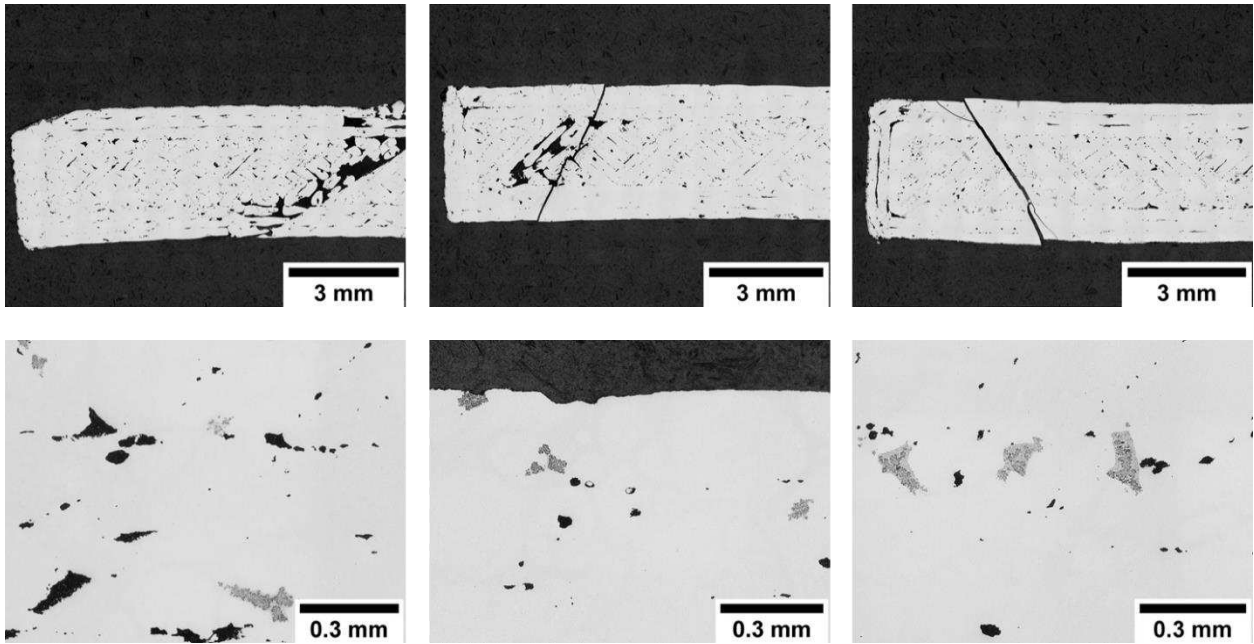


Fig. 98 From left to right: CIP2 (left), CIP2 (middle), CIP2 (right)

The images above each show one half of a block's vertical cross section at three different planes rotated 90° to the left and the respective magnified parts. Except for a small region in the centre of the middle cross section and one on the upper left edge of the bottom cross section, no particularly large cavities are visible. The residual cavities throughout the sample are smaller and round shaped resembling traditional pores but still indicate the original printing path. Corresponding to the magnetic saturation results the sample exhibits free C.

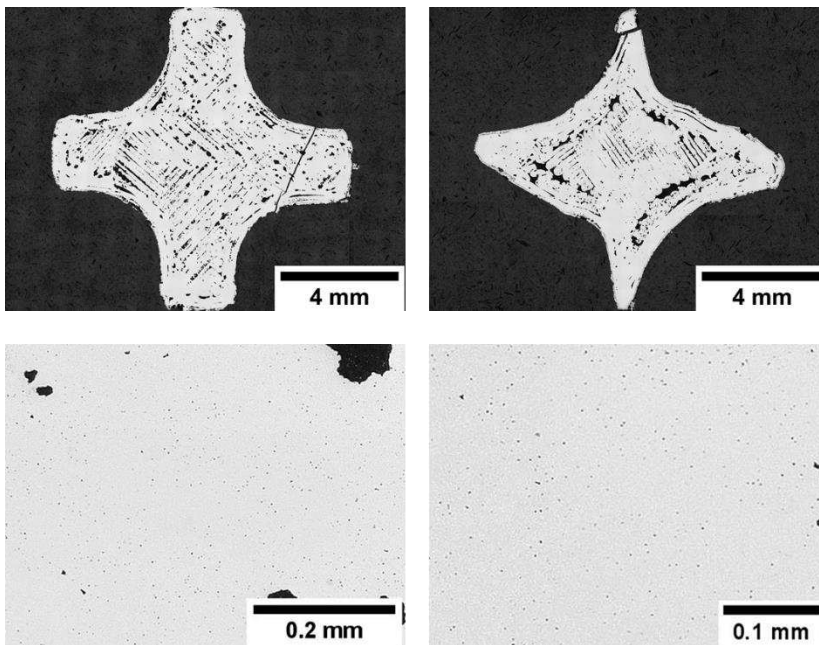


Fig. 99 From left to right: HIP (bottom), HIP (top)

The images above each show a drill bit's horizontal cross section at two different planes and the respective magnified parts. All three characteristic kinds of cavities (border,

interface, and centre) resulting from improper row bonding are clearly visible at both cross sections. The magnified areas show the micropores resulting from the interrupted sintering cycle, as already seen at samples 3spDB and 4spDB. The samples appear to be two-phased while most likely being in the η region as suggested by the hypothesis presented in the previous subchapter.

4.9.5 Summary of the self-printed series

As this chapter shows, the post-densification process, either CIP or HIP, did not lead to a successful elimination of the cavities, meaning that the cavities are connected throughout the sample which would be referred to as open porosity, rendering every isostatic pressure procedure useless. The mass loss confirmed previous results. The magnetic saturation corrected the previous statement that samples 3spDB and 4spDB were two-phased, as the fully sintered samples, which were thermally debinded with the same parameters showed, that applying H_2 between 450 and 550°C is enough to shift the C balance into the η region.

5 Conclusion and Outlook

During this thesis' research the FFF printability of commercial RTP hardmetal powder was investigated. After the production, the testing of the filaments and the printing, the printed parts were sent to our research group to TU Wien to debind, sinter and analyse the printed samples. Additionally, the pure RTP powder was pressed and tested regarding the debinding and sintering behaviour. MU Leoben produced five series in total, whose printing parameters were varied mainly in the printing speed and the flow rate. Our research group produced several samples based on the parameters and the work previously done by MU Leoben.

The 1st series showed that H₂ at 600 as well as 800°C is enough to shift the printed samples series into the η region. N₂ as a debinding atmosphere at the applied temperatures did not lower the C balance enough to gain two-phased samples. The printed samples had different degrees of cavity amount and size and the bonding in the interface region between border and centre would already pose a problem in this series which would not be eliminated even in the most recent series. It was shown that the mass loss during solvent debinding is around 4.2% and around 2% for the thermal debinding, which is not related to the pressed samples mass loss during thermal debinding, as the wax, which made up the 2% in *4.2.1 Mass loss and shrinkage of the pressed samples* is already removed during solvent debinding.

In the 2nd series, a different set of printing parameters, which changed in a reduced flow rate did improve the density in some cases and in other cases worsened the cavity situation. It was shown for the first time that the same thermal debinding conditions could impact samples of different geometries in different intensity regarding their C balance, if the printing led to larger cavities and thus a larger inner surface and a higher reactivity. This was also the only series where an influence of the support plate material was undoubtedly recognizable, as in limited areas the C balance rose by putting a C source underneath the sample. Comparing the 2nd series with the 1st series, it was also shown that different printing parameters lead to different feedstock infills and thus the mass loss changed because of different levels of organic binder, even if the dimensions of the printed samples do not change significantly.

In the 3rd series a lower flow rate was used during printing which led to large cavities due to poor row bonding. This resulted in a higher C loss at the same thermal debinding parameters already used before. While the H₂ debinded samples showed the presence of η phase, the N₂ debinded samples were two-phased opposed to the previous samples, even though the thermal debinding program was not changed. This underlines the different impact of the same conditions on samples of different cavity levels, sizes, and orientations.

The 4th series was produced using a slower printing speed which resulted in generally denser bodies. The mass loss during thermal debinding under N₂ up to 800°C was slightly higher than the one in the 1st and 2nd series but the one under H₂ up to 600°C was similar to the previous results. While the H₂ atmosphere lowered the samples into the η region, the debinding under N₂ was not enough to lower the sample into the two-phase region which is especially interesting as N₂ and heating up to only 600°C was enough for the 3rd series to drop into the two-phase region, while heating up to higher temperatures did not result in two-phased samples in this series, which underlines once more the impact of the

cavitation level, as milder thermal debinding conditions led to a larger C loss in the 3rd series' samples

In the 5th series the printing parameters were changed mainly regarding the flow rate and the printing speed, which were varied during the printing process compared to previous series where it was kept constant. Varying the flow rate led to some of the best results, especially in some limited areas (bottom region of 5f samples). However, the fact that some samples had almost completely dense areas, although they were produced with the same set of parameters as other samples, which did have higher levels of cavitation, questions the general reproducibility while using this printer setup. The variation of the printing speed changed the cavities' morphology as they were now round shaped but did not eliminate them, in fact the overall quality was better with the samples where the printing speed was varied.

Starting from the printing parameters MU Leoben used in the 5th series as a reference, own sets of printing parameters in which only the flow rate was changed as faster printing speeds did not lead to promising results in the 5th series. The experiments were carried out with Ceratizit filament at first, as the green bodies displayed far better surface quality and the filament had a better extrusion behaviour. In some samples certain areas were produced cavity free, while others showed large cavity agglomerations. Especially the 4spDB can act as a foundation for further research, as it shows that producing cavity-free green bodies by FFF is certainly possible, but the printing parameters must be tailored exactly to one desired geometry. The metallographic specimens were two-phased further improving the obtained results, if it were not for the interrupted sintering cycle, whose impact would become clear with the last investigated samples.

Post-densification of the green bodies, either CIP or HIP, did not lead to a successful elimination of the cavities, meaning that the cavities are connected throughout the sample which would be referred to as open porosity, rendering every isostatic pressure procedure useless. The magnetic saturation values corrected the previous statement that samples 3spDB and 4spDB were two-phased, as the fully sintered samples, which were thermally debinded with the same parameters showed, that applying H₂ between 450 and 550°C is enough to shift the C balance into the η region.

To summarize, FFF production of dense hardmetal bodies poses several challenges:

- First, no fully dense specimen was obtained, even though several parameters were changed. The strategy to print the border and the centre with different strategies (circular and then zigzag shaped) in many cases led to the formation of large interface cavities because of poor row bonding between these different areas. While the printing parameters were optimized over the course of the thesis, only parts of the samples benefited from the change, while the cavities could not be eliminated in other areas. Another approach to fully print one layer in a circular way should be investigated in the future as for tooling applications the centre of a tool is often not as exposed to stress as the outer parts and single cavities could be negligible, even though a hardmetal part should generally not contain any pores whatsoever. Furthermore, the printing strategy must be tailored perfectly to a single geometry, as the production of a dense hardmetal drill bit requires other printing strategies than the printing of a block, as was shown during this thesis. FFF with filled filaments with a general set of parameters applicable to any geometry is highly doubtful as this does not even work with standard FFF

material such as PLA or ABS. A post-densification of the green bodies was unsuccessful due to open porosity.

- The selection of the printer should be carefully made for future investigations. Our research group acquired the Wanhao Duplicator i3 Plus based on the model MU Leoben was using, to avoid or minimize an influence by the hardware performance. However, these Wanhao models are part of the lower end of the low-cost printer segment and require a lot of optimization, expertise, and time to produce favourable results. Contrary to MU Leoben's team the author did not have any experience in operating an FFF printer before, let alone the experience in optimizing one towards filled filaments. The time consumed by tinkering and working on the printer itself was tremendous and the planned schedule and the number of experiments on self-printed samples suffered under these circumstances. For future projects the author recommends choosing the printer wisely, e.g. one with a higher investment cost which may also produce significantly better results regarding the cavities and the improper row bonding. The possibility of using an industrial printed should be considered, although such a device is very costly and hard to get one's hand onto.
- The thermal debinding process depends on the density of the sample. While the solvent debinding step poses no difficulties, the thermal debinding step regarding hardmetals is very sensitive. As shown in this thesis the debinding conditions can stay the same but will produce different results for different levels of cavitation. While pure N₂ at a maximum temperature might be enough to push the C balance of a sample with a lot of cavities into the two-phase area, a higher temperature which should normally lead to a larger C loss, could produce a sample containing free C, if the green body was initially denser.
- The printing behaviour and surface quality is dependent on the RTP wax which was shown by using two different RTP powders with the same organic binder. As the inorganic components do not affect the printing behaviour and only differ in grainsize and not composition, the only possible factor is the paraffin-based RTP wax. Unfortunately, information on the wax's nature was not provided by the manufacturer. However, every manufacturer uses a different RTP wax and in most cases, it is recycled which means that the wax from one manufacturer might not be the same in different powder batches. This is a significant hindrance in the process of using commercially available RTP powder for the production of filament for FFF printing, as the wax obviously influences the printing itself.

This thesis' aim was to further improve the insight on the process parameters during the FFF production of hardmetal parts. The crucial issue is still the production of cavity-free specimen, onto which a thermal debinding program can be tailored to as the porous parts will always react differently to a certain program. The printing process should be investigated on a printer of higher quality to see if the formation of cavities might be a hardware-related issue. Nevertheless there is no doubt that the relevance of FFF in hardmetal production could rise, if dense specimen can be produced, and by looking at the fast developing AM technologies in general one can tell that it is only a matter of time until the cavity issue due to the shaping process is attended to.

A list of the most promising candidates and their printing parameters is presented in Tab. 12.

Tab. 12 Most promising candidates regarding the cavity situation

Sample	Tnozzle(°C)	Tbed(°C)	Print speed (mm/s)	Flow rate (%)
1AH ₂ 800AIC	250	95	12	130
1AH ₂ 800AIB	250	95	12	130
1AN ₂ 800CC	250	95	12	130
1AH ₂ 600AIC	250	95	12	130
1AN ₂ 600AIC	250	95	12	130
1AN ₂ 600AIB	250	95	12	130
2AN ₂ 600CC	250	95	16	111
2AN ₂ 600CDB	250	95	16	111
5eAH ₂ 200to300AIB	250	95	10	115
5eAH ₂ 200to300AIDB	250	95	10	115
5fAN ₂ 800AIC	250	95	10	115
5fAN ₂ 800AIB	250	95	10	115
5fAN ₂ 800AIDB	250	95	10	115
5iAN ₂ 800AIDB	250	95	23	117
1spBN ₂ 800AIC	240	70	10	100
4spAH ₂ 450to550AIDB	250	95	10	110

Bibliography

1. Lengauer, W., Duretek, I., Schwarz, V., Kukla, C., Kitzmantel, M., Neubauer, E., Lieberwirth, C., and Morrison, V.; **Preparation and properties of extrusion-based 3D-printed hardmetal and cermet parts**; *Euro PM2018 Congress & Exhibition - Bilbao, Spain*; (2018)
2. Crump, S.; **Apparatus and method for creating three-dimensional objects**; *US5121329A*; (1992)
3. Sher, D.; **Additive manufacturing with metal powders market to top \$11B by 2024**; last updated 2019/06/04, accessed 2020/04/08; Available from: <https://www.3dprintingmedia.network/additive-manufacturing-with-metal-powders/>.
4. Sher, D.; **SmartTech's quick-access Ceramics AM Dataset and Report highlights long tail market opportunity**; last updated 2019/09/09, accessed 2020/04/08; Available from: <https://www.3dprintingmedia.network/smartech-releases-ceramics-am-dataset/>.
5. Agarwala, M., Weeren, R., Vaidyanathan, R., Bandyopadhyay, A., Carrasquillo, G., Jamalabad, V., Langrana, N., Safari, A., Garofalini, S., and Danforth, S.; **Structural ceramics by fused deposition of ceramics**; *6th International Solid Freeform Fabrication Symposium - Austin, Texas, USA*; (1995)
6. Geiger, M., Steger, W., Greul, M., and Sindel, M.; **Multiphase Jet Solidification-a new process towards metal prototypes and a new data interface**; *5th International Solid Freeform Fabrication Symposium - Austin, Texas, USA*; (1994)
7. Griffin, E. and McMillin, S.; **Selective laser sintering and fused deposition modeling processes for functional ceramic parts**; *6th International Solid Freeform Fabrication Symposium - Austin, Texas, USA*; (1995)
8. Kitzmantel, M., Lengauer, W., Duretek, I., Schwarz, V., Kukla, C., Lieberwirth, C., Morrison, V., Wilfinger, T., and Neubauer, E.; **Potential of Extrusion Based 3D-printed Hardmetal and Cermet Parts**; *World PM2018 Congress & Exhibition - Beijing, China*; (2018)
9. Lengauer, W., Duretek, I., Fürst, M., Schwarz, V., Gonzalez-Gutierrez, J., Schuschnigg, S., Kukla, C., Kitzmantel, M., Neubauer, E., Lieberwirth, C., and Morrison, V.; **Fabrication and properties of extrusion-based 3D-printed hardmetal and cermet components**; *International Journal of Refractory Metals & Hard Materials*, 82: p. 141-149; (2019)
10. Kupp, D., Eifert, H., Greul, M., and Kunstner, M.; **Rapid Prototyping of Functional Metal and Ceramic Components by the Multiphase Jet Solidification (MJS) Process**; *8th International Solid Freeform Fabrication Symposium - Austin, Texas, USA*; (1997)

11. ISO/ASTM, **Additive manufacturing - General principles - Terminology (ISO/ASTM DIS 52900:2018)**; (2018)
12. Sachs, E., Cima, M., Williams, P., Brancazio, D., and Cornie, J.; **Three Dimensional Printing: Rapid Tooling and Prototypes Directly from a CAD Model**; *Journal of Engineering for Industry*, 114 (4): p. 481-488; (1992)
13. Sachs, E., Haggerty, J., Cima, M., and Williams, P.; **Three-dimensional printing techniques**; *US5204055*; (1993)
14. Griffith, M., Keicher, D., and Atwood, C.; **Free form fabrication of metallic components using laser engineered net shaping (LENS)**; *7th International Solid Freeform Fabrication Symposium - Austin, Texas, USA*; (1996)
15. Pearson, A.; **The history of 3D printing.**; accessed 2020/04/16; Available from: <https://www.stratasys.com/explore/article/3d-printing-history>.
16. Jones, R., Haufe, P., Sells, E., Iravani, P., Olliver, V., Palmer, C., and Bowyer, A.; **RepRap – the replicating rapid prototyper**; *Robotica*, 29 (1): p. 177-191; (2011)
17. Sanders Jr., R., Forsyth, J., and Philbrook, K.; **3-D model maker**; *US5506607A*; (1996)
18. Molitch-Hou, M.; **Overview of additive manufacturing process**, in *Additive Manufacturing Materials, Processes, Quantifications and Applications*, J. Zhang and Y.-G. Jung, Butterworth-Heinemann: p. 1-38; (2018)
19. Gothait, H.; **Apparatus and method for three dimensional model printing**; *US6259962B1*; (2001)
20. Deckard, C.; **Method and apparatus for producing parts by selective sintering**; *US4863538A*; (1989)
21. Feygin, M.; **Apparatus and method for forming an integral object from laminations**; *US4752352A*; (1988)
22. Wolf, M.; **3D Printing With Paper At Your Local Office Supply Store? Yep, If Mcor Has Its Way**; last updated 2013/03/13, accessed 2020/04/20; Available from: <https://www.forbes.com/sites/michaelwolf/2013/03/13/3d-printing-with-paper-at-your-local-office-supply-store-yep-if-mcor-has-its-way/>.
23. Kodama, H.; **Automatic method for fabricating a three-dimensional plastic model with photo-hardening polymer**; *Review of scientific instruments*, 52 (11): p. 1770-1773; (1981)
24. André, J., Le Mehaute, A., and De Witte, O.; **Dispositif pour réaliser un modèle de pièce industrielle**; *FR2567668B1*; (1986)
25. Hull, C.; **Apparatus for production of three-dimensional objects by stereolithography**; *US4575330A*; (1986)

26. Mansfield, B., Torres, S., Yu, T., and Wu, D.; **A Review on Additive Manufacturing of Ceramics**; *ASME 2019 14th International Manufacturing Science and Engineering Conference - Erie, Pennsylvania, USA*; (2019)
27. Deckers, J., Vleugels, J., and Kruth, J.; **Additive Manufacturing of Ceramics: A Review**; *Journal of Ceramic Science and Technology*, 5 (4): p. 245-260; (2014)
28. Bertrand, P., Bayle, F., Combe, C., Goeuriot, P., and Smurov, I.; **Ceramic components manufacturing by selective laser sintering**; *Applied Surface Science*, 254 (4): p. 989-992; (2007)
29. Owen, D., Hickey, J., Cusson, A., Ayeni, O., Rhoades, J., Deng, Y., Zhang, Y., Wu, L., Park, H.-Y., Hawaldar, N., Raikar, P., Jung, Y.-G., and Zhang, J.; **3D printing of ceramic components using a customized 3D ceramic printer**; *Progress in Additive Manufacturing*, 3 (1-2): p. 3-9; (2018)
30. Schwentenwein, M. and Homa, J.; **Additive Manufacturing of Dense Alumina Ceramics**; *International Journal of Applied Ceramic Technology*, 12 (1): p. 1-7; (2015)
31. Griffith, M. and Halloran, J.; **Freeform fabrication of ceramics via stereolithography**; *Journal of the American Ceramic Society*, 79 (10): p. 2601-2608; (1996)
32. Chartier, T., Dupas, C., Lasgorceix, M., Brie, J., Delhote, N., and Chaput, C.; **Additive manufacturing to produce complex 3D ceramic parts**; *Journal of Ceramic Science and Technology*, 6 (2): p. 95-104; (2015)
33. Du, W., Ren, X., Ma, C., and Pei, Z.; **Binder jetting additive manufacturing of ceramics: A literature review**; *ASME 2017 International Mechanical Engineering Congress and Exposition - Tampa, Florida, USA*; (2017)
34. Frazier, W.E.; **Metal Additive Manufacturing: A Review**; *Journal of Materials Engineering and Performance*, 23 (6): p. 1917-1928; (2014)
35. Herzog, D., Seyda, V., Wycisk, E., and Emmelmann, C.; **Additive manufacturing of metals**; *Acta Materialia*, 117: p. 371-392; (2016)
36. DebRoy, T., Wei, H., Zuback, J., Mukherjee, T., Elmer, J., Milewski, J., Beese, A., Wilson-Heid, A., De, A., and Zhang, W.; **Additive manufacturing of metallic components – Process, structure and properties**; *Progress in Materials Science*, 92: p. 112-224; (2018)
37. Gothait, H., Kritchman, E., Benichou, A., Shmal, T., Eytan, G., Salalha, W., Dayagi, Y., Kodinets, O., and Lavid, L.; **Methods and systems for printing 3d object by inkjet**; *IL245142D0*; (2016)

38. Zhang, Y., Wu, L., Guo, X., Kane, S., Deng, Y., Jung, Y.-G., Lee, J.-H., and Zhang, J.; **Additive Manufacturing of Metallic Materials: A Review**; *Journal of Materials Engineering and Performance*, 27 (1): p. 1-13; (2018)
39. Rane, K. and Strano, M.; **A comprehensive review of extrusion-based additive manufacturing processes for rapid production of metallic and ceramic parts**; *Advances in Manufacturing*, 7 (2): p. 155-173; (2019)
40. Jabbari, A. and Abrinia, K.; **Developing thixo-extrusion process for additive manufacturing of metals in semi-solid state**; *Journal of Manufacturing Processes*, 35: p. 664-671; (2018)
41. Cesarano, J.; **A Review of Robocasting Technology**; *MRS Proceedings*, 542: p. 133; (1998)
42. Agarwala, M., Weeren, R.v., Bandyopadhyay, A., Whalen, P., Safari, A., and Danforth, S.; **Fused deposition of ceramics and metals: an overview**; *7th International Solid Freeform Fabrication Symposium - Austin, Texas, USA*; (1996)
43. Wu, G., Langrana, N., Rangarajan, S., Sadangi, R., Safari, A., and Danforth, S.C.; **Feasibility of Fabricating Metal Parts from 17- 4PH Stainless Steel Powder**; *9th International Solid Freeform Fabrication Symposium - Austin, Texas, USA*; (1998)
44. Wu, G., Langrana, N.A., Rangarajan, S., McCuiston, R., Sadanji, R., Danforth, S., and Safari, A.; **Fabrication of metal components using FDMet: fused deposition of metals**; *10th International Solid Freeform Fabrication Symposium - Austin, Texas, USA*; (1999)
45. Li, J., Xie, Z., Zhang, X., Zeng, Q., and Liu, H.; **Study of Metal Powder Extrusion and Accumulating Rapid Prototyping**; *Key Engineering Materials*, 443: p. 81-86; (2010)
46. Yang, Y., Zhang, C., Wang, D., Nie, L., Wellmann, D., and Tian, Y.; **Additive manufacturing of WC-Co hardmetals: a review**; *The International Journal Of Advanced Manufacturing Technology*, 108 (5-6): p. 1653-1673; (2020)
47. Aramian, A., Razavi, S., Sadeghian, Z., and Berto, F.; **A review of additive manufacturing of cermets**; *Additive Manufacturing*, 33; (2020)
48. Chen, J., Huang, M., Fang, Z., Koopman, M., Liu, W., Deng, X., Zhao, Z., Chen, S., Wu, S., Liu, J., Qi, W., and Wang, Z.; **Microstructure analysis of high density WC-Co composite prepared by one step selective laser melting**; *International Journal of Refractory Metals and Hard Materials*, 84; (2019)
49. Kumar, S.; **Manufacturing of WC-Co moulds using SLS machine**; *Journal of Materials Processing Technology*, 209 (8): p. 3840-3848; (2009)

50. Kumar, S. and Czekanski, A.; **Optimization of parameters for SLS of WC-Co**; *Rapid Prototyping Journal*, 23 (6): p. 1202-1211; (2017)
51. Kernan, B., Sachs, E., Oliveira, M., and Cima, M.; **Three-dimensional printing of tungsten carbide–10wt% cobalt using a cobalt oxide precursor**; *International Journal of Refractory Metals and Hard Materials*, 25 (1): p. 82-94; (2007)
52. Enneti, R., Prough, K., Wolfe, T., Klein, A., Studley, N., and Trasorras, J.; **Sintering of WC-12%Co processed by binder jet 3D printing (BJ3DP) technology**; *International Journal of Refractory Metals and Hard Materials*, 71: p. 28-35; (2018)
53. Zhang, X., Guo, Z., Chen, C., and Yang, W.; **Additive manufacturing of WC-20Co components by 3D gel-printing**; *International Journal of Refractory Metals and Hard Materials*, 70: p. 215-223; (2018)
54. Enneti, R. and Prough, K.; **Wear properties of sintered WC-12% Co processed via Binder Jet 3D Printing (BJ3DP)**; *International Journal of Refractory Metals and Hard Materials*, 78: p. 228-232; (2019)
55. Lieberwirth, C. and Seitz, H.; **Additive manufacturing with metal injection molding granules**; *13th Rapid. Tech.-International Trade Show & Conference for Additive Manufacturing - Erfurt, Germany*; (2016)
56. Lieberwirth, C., Harder, A., and Seitz, H.; **Extrusion based additive manufacturing of metal parts**; *Journal of Mechanics Engineering and Automation*, 7: p. 79-83; (2017)
57. Schröter, K.; **Gesinterte harte Metallegierungen und Verfahren zu ihrer Herstellung**; 420689; (1923)
58. maschine+werkzeug; **Optimierte Cermets**; last updated 2015/06, accessed 2020/08/06; Available from: <https://www.maschinewerkzeug.de/werkzeuge/uebersicht/artikel/optimierte-cermets-1109703.html>.
59. Holleck, H.; **Binäre und ternäre Carbid- und Nitridsysteme der Übergangsmetalle**; *Materialkundlich-technische Reihe: Borntraeger*; (1984)
60. Raghavan, V.; **C-Co-Fe-Ni-W (Carbon-Cobalt-Iron-Nickel-Tungsten)**; *Journal of Phase Equilibria and Diffusion*, 28 (3): p. 284-285; (2007)
61. 3Dreams; **Wanhao Duplicator i3 Plus**; accessed 2020/07/31; Available from: <https://3-dreams.de/wp-content/uploads/2018/06/Wanhao-Duplicator-i3-Plus-%D1%83%D0%BA%D1%80%D0%B0%D0%B8%D0%BD%D0%B0-600x600.jpg>.

62. Topić, I., Sockel, H.G., Wellmann, P.J., and Göken, M.; **The influence of microstructure on the magnetic properties of WC/Co hardmetals**; *Materials Science and Engineering: A*, 423 (1-2): p. 306-312; (2006)